Kelvin-Helmholtz instability at the magnetopause : theory and observations

Claudia Rossi

PHD THESIS IN CO-SUPERVISION BETWEEN:

UNIVERSITÀ DEGLI STUDI DI PISA

SCUOLA DI DOTTORATO DI RICERCA IN FISICA APPLICATA

UNIVERSITÉ PIERRE ET MARIE CURIE

ÉCOLE DOCTORALE "ASTRONOMIE ET ASTROPHYSIQUE D' ÎLE DE FRANCE"

CLAUDIA ROSSI

KELVIN-HELMHOLTZ INSTABILITY AT THE MAGNETOPAUSE: THEORY AND OBSERVATIONS

SSD: FIS/06 Fisica per il sistema Terra ed il mezzo circumnterrestre

Discussed 29/04/2015, Jury:

- Francesco, PEGORARO, Università di Pisa, Italy, (President of the jury)
- Francesco, CALIFANO, Università di Pisa, Italy, (Supervisor)
- Alessandro, RETINÒ, LPP, Ecole Polytechnique, France (Co-Supervisor)
- Claire, FOULLON, University of Exeter, UK (Referee)
- Gaetano, ZIMBARDO, Università della Calabria, Italy (Referee)
- Martin, VOLWERK, Austrian Academy of Sciences, Austria (Examiner)
- Matteo, FAGANELLO, Aix Marseille Université, France (Examiner)
- Arnaud, ZASVLASKY, LESIA, Observatoire de Paris, France (Examiner)

ABSTRACT

The interaction between the solar wind and the Earth's magnetosphere is mediated by the magnetopause. The dynamics occurring at this boundary depends on various aspects as, e.g., the solar wind dynamic pressure or the direction of the Interplanetary Magnetic Field (IMF). The solar wind, streaming from the Sun carries with it the IMF which interacts with northwards geomagnetic field lines causing magnetic reconnection events, particularly effective when the IMF is directed southwards. Magnetic reconnection makes a large amount of solar wind particles to be tranferred into the Earth's magnetosphere. If the IMF is directed northward magnetic reconnection can take place at high latitude, but it is not efficient enough to justify the amount of cold and dense solar wind plasma observed by satellites inside the magnetosphere. Furthermore, in northwards conditions one observe the formation of a wide boundary layer at the low latitude. This boundary layer is thought to be the result of the observed plasma transfer driven by the development of the Kelvin-Helmholtz (K-H) instability. This instability, originating from the velocity shear between the solar wind and the almost static near-Earth plasma, develops along the flanks of the magnetopause giving rise to vortex like structures that in turn create the favorable conditions for solar wind plasma transfer. In particular, the vortices can merge forming eventually large structures, carrying with them solar wind plasma and magnetic field lines. The large scale dynamics of K-H vortices generates favorable conditions for the development of secondary instabilities important for the plasma transport as, for example Rayleigh-Taylor and secondary K-H instability, as well as magnetic reconnection occurring inside the vortices themselves or in-between.

Numerical simulations have also shown that the long time evolution of this instability is characterized by the formation of a layer dominated either by vortex like, coherent structures or by small scale structures in a more or less turbulent state, depending on the competition between vortex pairing and secondary instabilities that take place in the non linear phase. In particular, last ten years of simulations have shown that the competition between the merging mechanism and the development of secondary instabilities depends strongly on the initial velocity, density and magnetic large scale field profiles used as initial conditions in the simulations.

Therefore, in order to make a further step towards the comprehension of this complex system, it is imperative to combine satellite data and numerical simulations. The idea here is to initialize numerical simulations by using direct in-situ observations of the main field pro-

files since only a correct initialization can reproduce the correct dynamics. Note that in-situ measurements are limited at short crossings of the magnetopause for orbital reasons, so that we would not be able to follow the temporal evolution of the Kelvin-Helmholtz instability.

The main goals of this thesis are: (i) to investigate the properties of the development of the K-H and its further non-linear dynamics eventually leading to turbulence; (ii) to investigate the small scale mechanisms occurring inside the mixing layer in the long time evolution of the instability; (iii) to find observational events when satellites cross the magnetopause under K-H condition but before the instability develops and (iv) to recover the profiles of the principal physical quantities and to use them to initialize our numerical simulations.

In this study a "two-fluid" plasma model is adopted using 2D simulations to understand the role of K-H instability at low latitude magnetopause. The code has been developed at the University of Pise and has already been used for different scientific publications, Ref. Faganello et al. [30, 31, 33], Tenerani et al. [116], Palermo et al. [87], Henri et al. [56]. From the experimental point of view, we use data from the ACE satellite orbiting in the solar wind to monitor the IMF conditions and the measurement from Cluster and Geotail satellites to study the magnetopause. In particular we use particles and electromagnetic fields to reconstruct the profiles across the magnetopause (density, magnetic and velocity fields profiles, etc..) to be used as more realistic initial conditions for the numerical simulations.

The main results achieved during this work are: (i) characterize the turbulence inside K-H vortices and the small scale magnetic reconnection events responsible for the observed intermittency; (ii) select one event in particular where we have the combination of a satellite measurement before and after K-H develops and find that the density and velocity profile centers are shifted by a distance comparable to their shear lengths and (iii) that this initial shift cause a different evolution of the K-H instability leading to a final state in agreement with satellites observations.

This thesis shows that the combination of spacecraft data and numerical simulations is the most effective way to study complex phenomena of plasma transport across frontiers, such as Kelvin-Helmholtz instability at the magnetopause.

RÉSUMÉ

L'interaction entre les plasmas du vent solaire et de la magnétosphère terrestre se fait par l'intermédiaire de la magnétopause, frontière qui sépare la magnétosphère de la magnétogaine (région derrière le choc où le plasma du vent solaire est ralenti). La dynamique de la magnétopause dépend en particulier de la pression dynamique du vent solaire et de la direction du champ magnétique interplanétaire. Le vent solaire est éjecté du Soleil et voyage à travers le système solaire en transportant avec lui le champ magnétique interplanétaire. Ce dernier interagit avec les lignes du champ géomagnétique (dirigé vers le nord) provoquant le phénomène de reconnexion des lignes de champ magnétique, particulièrement efficace lorsque le champ magnétique interplanétaire est dirigé vers le sud. La reconnexion magnétique permet l'entrée d'une grande quantité de particules du vent solaire dans la magnétosphère de la Terre. Si le champ magnétique interplanétaire est dirigé vers le nord, la reconnexion magnétique peut avoir lieu à haute latitude, mais n'est pas assez efficace pour justifier la quantité de plasma froid et dense, typique du vent solaire, observée par les satellites à l'intérieur de la magnétosphère. En outre, dans les cas où le champ magnétique interplanétaire est dirigé vers le nord, la formation d'une couche de mélange est observée à basse latitude. Les tourbillons de Kelvin-Hemholtz fournissent un mécanisme efficace pour la formation d'une couche de mélange à la magnétopause à basse latitude. Cette instabilité se produit à la magnétopause où il existe un déchirement de vitesse entre le vent solaire et le plasma de la magnétosphère, donnant lieu à la formation de tourbillons qui, à leur tour créent les conditions favorables pour le transport du plasma du vent solaire dans la magnétosphère. En particulier, l'interaction entre différentes échelles dans les tourbillons de Kelvin-Hemholtz peuvent former des grandes structures qui transportent le plasma du vent solaire et les lignes du champ magnétique. La dynamique à grande échelle des tourbillons de Kelvin-Hemholtz crée des conditions favorables pour le développement de la reconnexion magnétique, un autre mécanisme efficace pour expliquer le transport du plasma du vent solaire. D'autre part, différents types d'instabilités secondaires peuvent se produire dans les tourbillons de Kelvin-Hemholtz, qui sont aussi importantes pour le transport (par exemple l'instabilité de Rayleigh-Taylor). Les simulations numériques montrent que l'évolution temporelle de cette instabilité est caractérisée par des phénomènes à petite échelle qui se produisent localement à l'intérieur des tourbillons, tels que la reconnexion magnétique à petite échelle, des instabilités secondaires et la turbulence

associée à ces instabilités. Au cours des dernières années, les simulations de Kelvin-Helmholtz, ont également montré que la concurrence entre les mécanismes de fusion des tourbillons et le développement des instabilités secondaires dépend fortement des profils initiales de déchirement de vitesse, de densité et de champ magnétique à grande échelle. La comparaison des données spatiales et des simulations numériques est donc d'une importance fondamentale dans ce contexte. Cependant, les données satellites sont limitées à des traversées relativement courtes de la magnétopause (en raison de l'orbite), qui ne peuvent donc pas suivre complètement l'évolution temporelle des différents phénomènes. Par contre, les simulations numériques peuvent suivre cette évolution, à condition de disposer des conditions initiales réalistes. Dans ce contexte, les principaux objectifs de cette thèse sont les suivantes : (i) analyser les propriétés du développement de l'instabilité de Kelvin-Hemholtz ainsi que de sa dynamique nonlinéaire conduisant au développement de turbulence; (ii) analyser les mécanismes à petites échelles qui se produisent dans l'évolution temporelle de l'instabilité dans la cuoche de mélange ; (iii) trouver des observations "in situ" de traversées de magnétopause dans des cas où l'écoulement est instable (du point de vue de l'instabilité de Kelvin-Hemholtz), mais avant que l'instabilité ne se développe de faccon à (iv) récupérer les profils des principales grandeurs physiques et les utiliser pour initialiser nos simulations numériques.

Dans le cadre de cette étude l'instabilité de Kelvin-Hemholtz à la magnétopause est modélisée par des simulations numériques de type bi-fluide à deux dimensions (2D). Le code de simulation a été développé à l'Université de Pise et avait dé jà utilisé pour plusieurs publications scientifiques, Ref. Faganello et al. [30, 31, 33], Tenerani et al. [116], Palermo et al. [87], Henri et al. [56]. Du point de vue expérimental, le travail est basé sur l'exploitation de données fournies par le satellite ACE, en orbite dans le vent solaire, pour surveiller les conditions du champ magnétique interplanétaire et des données des satellites Cluster et Geotail pour étudier la magnétopause. En particulier, nous avons utilisé des données des particules et des champs électromagnétiques, pour reconstruire des profils à travers de la magnétopause (densité, champ magnétique, etc.) à utiliser comme conditions initiales réalistes dans les simulations numériques. Les principaux résultats obtenus au cours de ce travail sont les suivants : (i) caractérisation de la turbulence à l'intérieur des tourbillons de Kelvin-Hemholtz, ainsi que des événements de reconnexion magnétique à petite échelle responsables de l'intermittence observé ; (ii) sélection d'un événement en particulier où nous avons une combinaison des données des satellites avant et après que l'instabilité se développe (iii) observation d'un décalage entre les profils de densité et de vitesse (d'une distance comparable à celle de leurs longueurs de gardient) et constat que ce décalage initial entraîne une évolution différente de

la simulation qui est en accord avec les observations satellite. Cette thèse montre que la combinaison entre analyses de données spatiales et simulations numériques est la façon plus efficace pour étudier des phénomènes complexes tels que le transport du plasma a travers les frontières.

RIASSUNTO

L'interazione tra il vento solare e la magnetosfera terrestre é mediato dalla magnetopausa. La dinamica in questa regione dipende da vari aspetti, come la pressione dinamica del vento solare o la direzione del campo magnetico interplanetario. Il vento solare é un flusso di particelle cariche proveniente dal Sole che trasporta con sè le linee di campo magnetico interplanetario che interagendo con il campo magnetico terrestre, diretto verso nord, causano il fenomeno della riconnessione magnetica, che é particolarmente importante quando il campo interplanetario è diretto verso sud. La riconnessione magnetica fà si che una grande quantità di particelle del vento solare sia trasferita nella magnetosfera terrestre. Se il campo interplanetario é diretto verso nord, la riconnessione magnetica avviene ad alta latitudine, questo meccanismo però non è sufficiente a spiegare la quantita di plasma di vento solare, freddo e denso, osservato dai satelliti nella magnetosfera. Inoltre, quando il campo interplanetario è diretto verso nord, si osserva la formazione di uno strato limite a bassa latitudine, in cui si ha la presenza, allo stesso tempo, di plasma di vento solare e magnetosferico. Questo strato si pensa sia responsabile del trasferimento di plasma di vento solare, e si pensa sia generato dall'evoluzione dell'instabilità di Kelvin-Helmholtz. Questa instabilità, origina dal salto di velocità tra il vento solare e il plasma quasi statico che si trova vicino alla Terra. L'instabilità si sviluppa lungo i fianchi della magnetopausa, genera strutture vorticose che creano le condizioni favorevoli per il trasferimento di plasma di vento solare. In particolare, i vortici si possono unire formando eventualmente strutture a scala più grande, trascinando con loro il plasma di vento solare e le linee di campo magnetico. La dinamica a grande scala dei vortici di K-H genera le condizioni favorevoli per lo sviluppo di instabilità secondarie importanti per il trasporto di plasma, come per esempio l'instabilità di Rayleigh-Taylor, la K-H secondaria e la riconnessione magnetica, che può avvenire tra i vortici o all'interno di essi stessi.

Le simulazioni numeriche hanno mostrato anche che, l'evoluzione di questa instabilità é caratterizzata, su tempi lunghi, dalla formazione di un mixing layer in cui si trovano strutture di piccola scala in uno stato turbolento. Negli ultimi anni le simulazioni di K-H, hanno anche mostrato che la competizione tra il meccanismo di fusione dei vortici e quello in cui si formano le instabilità secondarie, dipende fortemente dai profili iniziali a grande scala di velocità, densità e campo magnetico usati come condizione iniziale nelle simulazioni. La combinazione dei dati di satellite e delle simulazioni numeriche è quindi di fondamentale importanza in questo contesto. Infatti i dati

di satellite, per questioni orbitali, sono limitati ad attraversamenti brevi della magnetopausa, perciò non siamo in grado di seguire, solo attraverso le osservazioni, l'evoluzione temporale dell'instabilità di Kelvin-Helmholtz. D'altra parte, le simulazioni numeriche possono seguire la sua evoluzione temporale ma, come abbiamo appena discusso, hanno bisogno degli attraversamenti dei satelliti per ottenere quali siano le condizioni iniziali più realistiche possibili.

I principali obiettivi di questa tesi sono: (i) studiare le proprietà dello sviluppo della K-H e la sua conseguente dinamica non lineare che porta eventualmente allo sviluppo della turbolenza; (ii) studiare i meccanismi che avvengono a piccola scala all'interno del mixing layer nell'evoluzione dell'instabilità su tempi lunghi; (iii) trovare eventi osservativi in cui i satelliti attraversano la magnetopausa sotto condizioni favorevoli per la K-H ma prima che l'instabilità si sviluppi e (iv) ottenere i profili delle principali quantità fisiche ed usarli per inizializzare le nostre simulazioni numeriche.

In questo lavoro usiamo un modello a "due fluidi" per descrivere il plasma e le simulazioni 2D per comprendere il ruolo dell'instabilità di K-H nella magnetopausa a bassa latitudine. Il codice è stato sviluppato a Pisa ed è stato impiegato per diverse pubblicazioni scientifiche, Ref.Faganello et al. [30, 31, 33], Tenerani et al. [116], Palermo et al. [87], Henri et al. [56]. Da un punto di vista sperimentale, usiamo i dati del satellite ACE che orbita nel vento solare per controllare le condizioni del campo magnetico interplanetario e i dati dei satelliti Cluster e Geotail per studiare la magnetopausa. In particolare, usiamo i dati di particelle e campi elettromagnetici per ricostruire i profili attraverso la magnetopausa (di densità, campo magnetico, velocità, etc..) per usarli come condizioni iniziali all'interno delle simulazioni, in modo che questi siano il più vicino possibile alla realtà.

I risultati principali ottenuti durante questo lavoro sono: (i) caratterizzare la turbolenza all'interno dei vortici di K-H e la riconnessione magnetica che avviene tra le strutture a piccola scala e responsabile dell'intermittenza osservata; (ii) l'aver selezionato un evento in particolare dove abbiamo la combinazione di misure di satellite prima e dopo lo sviluppo della K-H ed abbiamo trovato che i profili di densità e velocità sono separati da una distanza comparabile alle loro lunghezze di shear e (iii) che questa separazione iniziale causa una diversa evoluzione nelle simulazioni K-H che é più vicina alle osservazioni dei satelliti.

Questa tesi mostra che la combinazione di dati di satellite e delle simulazioni è il modo più effettivo di studiare la complessa dinamica del trasporto di plasma attraverso le frontiere, come l'instabilità di K-H alla magnetopausa.

ACKNOWLEDGMENTS

I am greatful for all the people I met during the research work of these years that in many ways have supported and helped me to improve. In particular:

- I am deeply grateful to my supervisors Francesco Califano, Alessandro Retinò and Laurence Rezeau for having given me the chance to learn and work with them. They guided and helped me during this work, teaching me a lot both from a human and scientific point of view;

- I would like to express my gratitude to all the people I had the honour to collaborate with during the preparation of this thesis. Among them a special thanks goes to Pierre Henri that has been a guide and a friend during these years and to Prof. F. Pegoraro for the useful discussions and for having been always enlighting in answering all my questions;

- This work has been conducted in partnership between the University of Pisa and the Ecole Polytechnique, I am sincerely grateful to the Plasma groups of both universities for the interesting exchanges of opinions, in particular I would like to thank very much all the friends I met, I wish I could find the words to express all my gratitude for sharing the tough and funny moments;

- I would like to thank all the the members of the jury for their partecipation and for evaluating this work, in particular the referees for their interest in carefully reading my manuscript and for all their useful comments;

- The research leading to these results has received, funding from the European Commission's Seventh, Framework Programme (FP7/2007-2013) under the Grant, Agreement SWIFF (Project No. 263340, www.swiff.eu). We acknowledge the access to supermuc machine at LRZ made, available within the PRACE initiative receiving funding, from the European Commission's Seventh Framework, Programme (FP7/2007-2013) under Grant Agreement No., RI-283493, Project No. 2012071282. The authors also gratefully acknowledge the Gauss Centre for Supercomputing e.V. (www.gauss-centre.eu) for funding this project by providing computing time on the GCS Supercomputer SuperMUC at Leibniz Supercomputing Centre (LRZ, www.lrz.de) and the

italian CINECA supercomputing center (www.cineca.it) where the numerical code has been developed;

- The authors acknowledge the instrument teams and the ESA Cluster Science Archive (CAA) data center for providing Cluster data;
- Special thanks to the developers of the IRFU-Matlab used to work with space data, particularly with Cluster data from CAA;
- Part of the data analysis was done with the AMDA science analysis system provided by the Centre de Données de la Physique des Plasmas (IRAP, Université Paul Sabatier, Toulouse) supported by CNRS and CNES;
- Part of this Ph.D. in joint supervision between the University of Pise and the UPMC, was financed by a Programme Vinci 2013 Grant from the Università Franco-Italiana/Université Franco-Italienne (Projet C2-35, VINCI 2013 chapter 2);
- The authors thank Prof. H. Hasegawa for providing Geotail data and helpful discussions;
- Last but not least, thanks to my family for being supportive in every single choice I made.

So long, and thanks for all

CONTENTS

Part I

INTRODUCTION

1

INTERACTION BETWEEN SOLAR WIND AND EARTH'S MAGNETOSPHERE

1.1 INTRODUCTION

A very important problem in space plasma physics is how solar wind interacts with the Earth's magnetosphere after interactions through the Earth's bow shock. Many processes are at play for the mixing of the two plasmas nearby the interface, eventually leading to solar wind plasma entering into the Earth's magnetosphere. Solar wind is a flux of ionized particles flowing from the Sun, carrying throughout the solar system the Sun's magnetic field, also known as the Interplanetary Magnetic Field (IMF). Because of the rotation of the Sun, the magnetic field has a spiral shape, known as Parker Spiral, Ref. Parker [88]. According to the frozen-in theorem the plasma and the magnetic field lines are linked one to each other so that, in principle, no mixing between solar wind and magnetospheric plasma should exist. Observations show instead the presence of cold dense solar wind plasma inside the magnetosphere. The IMF component B_z perpendicular to the ecliptic has a fundamental role in solar wind plasma transfer into the magnetosphere. Indeed if $B_{z,IMF}$ is directed southward, it interacts with antiparallel geomagnetic field lines making possible reconnection processes at the dayside, see section 1.3 for details. This phenomena is at the origin of solar wind plasma enter into magnetopause, Ref. Dungey [26]. The solar wind particles are accelerated and pushed inside the magnetosphere as a consequence of the reconnection process, Ref. Cowley [21]. However satellites observations have revealed that even under northward IMF conditions cold and dense plasma is injected into the magnetosphere, in particular along the flanks of the magnetosphere, Ref. Terasawa et al. [117], Borovsky et al. [10], Wing and Newell [131]. Different possible mechanisms have been proposed to explain these observations, like high latitude magnetic reconnection, low latitude Kelvin-Helmoltz instability and anomalous diffusion across the magnetopause, Ref. Matsumoto and Seki [74]. During northward IMF, reconnection can still occur but at high latitude, this is called "double lobe reconnection". Moreover during northward IMF the presence of a broad boundary layer at low latitude has been observed at the flank side of the mag-

netosphere, Ref. Fujimoto et al. [44], Hasegawa et al. [51], Sckopke et al. [104], where a mixture of solar wind and magnetospheric populations coexist. Different mechanism have been proposed to explain this observational result, Ref. Terasawa et al. [117]. Among them an important transport mechanism is the Kelvin-Helmoltz instability (K-HI), responsible for anomalous diffusion at the magnetopause, Ref. Dungey [27], Miura [75]. Induced by a velocity shear, this instability can develop at the interface between the solar wind and the almost static magnetospheric plasma. Different satellite observations have revealed the presence of structures compatible with K-H vortices, see e.g. Ref. Hasegawa et al. [50]. Different kind of secondary instabilities that compete with vortex pairing in the non linear regime can further develop on the shoulder of the K-H vortices like the K-H itself, or the Rayleigh - Taylor (R-T) instability or magnetic reconnection, see section 1.3. All these secondary instabilities, that disrupt the vortices, are also a mechanism supporting the development of turbulence. Turbulence can be generated as well by the interaction between the vortices leading to vortex pairing process that eventually evolve in a turbulent non linear state. Turbulence at the interface between the solar wind and the magnetosphere is also a very important subject in space physics.

The purpose of this thesis is to study the evolution of the low latitude boundary layer system driven by the development of the K-H instability combining satellites' data and numerical simulations in order to study in the closest way to reality the dynamics at the magnetopause. The first step is to describe this region, characterized by strong gradients of density and magnetic field, by using data taken during satellites magnetopause crossings. Profiles of the main physical quantities, during satellite crossings, have been used as initial condition in the simulations. The objective is to compare simulation data and satellites measurements, for example by investigating the secondary instabilities inside K-H vortices, properties of magnetic reconnection sites and associated turbulence. A 2D two-fluid code is used, in order to describe the decoupling between the plasma and the magnetic field, a basic ingredient for describing plasma transport. Concerning satellite data, ACE, Geotail and Cluster satellites data have been used. This is motivated by the need to investigate different regions in the solar wind, with ACE, and at the magnetopause, with Geotail and Cluster.

1.2 SOLAR WIND AND MAGNETOSPHERIC PLASMA REGIONS

First indirect observations leading to consider the existence of a "*gas streaming outward from the Sun*", Parker [88], have been the presence of unexpected double tails in comets and phenomena like aurorae. The only possible explanation of such phenomena was to assume the

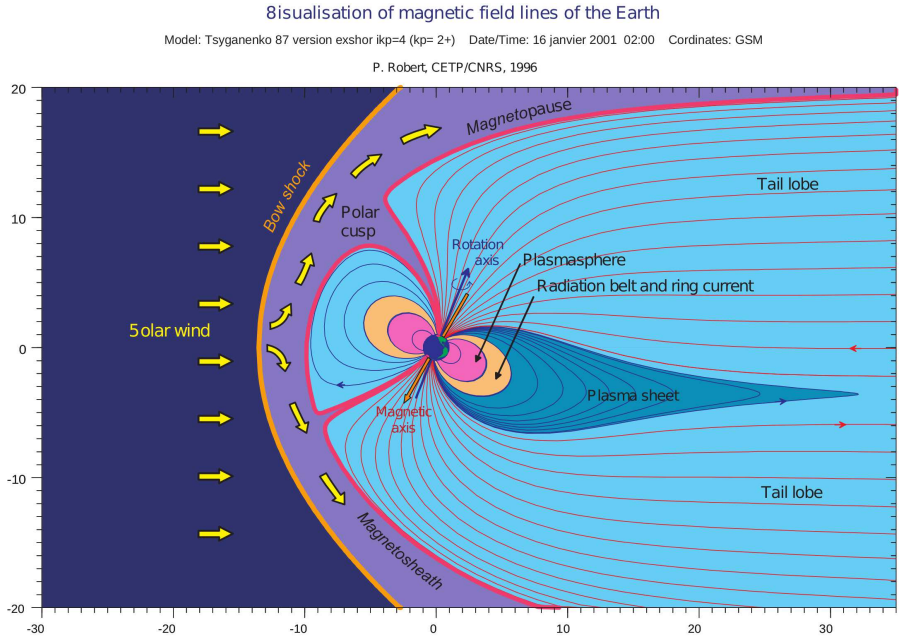

Figure 1: Scheme of the interaction between solar wind and Earth's magnetosphere. Courtesy of P. Robert.

presence of an ionized flux of particles, as later on observed thanks to space missions. Solar wind is a highly ionized plasma escaping from the Sun at velocities higher than the local sonic and Alfvènic velocities. It travels at two main speeds due to the different regions of the Sun from where it originates. Fast solar wind travels at about 700 km/s and it comes from polar coronal holes characterized by almost open magnetic field lines configuration. Slow solar wind, coming instead from equatorial regions of the Sun, has a velocity around 400 km/s being slowed down by the closed magnetic lines at the equator. The composition for the main species is the same: electrons, protons and a small percentage of alpha particles (~ 4 %), but the slow wind shows in general higher O^{7+}/O^{6+} ratio than the fast solar wind, Ref. Geiss et al. [45].

Solar wind flows in all directions and it interacts with the magnetosphere of the planets, a region of space where the magnetic field of the planet dominates on the plasma dynamics. When solar wind approaches the magnetosphere, its velocity slows down abruptly because of the planet magnetic field obstacle giving rise to a bow shock, as represented in orange in figure 1.

The shocked solar wind around the magnetopause, forms the magnetosheath, a region represented in violet in figure 1, a very turbulent medium, about $10 - 13$ R_E far from the Sun. In this region the magnitude and the direction of the magnetic field varies strongly. Magnetized planets are characterized by a magnetopause that separates the solar wind from the planet's magnetic field. Magnetopause

location is determined by pressure equilibrium between planetary magnetic pressure and solar wind dynamic pressure. The magnetopause boundary is not static but it moves towards or outwards Earth at velocities between $10-20$ km/s. Often satellites cross the magnetopause (MP) because of this rapid motion rather than of the velocity of the satellite itself. In absence of a magnetic field perpendicular to the layer it can be characterized as a tangential discontinuity. When crossing the magnetopause satellites enter in the magnetosphere. Magnetosheath and magnetosphere are characterized by different values of the plasma characteristic quantities detected by satellites. Indeed, in the magnetosheath satellites measure disturbed magnetic and velocity field, once approaching magnetosphere velocity field magnitude decreases (this is an almost static region) and magnetic field becomes more stable (geomagnetic field lines are less perturbed by the solar wind) and density decreases while temperature increases.

1.3 MAGNETIC RECONNECTION

Magnetic reconnection is one of the important processes occurring in a plasma. It takes place near the Earth's magnetopause, during solar flares, at the magnetotail and in fusion plasma (tokamaks), etc., and it produces a change of magnetic field topology together with a strong energy release. The process can be roughly resumed by saying that magnetic field lines, under some conditions, break and reconnect into a new configuration. During this process magnetic energy is converted into kinetic energy, accelerated particles and heating. Ideal MHD theory doesn't allow the possibility of magnetic reconnection to take place since plasma and magnetic field are linked one to each other and evolve together according to the so called frozen-in condition. The frozen–in condition between the plasma and the magnetic field can be described as follows. The magnetic flux across a surface S, is defined as:

$$\psi = \int_S \mathbf{B} \cdot d\mathbf{S}$$

The flux can change in time if the magnetic field evolves in time (according to Faraday's law or if the surface moves:

$$\frac{d\psi}{dt} = \int_S \frac{d\mathbf{B}}{dt} \cdot d\mathbf{S} + \int_S \mathbf{B} \cdot \frac{d(\Delta\mathbf{S})}{dt}$$

where $\frac{d\mathbf{B}}{dt} = \frac{\partial \mathbf{B}}{\partial t} + (\mathbf{u} \cdot \nabla)\,\mathbf{B}$. In the hyphothesis of infinite conductivity, the Faraday plus ideal Ohm's law, see appendix A, give:

$$\frac{\partial \mathbf{B}}{\partial t} = -c\nabla \wedge \mathbf{E} = \nabla \wedge (\mathbf{u} \wedge \mathbf{B}) = (\mathbf{B} \cdot \nabla)\mathbf{u} - (\mathbf{u} \cdot \nabla)\mathbf{B} - \mathbf{B}(\nabla \cdot \mathbf{u})$$

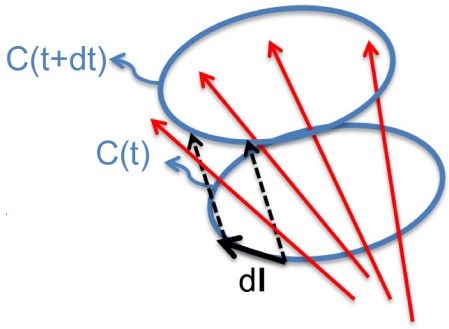

Figure 2: Surface S defined by the contour C in blu, the surface is moving in time from C(t) to C(t+dt). Magnetic flux is represented with red arrows, dl is the element of contour. . Image Credit: N. F Loureiro

The total derivative becomes then:

$$\frac{d\mathbf{B}}{dt} = \frac{\partial \mathbf{B}}{\partial t} + \mathbf{u}\cdot\nabla\mathbf{B} = (\mathbf{B}\cdot\nabla)\mathbf{u} - \mathbf{B}(\nabla\cdot\mathbf{u})$$

In figure 2 we show a generic surface S bounded by the contour $C(t)$ moving in a time dt to $C(t+dt)$ represented in blue; red arrows represent magnetic field lines. We will now show that the flux of magnetic field lines across the two contours is the same. Denoting the element of length along the contour as $d\mathbf{l}$, after a time increment dt the plasma element on the contour has moved by a surface $d\triangle\mathbf{S}$ given by $d(\mathbf{v}\delta t \wedge \delta\mathbf{l})$. If the surface is moving with the plasma, so $\mathbf{v} = \mathbf{u}$, the increment in the element of area is given by:

$$\frac{d\triangle\mathbf{S}}{dt} = \mathbf{u}\wedge d\mathbf{l}$$

$$\frac{d\psi}{dt} = \int_S \frac{d\mathbf{B}}{dt}\cdot d\mathbf{S} + \int_S \mathbf{B}\cdot\frac{d(\Delta\mathbf{S})}{dt} = \int_S \nabla\wedge(\mathbf{u}\wedge\mathbf{B})\cdot d\mathbf{S} + \int_C \mathbf{B}\cdot(\mathbf{u}\wedge d\mathbf{l}) =$$

$$= \int_S \nabla\wedge(\mathbf{u}\wedge\mathbf{B})\cdot d\mathbf{S} + \int_C \mathbf{B}\wedge\mathbf{u}\cdot d\mathbf{l} = \int_S [\nabla\wedge(\mathbf{u}\wedge\mathbf{B}) + \nabla\wedge(\mathbf{B}\wedge\mathbf{u})]\cdot d\mathbf{S} = 0$$

So the magnetic flux across a given surface is constant during the motion of the plasma. The frozen-in condition has been obtained using the ideal Ohm's law $\mathbf{E} + \mathbf{u}\wedge\mathbf{B}/c = 0$. This approximation is in general valid more or less everywhere since the plasma can be assumed as non collisional in the solar wind or, very often, in astrophysical environments. The frozen-in theorem force magnetic field lines to move with the plasma and vice versa. Magnetic reconnection means the possibility of breaking (locally) magnetic field lines with respect to the plasma flow by some non ideal effects in the Ohm's law at play

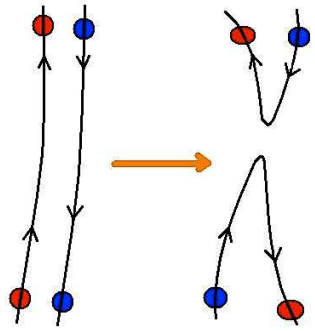

Figure 3: Example of magnetic reconnection, here two field lines of opposing polarity (indicated with blu and red spots). If they are pushed one to each other they reconnect dragging plasma with them.

in very thin regions characterized by the presence of strong gradients. These regions are called current sheets.

In figure 3 we show a simple scheme of the reconnection process. On the left, two antiparallel field lines are marked with blue and red spots marking plasma element. The initial direction of the field is given by the arrows. On the right the figure shows the configuration after the reconnection process in which field lines initially separated are now connected changing therefore magnetic field topology. To explain this process consider the two initial antiparallel field lines. As the instability sets-up, they are pushed closed to each other by a velocity perturbation. Then strong currents are generated corresponding to the local strong variation of the magnetic field in a region called 'current sheet'. Here the term $\mathbf{J}/\sigma$ in the Ohm's law becomes important, see appendix A for more details. As a consequence, ideal MHD is violated in this "dissipative or resistive region", where magnetic field and plasma decouple moving at different velocities. When magnetic field lines reconnect magnetic energy is converted into thermal and kinetic energy and accelerated particles; in particular magnetic tension trying to reduce the curvature of reconnected field lines accelerates plasma away from the reconnection point, in the so-called "reconnection jets". Considering figure 3 we can also observe that, once field lines have reconnected, there is a magnetic field component perpendicular to the initial direction of the magnetic lines, this is one of the important features typically used to recognize a reconnection process. There are different models of magnetic reconnection. In the 60's Sweet and Parker elaborated a model for describing resistive magnetic reconnection called today the 'Sweet-Parker model', that we will discuss in the next section.

1.3.0.1 *Sweet-Parker (SP) Model*

In the Sweet-Parker model, Ref. Sweet [114], Parker [88], magnetic reconnection is assumed to take place in a small "diffusion" region

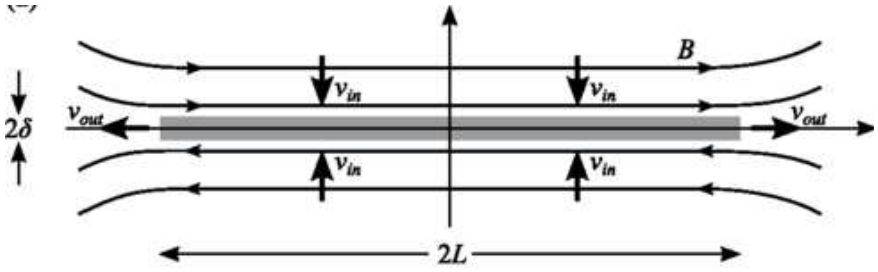

Figure 4: Figure taken and adapted from Ref. Comisso and Asenjo [18] showing the geometry of the Sweet-Parker configuration. Thick black arrows mark the inflow, v_{in}, and outflow, v_{out}, directions. The diffusion region, of length 2L and width 2δ, is grey shaded.

corresponding to the presence of a strong current sheet of length 2L and width 2δ with $\delta \ll L$. In figure 4 we show a simple scheme of this model, the diffusion region elongated in the x direction is grey shaded and it reveals the characteristic SP geometry longer than the width. The inflow and outflow regions are indicated with arrows in figure 4 showing the direction of the incoming plasma and how it is then pushed outside the diffusion region. Using Ideal Ohm's law the electric field in the inflow region is given by $E_{z,outside} = v_{inflow}B_{inflow}/c$ where B_{inflow} is the upstream magnetic field, see figure 4. Inside the current sheet instead $B = 0$. In this region, where fields approach each other, the resistive diffusion becomes important in the general Ohm's law, so that the electric field inside the diffusion region is given by $\mathbf{E}_{inside} \simeq \eta\mathbf{J}$. If we assume the flow is steady state, we can connect the two relations. Assuming E_z constant everywhere, we get $v_{inflow}B_{inflow}/c = \eta J_z = \eta\nabla \wedge B/4\pi \sim \eta B/\delta$ so that the inflow velocity is proportional to $v_{in} \sim \eta/\delta$. If the density is comparable on both sides and assuming incompressible flow, from continuity equation we have:

$$v_{in}L = v_{outflow}\delta \rightarrow v_{in} = \frac{\delta}{L}v_{outflow}$$

Pressure balance along the layer between the magnetic pressure at the centre of the layer and the dynamic pressure of the outflowing plasma gives:

$$\frac{B_{in}^2}{8\pi} = \rho\frac{v_{outflow}^2}{2}$$

The outflow velocity is assumed to be about the Alfvèn velocity:

$$v_{outflow} = \sqrt{\frac{B_{in}^2}{4\pi\rho}} \equiv v_A$$

Since $v_{in} = (\delta/L)v_{outflow} = (\eta/L)(v_{outflow}/v_{in})$ the inflow velocity can be written in terms of the Alfvèn velocity: $v_{in} = \sqrt{(\eta/L)}v_{outflow} =$

$\sqrt{(\eta/L)v_A}$. We estimate the reconnection rate using the inflow velocity, supposing that all the magnetic field lines advected into the layer are then reconnected:

$$\frac{v_{inflow}}{v_{outflow}} = \sqrt{\frac{\eta}{v_A L}} \tag{1}$$

From the induction equation:

$$\frac{\partial \mathbf{B}}{\partial t} = \nabla \wedge (\mathbf{u} \wedge \mathbf{B}) + \eta \nabla^2 \mathbf{B}$$

we define two characteristic times, the resistivive diffusion time $\tau_d = L^2/\eta$ and the dynamic Alfvèn time $\tau_A = L/v_A$. The Lundqvist number S is defined as the ratio of the diffusion and Alfvèn time: $S = \tau_d/\tau_A = v_A L/\eta$. We define $M = v_{inflow}/v_A$ the Alfvèn Mach number as an index of the reconnection rate; it follows from equation 1 that $M \approx S^{-1/2}$. In the solar corona the Lundquist number is $S \sim 10^{14}$, so $M = 10^{-7}$. As a result, according to Sweet-Parker theory, solar flares should last months, in contrast with the observed values $\tau_{flares} \backsim 10^3 s$. Sweet-Parker reconnection rate predicts indeed a too slow reconnection rate to account for the reconnection processes which take place in plasma. A reconnection mechanism faster than the Sweet-Parker model was introduced by Petscheck, who developed a reconnection model fast enough to justify measured reconnection rate in solar flares but it will not be discussed in this thesis.

1.3.0.2 *Hall-MHD reconnection*

Fast reconnection can occur in collisionless plasmas in the presence of anomalous resistivity or when dealing with Hall-MHD systems that allow for the transition from MHD towards a two fluid system. Let us consider the generalized Ohm's law (see appendix A):

$$\mathbf{E} + \mathbf{v} \wedge \mathbf{B} = \eta \mathbf{J} + \frac{\mathbf{J} \wedge \mathbf{B}}{ne} - \frac{\nabla \cdot P_e}{ne} + \frac{m_e}{ne^2} \frac{\partial \mathbf{J}}{\partial t}$$

When the typical scale length becomes comparable to the inertial ion length, $l \sim d_i$, the Hall term $J \wedge \mathbf{B}/ne$ becomes important. Ions are no longer magnetized while electrons are. As a result, the ion and electron velocities start to separate giving rise to a two-fluid dynamics. In figure 5 we show the geometry of a typical Hall collisionless reconnection process. Electron velocity is represented by dotted arrows while white and black shaded arrows show the inflow and outflow regions respectively. Electrons are advected in the current layer at velocity $\mathbf{E} \wedge \mathbf{B}/B^2$ building the Hall current $\mathbf{J_H} = -eNv_e = -eN\left(\mathbf{E} \wedge \mathbf{B}/B^2\right)$, as we have shown in figure 5. Electrons generate the quadrupolar Hall magnetic fields, B_H, signature along the separatrices. Ions are accelerated in the direction of the electric field pointing out of the plane and contributing to increase the strength of the current sheet.

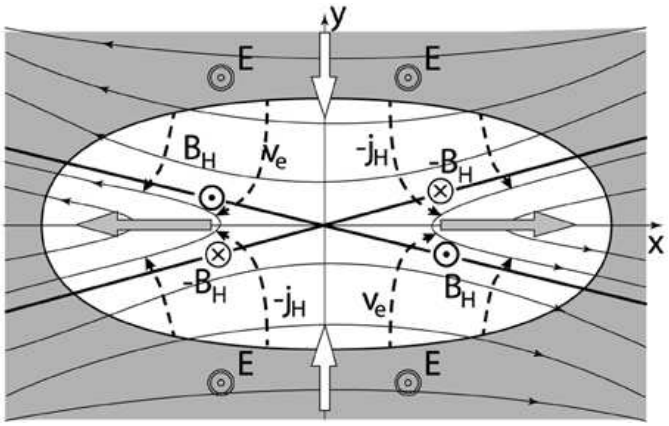

Figure 5: Geometry of the Hall collisionless reconnection, figure taken from Treumann and Baumjohann [120]. The reconnection layer thickness is smaller than the ion inertial length for reconnection to occur. Dotted lines shows the electron motion, white and gray arrows show the inflow and outflow directions respectively.

1.3.1 *Interplanetary Magnetic Field interaction with Geomagnetic field lines*

In this section we give an example of magnetic reconnection occurring at the magnetosphere, as it has been briefly discussed in section 1.1. In figure 6 two different configurations of the geomagnetic field are shown according to the interplanetary solar wind conditions. Magnetosphere is classified into "open" and "closed" configuration, top and bottom panel, respectively, according to how it interacts with the interplanetary magnetic field. During southward configurations, reconnection takes place both at the nose and at the tail between the solar wind field and northward Earth's magnetic field. In particular, reconnected field lines drag solar wind particles inside the magnetosphere, causing phenomena like auroras. During northward interplanetary magnetic field, instead, there is no dayside reconnection but reconnection takes place at the south and north geomagnetic poles. We already anticipated in section 1.1 that under this condition still cold dense solar wind plasma is observed in the Earth's magnetosphere together with a broad boundary layer at low latitude (LLBL) a region where a mixture of solar wind and magnetospheric populations, Ref. Fujimoto et al. [44], so other phenomena like Kelvin-Helmholtz instability must take place.

1.4 SPACE PLASMA DISCONTINUITIES

In space plasma, there are various discontinuities, some of them have been briefly introduced in section 1.2, like the bow shock and the magnetopause. A discontinuity is a transition region across which there is a variation of the field and plasma properties. Discontinuities

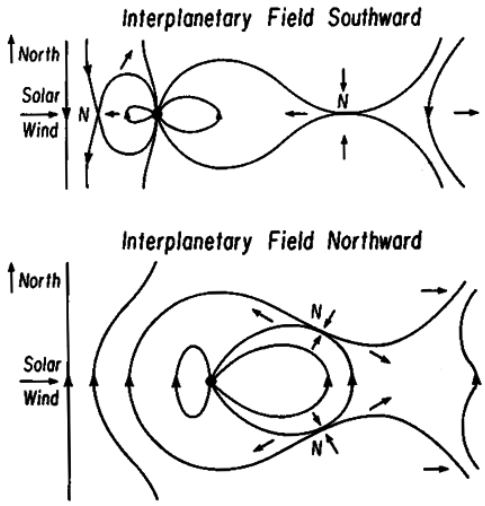

Figure 6: Image taken from Dungey [28] showing two magnetosphere configurations: open in the top figure and closed in the bottom. Arrows indicate the direction of the flowing plasma.

are classified into tangential or rotational discontinuities and shocks. In figure 7, taken from Ref. Burlaga [12], we show a scheme for two typologies of discontinuities, a tangential and a rotational discontinuity. A discontinuity is characterized as tangential when there is no mass or magnetic flux across it and the pressure on it is constant. A schematic representation of a tangential discontinuity is shown in the left panel in figure 7. The magnetic and the velocity fields can change across the discontinuity but there is no component normal to it, so $B_n = 0$ and $u_n = 0$, where n is the normal direction. The normal to the surface is determined by $B_1 \wedge B_2$ (both parallel to the discontinuity), here the subscripts mark the two different sides of the discontinuity, as shown in figure 7. In a rotational discontinuity, instead, the magnetic field direction change with a non-zero component normal to the current layer, as shown in the right panel in figure 7. The rotational discontinuity is characterized by a finite normal mass flow but a continuous v_n. The rotational discontinuity is not static and it propagates along the direction of the normal of the surface at the Alfvèn speed $v_A = B_n/\sqrt{4\pi\rho}$. A discontinuity is called a shock if there are both magnetic flux and mass flux across it and if there is a change in the density as well, sometimes the rotational discontinuity is classified also as a non-compressional shock because there is no density variation across the layer. Shocks are characterized by the coplanarity of the magnetic field, Ref. Belmont et al. [6], i.e. the magnetic field vectors on the two side of the shock are coplanar with the shock normal vector.

The magnetopause is a finite thickness discontinuity defined by the balance of the solar wind dynamic pressure and the magnetosphere magnetic pressure. According to the direction of the interplanetary

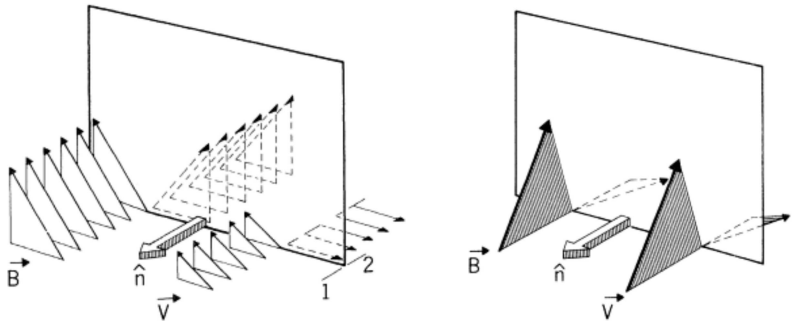

Figure 7: A schematic representation of a tangential discontinuity (left panel) and of a rotational discontinuity (right panel). Image Credit :Burlaga [12].

magnetic field it is classified as an open or closed magnetopause, these configurations correspond nearly to a rotational or a tangential discontinuity respectively. The closed magnetopause occurs when there is no magnetic reconnection between the solar wind and the geomagnetic field lines, as shown in the bottom in figure 6. The "open" magnetopause is a rotational discontinuity and it occurs when the IMF is directed southward and there is magnetic reconnection taking place at the dayside magnetopause, see top panel in figure 6. It has to be underlined here that a rotational discontinuity requires the continuity of some quantities across the discontinuity layer, like the normal velocity, the mass density, and the thermal pressure and that these are not often satisfied at the magnetopause. For this reason magnetopause is preferably defined as a "disturbed tangential discontinuity", Ref. Volland [127], having a small normal component of magnetic field, $B_n \gtrsim 0$.

1.5 PLASMA CHARACTERISTIC FREQUENCIES AND SCALES IN NEAR EARTH'S REGIONS

A plasma has a large number of characteristic scales. Of particular importance is the Debye length, which is the typical distance over which any charge imbalance is shielded by the electrostatic field. An isolated charge q generates an electrostatic potential $\phi_0(r) = q/4\pi r$ but, if we consider this particle in a plasma, then many particles with opposite sign will be attracted thus shielding its potential from the rest of the plasma (and vice versa). Let us consider a positive charge q in a neutral plasma; the number density of the electrons cloud is given by the Boltzmann distribution $n_e = n_\infty e^{e\phi/k_B T_e}$ with $\phi(r \to \infty) = 0$. One dimensional Poisson equation for the electrostatic potential is $\nabla^2\phi = d^2\phi/dx^2 = -4\pi e(n_i - n_e)$. Substituting the values of n_e and n_i it becomes: $d^2\phi/dx^2 = 4\pi e n_\infty(e^{e\phi/k_B T_e} - 1)$. Far from the influence of the electrostatic potential, i.e. when $|e\phi/k_B T_e| \ll 1$ the exponential

can be expanded as $d^2\phi/dx^2 = 4\pi e n_\infty \left[e\phi/k_B T_e + \frac{1}{2}(e\phi/k_B T_e)^2 + ...\right]$. Keeping first order terms we can write $d^2\phi/dx^2 = 4\pi n_\infty \left(e^2/k_B T_e\right)\phi$. By defining the Debye length as $\lambda_D = \sqrt{k_B T_e/4\pi n e^2}$, the electrostatic potential turns out to be $\phi = \phi_0 e^{-x/\lambda_D}$. As result, the plasma beyond the Debye sphere is neutral. The number of particles in a Debye sphere is $N = 4/3\pi n \lambda_D^3 \propto n\lambda_D^3$, the shielding of individual charge is efficient if N is much larger than unity. It is usually convenient to deal with dimensionless quantities, for this reason we define the plasma parameter g as:

$$g = \frac{1}{n\lambda_D^3}$$

This number is very small when there are many electrons in a Debye sphere and since it is proportional to the ratio of potential energy over kinetic energy, it means that the average potential energy must be (much) less then the avarage kinetic energy. This is also a measure of the dominance of collective interactions over single particle interactions. Indeed if g is small the number of electrons in a Debye sphere is large, less likely there will be a significant force on a particle due to "collisions", e.g. Coulomb interaction with nearby particles with respect to the interaction with the full system. An example of collective interactions are plasma oscillations. If for example in a plasma made by electrons and ions, we imagine to displace a certain amount of electrons (or ions) with respect to their original configuration, then the electric force will try to restore the system to its original position. Plasma electrostatic waves are then generated and the electrons oscillate at the plasma frequency, defined as:

$$\omega_{p,e} = \sqrt{\frac{4\pi n_e q_e^2}{m_e}}$$

Another important set of frequencies used in the electromagnetic kinetic applications are the electron and ion cyclotron frequencies. If we consider a charged particle moving perpendicular to a uniform magnetic field, due to the Lorentz force the particle gyrates around the magnetic field. The circular motion has a radius called "Larmor radius", $\rho_{Le,i} = v_\perp/\Omega$ where $\Omega_{c,e,i} = qB/m_{e,i}c$ is known as "cyclotron frequency".

Going back to the characteristic plasma scales, in addition to the Debye length there are other two important scales associated to the frequencies described above. The electron (ion) inertial length $d_{e,i} = c/\omega_{pe,pi}$ and the gyro-radius, already described above and also called 'Larmor radius' $\rho_{e,i} = v_{th}/\Omega_{ce,ci}$. In the non relativistic limit: $\lambda_D \ll \rho_{e,i} \ll d_{e,i}$. These scales help to define an ordering in the plasma. According to the characteristic scales of the interested phenomena

the plasma can be described using different approximations. Fluid plasma description, for example, deals with scales much larger than both $\rho_{e,i}$ and $d_{e,i}$. Moreover in the fluid limit the time scale of fluid phenomena is larger than the time response of the electrons, proportional to $\omega_{p,e}^{-1}$ so it has consequences in the frequency domain, dealing with $\omega \ll \omega_{p,e}$ (low frequency regime). A kinetic plasma description is instead used for scales smaller than the ion inertial length.

1.6 KELVIN-HELMHOLTZ AND RAYLEIGH-TAYLOR INSTABILITIES

Let us now consider the main driver of our system, the Kelvin-Helmholtz instability. It originates any time two layers of a fluid (or two different fluids) are in relative motion. In a plasma, it can be stabilized by a magnetic field directed along the flow due to magnetic tension. In the case of the shear flow between the solar wind and the magnetosphere, when the IMF is northward, the equatorial component of the magnetic field can be negligeable at low latitude and so the K-H instability can develop eventually producing fully rolled-up vortices. Such vortices have been observed by Cluster satellites, see Ref. Hasegawa [54], Hasegawa et al. [50, 52] at the magnetopause.

1.6.1 *Hydrodynamic case*

Let now consider the physical mechanism of the K-H instability in the hydrodynamics limit. An intuitive description of this instability can be found in the work of Ref. Drazin and Reid [25] and Batchelor [4] that present the instability in terms of the dynamics of the vorticity evolution. In figure 8 we show the schematic representation of two fluids moving at two different velocities separated by an horizontal boundary at $z = 0$. The velocity $\mathbf{U}(z)$ is defined as:

$$\mathbf{U}(z) = \begin{cases} U_1 & (z < 0) \\ U_2 & (z > 0) \end{cases}$$

where $U_1 = -V_0$ is the velocity of the lower fluid, indicated as fluid 1 and it is directed in the negative x-direction while the upper fluid has velocity $U_2 = +V_0 > 0$ directed in the positive x-direction. The two fluids have densities ρ_1 and ρ_2 in the regions $z < 0$ and $z > 0$ respectively. The vertical displacement of the sheet is indicated as $z = \zeta(x, t)$. Points A and C are characterized by zero displacement, as we can observe in figure 8, so $\zeta(x_A, t) = 0 = \zeta(x_C, t)$. In the two dimensional (x, z) representation of the velocity discontinuity in figure 8, we consider an initial sinusoidal perturbation, represented with a thick continuous black line and we observe the evolution of the vorticity, marked with arrows.

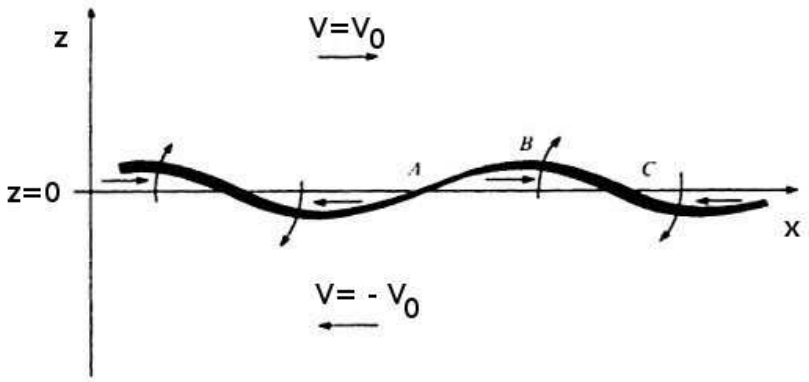

Figure 8: Image taken from Batchelor [4], Drazin and Reid [25], representing the evolution of a sinusoidal perturbation in terms of vorticity in the (x, z) plane. Arrows reveal the direction of vorticity, showing points where it accumulates (i.e. point C in figure).

Defining the velocity field as $\mathbf{U} = (u, v, w)$, the vorticity of the sheet is $\omega = \nabla \wedge \mathbf{U} = \hat{e}_y \, (\partial_z u - \partial_x w)$ and it is positive where $V_0 > 0$. Vorticity leaves points like A where $\partial\zeta(x,t)/\partial x > 0$ and accumulates around points like C where $\partial\zeta(x,t)/\partial x < 0$; where the fluid is displaced downwards ($w < 0$) the vorticity induces a positive velocity in the x–direction $u > 0$ where $z > 0$ and vice versa, for example in points like B where a positive vorticity is induced from both sides. Vorticity accumulating in points like C induces an increase of the amplitude of the perturbation leading to larger and larger clockwise velocities at these points. This intuitive description of the Kelvin-Helmholtz instability, will now be supported by a mathematical derivation of the dispersion relation, Ref. Chandrasekhar [16]. For the sake of mathematical simplicity, the flow is assumed as an incompressible potential flow:

$$\begin{cases} U_1 = \nabla\phi_1 \\ U_2 = \nabla\phi_2 \end{cases} \tag{2}$$

The elevation of the disturbance is $z = \zeta(x, y, t)$. Potentials can be written as $\phi_2 = U_2 x + \phi_2'$ (for $z > \zeta$) and $\phi_1 = U_1 x + \phi_1'$ (for $z < \zeta$) and they must satisfy Laplace equation. The vertical velocity at $z = 0$, $U_z = d\zeta/dt$, can be written as:

$$\frac{\partial\phi_i}{\partial z} = \frac{d\zeta}{dt} = \frac{\partial\zeta}{\partial t} + \frac{\partial\phi_i}{\partial x}\frac{\partial\zeta}{\partial x} + \frac{\partial\phi_i}{\partial y}\frac{\partial\zeta}{\partial y} = w \; (z = \zeta, \, i = 1, 2) \tag{3}$$

The motion equation of an incompressible flow (with constant density) is shown in equation 4, where $\mathbf{g}$ is the gravity acceleration.

$$\begin{cases} \rho\left(\frac{\partial u}{\partial t} + U\frac{\partial u}{\partial x} + w\frac{dU}{dz}\right) = -\frac{\partial \delta P}{\partial x} \\ \rho\left(\frac{\partial v}{\partial t} + U\frac{\partial v}{\partial x}\right) = -\frac{\partial \delta P}{\partial y} \\ \rho\left(\frac{\partial w}{\partial t} + U\frac{\partial w}{\partial x}\right) = -\frac{\partial \delta P}{\partial z} - \mathbf{g}\delta\rho \end{cases} \tag{4}$$

Continuity equation in the incompressible case read:

$$\frac{\partial \rho}{\partial t} + U\frac{\partial \delta\rho}{\partial x} + w\frac{d\rho}{dz} = 0 \tag{5}$$

and the incompressibility condition:

$$\frac{\partial u}{\partial x} + \frac{\partial v}{\partial y} + \frac{\partial w}{\partial z} = 0 \tag{6}$$

Analyzing the disturbances by a normal modes analysis, i.e. all quantities in the form $e^{i(k_x x + k_y y + \Omega t)}$, equations 3 - 6 become:

$$\begin{cases} i\Omega\rho u + \rho U i k_x u + \rho w D U = -i k_x \delta P \\ i\Omega\rho v + \rho U i k_x v = -i k_y \delta P \\ i\Omega\rho w + \rho U i k_x w = -D\delta\rho - g\delta\rho \end{cases} \tag{7}$$

$$i\Omega\delta\rho + U i k_x \delta\rho = -w D\rho \tag{8}$$

where $D = d/dz$ is the total derivative. The velocity along z can be written as:

$$i\Omega\zeta + U i k_x \zeta = w \tag{9}$$

and $\nabla \cdot \mathbf{u} = 0$ as:

$$i k_x u + i k_y v + Dw = 0 \tag{10}$$

Multiplying the first of the equations 7 by $-ik_x$ and the second by $-ik_y$ and using both of them in equation 10, we obtain:

$$\rho(\Omega + i k_x U) Dw - i k_x \rho (DU) w = -k^2 \delta p \tag{11}$$

where $k = \sqrt{k_x^2 + k_y^2}$. By combining the third of the equation 7 with equation 9 and 10, we get:

$$i\rho(\Omega + i k_x U) w = -D\delta p - g\frac{i w D\rho}{\Omega + i k_x U} \tag{12}$$

Finally, using the expression of δp from equation 11, this equation at the interface ($z = 0$) becomes:

$$D\{\rho(\Omega + ik_x U)Dw - \rho k_x (DU)w\} - \rho k^2(\Omega + ik_x U)w = \\ = gk^2 D\rho \frac{w}{\Omega + ik_x U} \tag{13}$$

Since $\nabla^2\phi_i = 0 \rightarrow \dfrac{d^2\phi_i}{dz^2} = -(k_x^2 + k_y^2)\phi_i = -k^2\phi_i$ the solution has the form:

$$\hat{\phi}_i(z) = A_i e^{kz} + B_i e^{-kz}$$

The perturbation must be localized around the sheared region and rapidly disappear elsewhere, $\mathbf{U}(z \rightarrow \pm\infty) \rightarrow 0$. This requires that, for $z > 0$, $B_1 = 0$ and $\hat{\phi}_1(z)$ becomes $\hat{\phi}_1(z) = A_1 e^{kz}$. For the same reason, we obtain $A_2 = 0$, $\hat{\phi}_2(z) = B_2 e^{-kz}$. Using the expression of $\hat{\phi}_{1,2}(z)$ in equation 3 at the interface ($z = 0$), we can obtain the values of the constants A_1, B_2. The velocity in the z direction takes the form:

$$\begin{cases} w_1 = A(\Omega + ik_x U_1)e^{kz} \\ w_2 = A(\sigma\Omega + ik_x U_2)e^{-kz} \end{cases} \tag{14}$$

Equation 13 is integrated across the surface over an infinitesimal element $z_s + \epsilon$ and $z_s - \epsilon$.

$$\int_{z_s-\epsilon}^{z_s+\epsilon} \{\rho(\Omega + ik_x U)Dw - \rho k_x (DU)w\}\, dz = \int_{z_s-\epsilon}^{z_s+\epsilon} \left[gk^2\rho \frac{w}{\Omega + ik_x U}\right] dz \tag{15}$$

Taking the limit $\epsilon \rightarrow 0$, can be written and using the solution for the vertical velocity, in equation 14, the equation 15 gives, after some algebra:

$$\rho_2(\Omega + ik_x U_2)^2 + \rho_1(\Omega + ik_x U_1)^2 = gk\{\rho_1 - \rho_2\} \tag{16}$$

From this equation we can deduce the dispertion relation:

$$\Omega = -\frac{k_x(\rho_1 U_1 + \rho_2 U_2)}{\rho_1 + \rho_2} \pm \left[gk\frac{(\rho_1 - \rho_2)}{\rho_1 + \rho_2} + -k_x^2 \frac{\rho_1\rho_2}{(\rho_1 + \rho_2)^2}(U_2 - U_1)^2\right]^{1/2} \tag{17}$$

Instability occurs when $gk\left(\rho_2^2 - \rho_1^2\right) < k_x^2\rho_1\rho_2\left(U_2 - U_1\right)^2$. Therefore, in the case in which the two densities are equal, any time a velocity

shear exists the system is unstable for KH. In general, for a given velocity jump and a perturbation wavevector **k** along the flow **U** the instability occurs for

$$k > \frac{g\left(\rho_2^2 - \rho_1^2\right)}{\rho_1 \rho_2 \left(U_2 - U_1\right)^2} \equiv k_{min}$$

there is always a critical wavenumber, k_{min}, above which the system is unstable. So the instability can always develop even on a stratified interface, as long as its wavelength is small enough. In the real case, the discontinuity has a finite shear length L. Therefore small wavelengths perturbations, $\lambda \ll L$, are stabilized since they do not "see" the velocity gradient.

1.6.1.1 *Rayleigh-Taylor*

If the fluid is denser in the region $z > 0$, i.e. $\rho_1 < \rho_2$, considering the two fluids moving at the same velocity, the system is also unstable:

$$\Omega_{RT} = -\frac{k_x(\rho_1 U_1 + \rho_2 U_2)}{\rho_1 + \rho_2} \pm \left[gk\frac{(\rho_1 - \rho_2)}{\rho_1 + \rho_2} \right]^{1/2}$$

This instability is known as the Rayleigh-Taylor (RT) instability and it takes place when two fluids with different densities are superposed or they are accelerated towards each other.

1.6.2 *Magnetohydrodynamic case*

In a plasma K-H instability can be stabilized by magnetic field $\mathbf{B} = (B + b_x, b_y, b_z)$, directed along the flow direction, see Ref. Chandrasekhar [16]. In the magnetoydrodynamic limit, the relevant equations must include the magnetic force, they become:

$$\rho\left(\frac{\partial \mathbf{U}}{\partial t} + \mathbf{U}\cdot\nabla\mathbf{U}\right) = -\nabla P + \rho\mathbf{a} + \frac{1}{4\pi}\left(\nabla \wedge \mathbf{B}\right)\wedge\mathbf{B} \tag{18}$$

component by component:

$$\begin{cases} \rho\frac{\partial u}{\partial t} + \rho U\frac{\partial u}{\partial x} + \rho w\frac{dU}{dz} = -\frac{\partial P}{\partial x} \\ \rho\frac{\partial v}{\partial t} + \rho U\frac{\partial v}{\partial x} = -\frac{\partial P}{\partial y} + \frac{B}{4\pi}\left(\frac{\partial b_y}{\partial x} - \frac{\partial b_x}{\partial y}\right) \\ \rho\frac{\partial w}{\partial t} + \rho U\frac{\partial w}{\partial x} = -\frac{\partial P}{\partial z} - g\delta\rho + \frac{B}{4\pi}\left(\frac{\partial b_z}{\partial x} - \frac{\partial b_x}{\partial z}\right) \end{cases}$$

We add the Faraday equation to calculate the magnetic field and we use the Ohm law for the **E** field. In the MHD limit:

$$\mathbf{E} = -\frac{\mathbf{U}\wedge\mathbf{B}}{c}$$

The induction equation reads:

$$\frac{\partial \mathbf{B}}{\partial t} = \nabla \wedge (\mathbf{U} \wedge \mathbf{B}) = (\mathbf{B} \cdot \nabla)\mathbf{U} - (\mathbf{U} \cdot \nabla)\mathbf{B}$$

by expliciting the gradients:

$$\frac{\partial \mathbf{B}}{\partial t} + U\frac{\partial \mathbf{B}}{\partial x} = B\frac{\partial u}{\partial x} + b_z\frac{dU}{dz} \tag{19}$$

Solenoidal equation for B is also included:

$$\frac{\partial b_x}{\partial x} + \frac{\partial b_y}{\partial y} + \frac{\partial b_z}{\partial z} = 0 \tag{20}$$

Analysing the disturbance in normal modes as before, the dispertion relation is given by:

$$\Omega = -k_x\frac{\rho_1 U_1 + \rho_2 U_2}{\rho_1 + \rho_2} \pm$$

$$\pm \left[\frac{gk(\rho_1 - \rho_2)}{\rho_1 + \rho_2} + \frac{k_x^2 B^2}{4\pi(\rho_1 + \rho_2)} - k_x^2\frac{\rho_1\rho_2}{(\rho_1 + \rho_2)^2}(U_1 - U_2)^2\right]^{1/2} \tag{21}$$

[see Ref. Chandrasekhar [16] for algebra details]. The main information we can extract from this formula is that a magnetic field in the flow direction can actually inhibit the Kelvin-Helmholtz instability by acting as a magnetic tension (in analogy with the hydrodynamic case). If:

$$\frac{\rho_1\rho_2}{(\rho_1 + \rho_2)^2}(U_1 - U_2)^2 \leqslant \frac{B^2}{4\pi(\rho_1 + \rho_2)}$$

the instability is suppressed. In other words if the velocity jump $\Delta U = (U_1 - U_2)$ doesn't exceed the mean Alfvèn speed the system is stable

$$U_1 - U_2 \leqslant \sqrt{\frac{B^2}{4\pi}\left(\frac{1}{\rho_1} + \frac{1}{\rho_2}\right)} \equiv \bar{v_A}$$

2

MODELLING KELVIN-HELMHOLTZ INSTABILITY USING A TWO FLUID CODE

Many numerical simulations have been performed, in the past literature, to model the interface between the Solar Wind and the magnetosphere with the purpose to study the development and evolution of the Kelvin-Helmholtz instability. In the next sections we give a brief overview of the past numerical simulations, section 2.1, and describe the two fluid code used in this thesis, section 2.2.

2.1 NUMERICAL SIMULATIONS OF KELVIN-HELMHOLTZ INSTABILITY

The role of this instability, in the plasma transport mechanism, has been investigated using mostly fluid models, as for example magnetohydrodynamic (MHD) simulations, Ref. Miura [75, 76], Otto and Fairfield [86].

These simulations have shown an increase of the initial velocity shear layer caused by anomalous momentum transport, consistently with the transport required to form the observed LLBL. Plasma transport has been studied in details also in Ref. Nykyri and Otto [83], where, using a 2D MHD simulations, authors focused instead on the magnetic reconnection process occurring in the thin current layers generated by the anti-parallel magnetic field twisted during vortex motion. Authors found the mass transport estimation in agreement with observations of Ref. Fujimoto et al. [44]. Since the layer across which K-H develops is narrow, with typical thickness around one inertial length, Hall-MHD simulations have been performed as well, showing important differences with respect to the MHD simulations, allowing faster broadening of the velocity layer, see Ref. Huba [60] and turbulence development. During the non-linear evolution of the instability, gradients of smaller scales are formed of the order of the ion inertial length or less, these gradients cause the development of secondary instabilities, e.g. secondary K-H, secondary Rayleigh- Taylor instability (in presence of a density jump), Ref. Faganello et al. [30], Tenerani et al. [116], Matsumoto and Hoshino [72], or magnetic reconnection. These processes have been analysed using two fluid simulations, Ref. Faganello et al. [31, 33, 32], Henri et al. [56], Palermo

et al. [87], Nakamura et al. [81]. Hybrid particle in cell (PIC) simulations, Ref. Cowee et al. [19, 20] and full PIC simulations, Ref. Nakamura et al. [82], Wan et al. [130], Karimabadi et al. [62] are used to study the kinetic effects at play during the evolution of the instability, these simulations have recently confirmed that secondary instabilities help the efficiency of plasma mixing inside the vortex itself, Ref Matsumoto and Hoshino [73] and validated the results of the fluid codes, Ref. Henri et al. [57]. Indeed, the effect of the small kinetic scales on the large scales is not dominant during the instability evolution and fluids codes are well suited to study the non linear phase of magnetized shear flow.

2.2 TWO FLUID CODE

The Two-Fluid code has been developed in Pise by the Plasma Physics group and it has been widely used to study different aspects of the K-H instability, see for example Ref. Faganello et al. [30, 31], Palermo et al. [87], Henri et al. [56]. The numerical code integrates the two fluid equations using dimensionless variables obtained normalizing to ion characteristic quantities, i.e. the ion mass, m_i, the Alfvàn velocity, v_A, the ion inertial length, d_i and the ion cyclotron frequency, Ω_{ci}. The code uses the following characteristic quantities (dimensionless variables are marked with a hat):

$$\hat{l} = l/d_i; \quad \hat{t} = t\Omega_{ci}; \quad \hat{v} = v/v_A; \quad \hat{m} = m/m_i$$

$$\hat{n} = n\frac{4\pi e^2 v_{A,i}^2}{m_i c^2 \Omega_{ci}^2}; \quad \hat{\mathbf{B}} = \mathbf{B}\frac{e}{m_i c \Omega_{ci}}; \quad \hat{P} = P\frac{4\pi e^2}{m_i^2 c^2 \Omega_{ci}^2}; \quad \hat{T} = T\frac{1}{m_i v_{A,i}^2}$$

where $\hat{n}$, $\hat{\mathbf{B}}$,$\hat{P}$ and $\hat{T}$ are respectively the dimensionless density, magnetic field, pressure and temperature. The quasi neutrality is assumed, $n_i \sim n_e \sim n$ (where n_i and n_e are the ion and electron densities) and in the low-frequency regime, $\omega \ll \omega_p$, the displacement current is neglected, where ω_p is the plasma frequency. The Ampère law reads:

$$\nabla \wedge \mathbf{B} = \mathbf{J} = n(\mathbf{u_i} - \mathbf{u_e}) \tag{22}$$

where $\mathbf{u}_i$ and $\mathbf{u}_e$ are the ion an electron velocities respectively. In this work, we integrate the *Hall-MHD* system of equations. The integrated equations are:

- the continuity equation

$$\frac{\partial n}{\partial t} + \nabla \cdot (n\mathbf{U}) = 0$$

- the motion equation

$$\frac{\partial (n\mathbf{U})}{\partial t} = -\{\nabla \cdot [n(\mathbf{UU}) + P_{tot}] - \mathbf{B} \cdot \mathbf{B}\}$$

where $\mathbf{U} = \mathbf{u_i}$ is the ion fluid velocity and P_{tot} is the total pressure, defined as $P_{tot} = P_e + P_i + B^2/8\pi$, here the subscripts e, i refer to electron and ion pressures. Adiabatic closures are used for both ions and electrons, Ref. Faganello et al. [31], Smets et al. [109]:

$$\frac{d}{dt}\left(P_{e,i} n^{-\gamma}\right) = 0 \tag{23}$$

with $\gamma = 5/3$ the polytropic index. For each species we define the quantity $S_{e,i} = P_{e,i} n^{-\gamma}$ and by multiplying the eq. 23 by the numerical density and using the continuity equation we can write the adiabatic closure in a conservative form:

$$\frac{\partial (nS_{e,i})}{\partial t} + \nabla \cdot (nS_{e,i}\mathbf{u}_{e,i}) = 0$$

The electric field, $\mathbf{E}$, is calculated through the generalized Ohm's law:

$$\mathbf{E} = -\mathbf{u}_i \times \mathbf{B} + \frac{\mathbf{J} \times \mathbf{B}}{n} - \frac{1}{n}\nabla P_e = -\mathbf{u}_e \times \mathbf{B} - \frac{1}{n}\nabla P_e$$

this expression contains the Hall term, $\mathbf{J} \times \mathbf{B}/n$, with $\mathbf{J}$ the current density, that becomes important when the system develops structures of scales of the order of one inertial length, i. e. when the ions dynamics starts to decouple from the magnetic field. The details on the numerical code can be found in Appendix B

3

SPACECRAFT OBSERVATIONS IN NEAR EARTH'S SPACE

In this chapter we describe the observations of the Kelvin-Helmholtz instability in space plasmas, section 3.1 and describe the satellites missions used in this thesis, section 3.2. A brief introduction to some of the methods used for satellite data analysis is provided in section 3.3.

3.1 EARLIER OBSERVATIONS OF KELVIN-HELMHOLTZ

The Kelvin-Helmholtz is a fluid instability that can be found everywhere in nature from fluids to space plasma environments. In figure 9, we report some examples of K-H observed in different astrophysical regions. It is indeed it is thought to act in disk accreting stars Ref. Lovelace et al. [70], Vietri and Stella [125], cometary tails, Ref. Ershkovich [29], sheared flows in the solar corona Kopp [63], Ofman and Thompson [85], see top left panel of figure 9, during coronal mass ejections, see top right panel in figure 9 from Ref. Foullon et al. [40], in planet's environments like Mercury, Ref. Boardsen et al. [8], Sundberg et al. [112], on Jupiter and on Saturn, bottom right and left panels respectively, Ref. Masters et al. [71], on Venus, Ref.Walker et al. [129] and at the Earth's magnetopause, Ref. Miura [75], Hasegawa et al. [50].

In particular in this thesis we focus on the Kelvin-Helmholtz instability occurring at the Earth's magnetopause. The magnetopause is a complex boundary, a transition region between the Solar Wind and Earth's magnetosphere, this region is of large interest because of the large variety of phenomena taking place. Observations have demonstrated that low latitude magnetopause is unstable to the Kelvin-Helmholtz instability, Ref. Hones et al. [58], Fairfield et al. [34], Hasegawa et al. [52, 53], Foullon et al. [37]. In particular the recent multipoint spacecraft measurements by Cluster satellites have revealed unambiguosly the presence of structures compatible with K-H vortices at the magnetopause, see Ref. Hasegawa et al. [50], Foullon et al. [37] and at the magnetotail, Ref. Fairfield et al. [34], Volwerk et al. [128]. The non-linear evolution of this instability drives the formation of secondary instabilities, like secondary K-H or in presence of a density

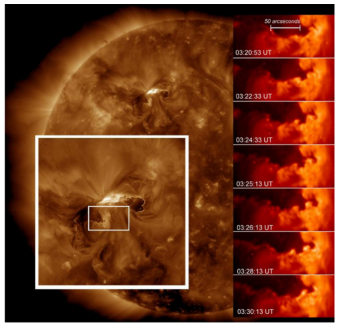

(a) Coronal mass ejection in the 211 Å, image taken from the Solar Dynamics Observatory/ Atmospheric Imaging Assembly (SDO/AIA). The white box is a zoom on the erupting structure and the smaller white box highlights the region where K-H vortices are observed. Frames on the right shows the temporal evolution of the vortices. Image credit: Ofman and Thompson [85]

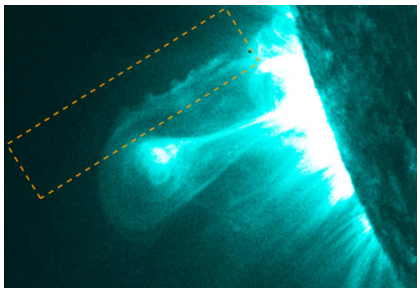

(b) Kelvin-Helmholtz waves observed in on a coronal mass ejection, image taken inthe 193 Å by Solar Dynamics Observatory/ Atmospheric Imaging Assembly (SDO/AIA). Image credit: Foullon et al. [40]

(c) K-H observed in Jupiter's storms by a Voyager 2. Photo credit: National Aeronautics and Space Administration (NASA).

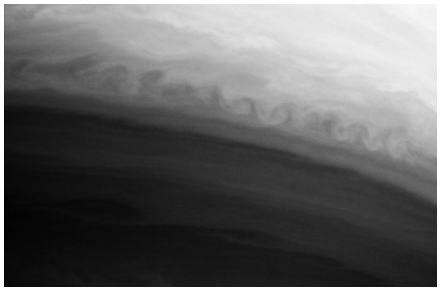

(d) K-H waves appearing in between the bands of Saturn. Image Credit: NASA/Cassini

Figure 9: Examples of K-H instability in different astrophysical environments.

shear of the Rayleigh-Taylor instability. In particular magnetic reconnection is another process induced by K-H evolution, Ref. Hasegawa et al. [53], Nykyri et al. [84].

All these processes contribute to the formation of the broad boundary layer. Yet, the exact processes responsible for plasma transport occurring inside K-H vortices are not fully understood. Some of these processes are occurring at kinetic scales where the frozen-in condition for particle is violated. Small–scale magnetic reconnection inside vortices is a very important example of such processes. Numerical simulations help to understand the small scale phenomena taking place during K-H evolution. Different numerical models are used to study the interface between the Solar Wind and the Magnetosphere, depending on the scale of the phenomena of interest. One important aspect, that has emerged in simulations, is the choice of the initial conditions. The large scale fields profiles of velocity, density, magnetic field, etc., used as initial conditions, strongly influence the dynamics of the magnetopause. In particular in the control of the evolution of the primary K-H instability and therefore the initial configuration over which vortex pairing and /or secondary instabilities develops and compete. So the final configuration of the system is strongly controlled by the initial condition. Numerical simulation are initialized with profiles reproducing typical configuration across the magnetopause, like using a velocity or density shear analogous to the one observed as crossing magnetopause. But, the exact details like the width of the shears or the total jumps of the profiles are often chosen to reduce computational time or to focus on one particular aspect of the instability. It is however very important to use the closest initial condition to the real ones to reproduce correctly the physics of this region. For this reason as discussed in the Introduction, Sec.1.1, in this thesis we will combine satellite data with numerical simulations. The initial large scale profiles are obtained from satellites crossings of the magnetopause during conditions that are favorable for the K-H, without the instability being already developed. In this chapter we will give a brief description of the satellites missions considered in this thesis.

3.2 RECENT SPACECRAFT MISSIONS

From 1958 to nowadays a large number of space observing missions have been developed; among them we use data from the European Cluster quartet (*sci.esa.int/cluster*); the Japanese space weather satellite GEOTAIL (*http://science.nasa.gov/missions/geotail/*) and the American ACE satellite (*http://science.nasa.gov/missions/ace/*).

Figure 10: Artist's view of the Cluster spacecraft quartet. Image credit: ESA

3.2.1 *Cluster Mission*

The Cluster mission, lead by American and European teams as principal investigators, was launched in 2000. It is made of four identical satellites travelling in tetrahedal configuration in an elliptic polar orbit, with a perigee around 19,000 km and and apogee of about 119,000 km, with a period of 57 hours. The size of the tetrahedron is varied during the mission; the interspacecraft distance during the mission goes form about 200 km up to 20,000 km. The diameter of each satellite is 2.9 m with an high of 1.3 m. In figure 10 we show an artist's view of the four Cluster satellites.

Using four identical spacecraft is an important innovation for disentangling spatial and temporal variations. Indeed, for the first time there are simultaneously four points measurements that allow the derivation of differential plasma quantities. All satellites of the Cluster quartet have the same instruments onboard measuring density, velocity and distribution functions of charged particles as well as electrical and magnetic fields. In table 1 we list the onboard instruments.

In this thesis we will focus on the density and the velocity profiles. In particular, the density is obtained using the spacecreft potential measured by EFW while the ion velocity is provided by CIS instrument.

3.2.1.1 *EFW Experiment*

The measured high time resolution (0.2 s) potential difference between the spacecraft and the probes in the EFW experiment is used to obtain the electric field and high resolution electron density measurements, Ref. Laakso et al. [65], Laakso and Pedersen [64], Pedersen et al. [91]. This is of particular importance in order to analyse with accuracy the density gradients occuring at the magnetopause. The EFW

Instruments Onboard of Cluster Satellites	
FGM	Fluxgate Magnetometer
EDI	Electron Drift Instrument
EFW	Electric Field and Wave experiment
DWP	Digital Wave Processing experiment
STAFF	Spatio-Temporal Analysis of Field Fluctuation experiment
WHISPER	Waves of High frequency and Sounder for Probing of Electron density by Relaxation experiment
WBD	Wide Band Data instrument
CIS	Cluster Ion Spectrometry experiment
PEACE	Plasma Electron And Current Experiment
RAPID	Research with Adaptive Particle Imaging Detectors
ASPOC	Active Spacecraft Potential Control experiment

Table 1: Table describing the 11 instruments onboard of Cluster satellites.

experiment is working on two of the four Cluster satellites (Cluster 2 and 4). It is made of four sensors mounted on two couple of wire booms in the spin satellite plane. From the measured potential difference between the probes the in plane Electric Field is estimated while the third component, along the spin axis, is constructed assuming $E \cdot B = 0$, Ref. Gustafsson et al. [47]. The spacecraft-to-probe potential difference is related to the ambient electron density. A method to estimate the electron density from potential is to derive empirically the curve N_e versus the potential difference, $V_{s/c} - V_{probe}$, where $V_{s/c}$ and V_{probe} are the spacecraft and probe potential respectively. This is possible by combining the measures of the density data derived by WHISPER instrument (see next section) with the potential difference, $V_{s/c} - V_{probe}$, measurements of EFW in the same region. By calibrating both measurements high resolution density data are obtained. In figure 11, we report a plot taken from Ref. Pedersen et al. [90], showing the density versus potential difference, $V_s - V_p$. The curve is recovered in different plasma regions for Cluster, from the solar wind to the magnetosphere and it is obtained from a comparison between WHISPER and EFW experiments. The orange curve refers instead to another satellite, POLAR. Here the differences between the two curves are linked probably to the different period in which the measurements were taken, during a solar minimum for POLAR and during a solar maximum for Cluster.

The Swedish Institute of Space Physics, Uppsala Division, is responsible of the EWF experiment and a useful guide to this instrument is the website of this experiment, *http://cluster.irfu.se/*.

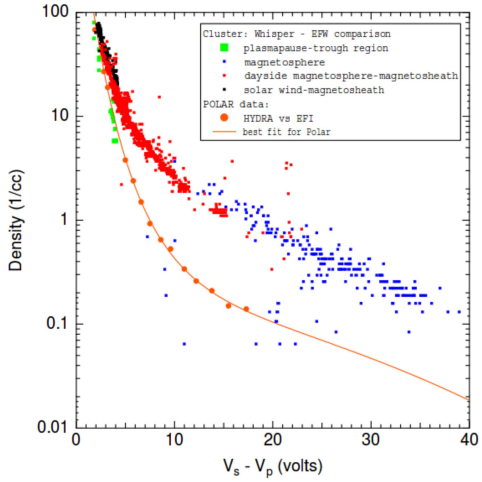

Figure 11: Density WHISPER measurements as a function of the potential difference between the spacecraft and the probe, $V_s - V_p$, for various plasma regions. In orange the same quantity estimated using POLAR satellite. Image Credit: Pedersen et al. [90]

3.2.1.2 *WHISPER experiment*

The WHISPER experiment consists of a pulse transmitter, a receiver and a wave spectrum analyser. Figure 12 is taken from Ref. Trotignon et al. [121] and it is particularly clear to show how this instrument works.

The transmitter sends a wave train at a given frequency (in short a time period around 1 ms) and the signal echo is recordered by the receiver, tuned to the same frequency, few millisecond later. The transmitter is connected to the outer conductive braids of one of the electric field antennae, shown in red in figure 12. The receiver, covering the $2 - 80\,\mathrm{kHz}$ band, is connected to each couple of conductive spheres antennae and it is possible to switch and use either of the antennas to receive the signal that is recovered thanks to the high impedance preamplifiers that provide the signal to the Whisper electronic board. The frequency of the sent wave is varied until the whole range of frequencies is covered. A very intense signal is received when this frequency is closed to a characteristic frequency. Depending on the plasma regions different resonances are recovered. In the magnetosphere, the resonances are at the electron cyclotron frequency, Ω_{ce} and its harmonics, at the total plasma frequency, ω_{pe} , the upper-hybrid frequency, $\omega_{UH} = \sqrt{\omega_{pe}^2 + \Omega_{ce}^2}$, and the Bernstein's frequencies. Once the plasma resonance is identified, for example at the plasma frequency, the electron density is then obtained, being proportional to the plasma frequency $n_e(cm^{-3}) \sim \omega_p^2(kHz)/81$. For more details see Ref. Décréau et al. [24], Trotignon et al. [121, 122].

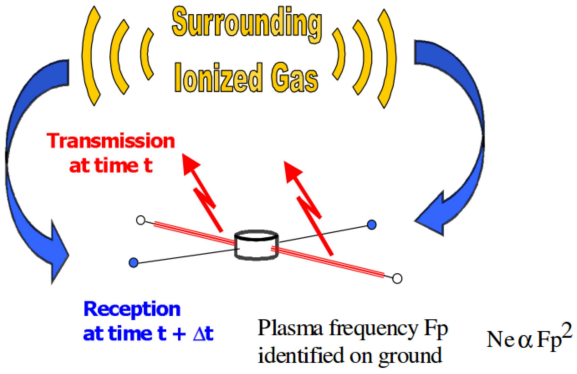

Figure 12: Scheme of WHISPER experiment. Transmitter conductive braids are shown in red. The receiver in this image is connected to the conductive sphere, represented in blue.Image Credit: Trotignon et al. [121]

3.2.1.3 *CIS experiment*

The Cluster Ion Spectrometry (CIS) experiment is onboard of each of the four Cluster spacecrafts but is currently working only for Cluster 4. CIS consists of two instruments:

- CIS-1: A time-of-flight ion Composition Distribution Function (CODIF);
- CIS-2: A Hot Ion Analyser (HIA);

CODIF The CODIF instrument is a high resolution spectrometer that measures the three-dimensional distribution functions of the principal ion species, H^+, He^+, He^{++} and O^+ with one spacecraft spin time resolution (4 s). The energy range covered by this instrument is $[0.02 - 38]$ keV/e. Incoming ions are selected according to their energy per charge ratio by deflection in a toroidal electrostatic analyser with a subsequent time-of-flight (TOF) analysis after a post acceleration of the incoming ions to $E/q \geqslant 15$ keV/e. Ions and secondary electrons emitted from a carbon foil at the entry of the TOF section, during the passage of the ions, are detected by microchannel plate electron multipliers. The detection of these electrons sign the beginning of the TOF process of measurements. Mass per charge ratio is obtained by combining the energy-per-charge selected in the electrostatic analyser with the energy gained during the post acceleration $e\Phi_{acc}$ in the TOF; in formula:

$$\frac{M}{q} = 2\frac{[E/q + e\Phi_{acc}]}{(d/\tau)^2}\alpha$$

Here τ is the time of flight throught the length d of the time-of-flight unit. The parameter α represents the energy loss of the ions in the entry of the TOF section. Density, as all the moments of the distribution function, are measured with 4 s time resolution. In this thesis we used density data obtained from the spacecraft potential measured by EFW, see section 3.2.1.1, to increase time resolution up to 0.2 s.

HIA HIA is an ion energy spectrometer that allows to obtain the three dimensional ion distribution function with one spacecraft spin resolution (4 s). Incoming ions are selected according to their energy per charge ratio, E/q, by electrostatic deflection in a quadrispherical analyser and by changing the voltage between the two hemispheres of the analyser. For more details on these instruments, see Ref.Dandouras and Barthe [23], Reme et al. [94].

3.2.2 *Geotail mission*

The GEOTAIL mission is a collaborative project between the Japanese Institute of Space and Astronautical Science (ISAS) and the American National Aeronautics and Space Administration (NASA). Sent in 1992, after the first period studying the dynamics of the Earth's magnetotail in 1995 its orbit was changed reducing apogee of $30R_E$ to provide data on the solar wind interaction with the magnetosphere. In this thesis we will focus on the density and velocity profiles. The ion moments are measured by the low energy particle instrument (LEP), that is used to observe plasma and energetic particles in the magnetosphere and in the interplanetary medium. It is made up of three sensors: LEP-EA, the energy analyzer measuring 3D velocity distributions and moments of hot plasma in the magnetosphere (for electrons and ions separately and simultaneously), LEP-SW sensor for the Solar Wind and LEP-MS, the energetic ion mass spectrometer. Moments can be used only qualitatively in the LEP SW mode while in the EA-mode data are more reliable. The energy-per-charge analizer (EA) consists of two sets of quadrispherical electrostatic analyzers. Three-dimensional velocity distributions are obtained in a period of four spins while velocity moments are calculated onboard with a spin period resolution (3s). For further details, see the project mission website: *http://pwg.gsfc.nasa.gov/geotail.shtml* and *www.darts.isas.ac.jp/stp/geotail/*.

3.2.3 *ACE*

ACE (Advanced Composition Explorer) is a satellite orbiting in the solar wind that studies particles of various origin over a wide range of energy (from low-energy particles of solar origin to high-energy galactic particles). Launched in 1997 this project is a NASA mission. It orbits at the first Lagrangian point L1, at $1.5 \cdot 10^6$ km from Earth.

It provides useful information on the Solar Wind condition and in particular we will be interested on data giving us the possibility to recover the magnetic field $B_{z,IMF}$ direction before interacting with magnetosphere. The instrument measuring the interplanetary magnetic field direction and magnitude is the magnetometer (MAG). It measures the local interplanetary magnetic field direction and magnitude and it is composed of a twin triaxial fluxgate magnetometer system. Mission website *http://www.srl.caltech.edu/ACE/*.

3.3 SPACECRAFT DATA ANALYSIS METHODS

In this part we will briefly introduce the methods of data analysis that are used in this thesis, to determine for example the normal to the magnetopause, see section 3.3.1 and 3.3.2, the magnetopause velocity, see section 3.3.3 and the local magnetopause reference frame, see section 3.3.4.

3.3.1 *Minimum Variance Analysis*

The minimum variance analysis consist in determining the direction $\hat{n}$ of a magnetic discontinuity. In the hypothesis of one dimensional discontinuity and neglecting temporal variations of it during the crossing of the satellites we can write that $\nabla \cdot B = \hat{n} \cdot \nabla(B \cdot \hat{n}) = 0$ so that it exist a direction $\hat{n}$ for which $B \cdot \hat{n}$ is constant (section "Minimum and Maximum Variance Analysis" in Paschmann and Daly [89]). Considering the magnetopause as a moving planar structure, the normal direction can be estimated identifying the direction in space where the magnetic field has the smallest fluctuations, i. e. where $\left\langle |(B - \langle B \rangle) \cdot \hat{n}|^2 \right\rangle$ has a minimum, here $\langle B \rangle$ is the mean magnetic field. Defining the magnetic field time series as $B^{(m)}$ ($m = 0, ..., M$), the direction $\hat{n}$ is obtained from the direction where the set $\left\{B^{(m)} \cdot \hat{n}\right\}$as minimum variance. The variance matrix to minimize to obtain $\hat{n}$ is defined as:

$$\sigma^2 = \frac{1}{M} \sum_{m=1}^{M} \left[\left(\left\langle \mathbf{B}^{(m)} \right\rangle - \langle \mathbf{B} \rangle \right) \cdot \hat{n} \right]^2$$

The average magnetic field $\langle \mathbf{B} \rangle$ is defined as: $\langle \mathbf{B} \rangle = \frac{1}{M} \sum_{m=1}^{M} \mathbf{B}^{(m)}$. The constraint $|\hat{n}^2| = 1$ has also to be imposed when minimizing. Using a *Lagrange multiplier*, for each component $j = x, y, z$ we get:

$$\frac{\partial}{\partial n_j} \left[\sigma^2 - \left(\hat{n}^2 - 1 \right) \right] = 0$$

These three equations can be written in a matrix form, as follows:

$$\sum_j \left(< B_i B_j > - < B_i >< B_j > \right) n_j = \lambda n_i$$

The eigenvalues λ_1, λ_2, λ_3 (numbered from the largest to the smallest) represent the variances of each component and they correspond to the orthogonal eigenvectors x_1, x_2, x_3. The normalized eigenvector, x_3, that corresponds to the normalized eigenvector associated with the smallest eigenvalue λ_3 of the variance matrix corresponds to the normal direction, $\hat{n}$. The magnetic field is then decomposed in its maximum, intermediate and minimum variance components:

$$B_{MVA} = B_{max}x_1 + B_{int}x_2 + B_{min}x_3$$

This method works if the eigenvalues can be clearly be distinguished, i. e. λ_1/λ_3 and λ_2/λ_3 are higher than 10. For more details on this analysis technique see chapter 8 in Paschmann and Daly [89].

3.3.2 *Timing method*

The timing method is a method used to estimate the velocity along and normal to the magnetopause, see Ref. Vogt et al. [126], Paschmann and Daly [89]. Supposing a discontinuity moving with velocity $\mathbf{V}$ along its normal, $\hat{\mathbf{n}}$. Neglecting temporal variation of it during the satellite crossing, if the discontinuity is detected by all the four spacecrafts, at time $t = t_\alpha$, let $\mathbf{r}_\alpha$ be the position of the spacecraft, then during the time $dt_{\alpha,\beta} = t_\alpha - t_\beta$ the discontinuity has moved with velocity V along $\hat{\mathbf{n}}$, covering a distance $\mathbf{r}_{\alpha,\beta} = (\mathbf{r}_\alpha - \mathbf{r}_\beta)$. Using satellite 4 as reference, we can then write:

$$(\mathbf{r}_\alpha - \mathbf{r}_4) \cdot \hat{n} = \mathbf{V}(t_\alpha - t_4) \tag{24}$$

Following Paschmann and Daly [89], we can introduce the vector $\mathbf{m} = \hat{\mathbf{n}}/\mathbf{V}$ and re-write equation 24 as:

$$D\mathbf{m} = T$$

where $D = (\mathbf{r}_1 - \mathbf{r}_4, \mathbf{r}_2 - \mathbf{r}_4, \mathbf{r}_3 - \mathbf{r}_4)$ and $T = \begin{pmatrix} t_1 - t_4 \\ t_2 - t_4 \\ t_3 - t_4 \end{pmatrix}$, and $\mathbf{m}$ can be found calculating $\mathbf{m} = D^{-1}T$.

3.3.3 *DeHoffman Teller*

The DeHoffman-Teller (HT) frame is a frame moving at velocity $\mathbf{u}_{HT}$ such that if $\mathbf{E}$ is the electric field measured by satellites, in the HT frame the electric field is given by $\mathbf{E}' = \mathbf{E} - \mathbf{u}_{HT} \wedge \mathbf{B} = 0$. From the Faraday's law we deduce that in this frame the magnetic field is stationary. We consider a set of experimental measurements of the plasma velocity $u^{(i)}$ and of the magnetic field $\mathbf{B}^{(i)}$, with $i = 0, ..., N$. To determine the HT frame we look for a frame in which the mean

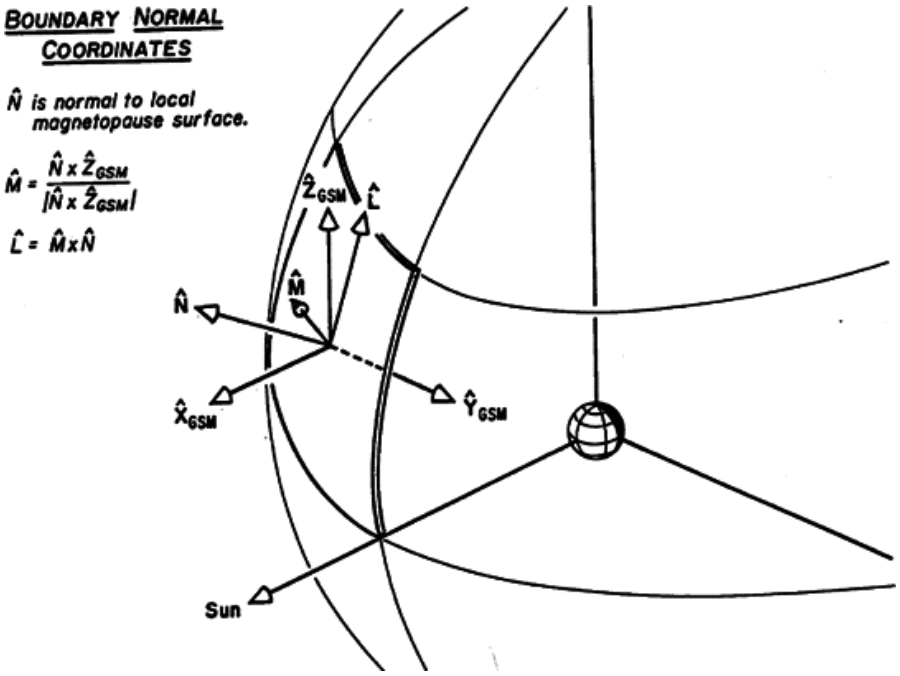

Figure 13: Boundary normal coordinates system at the magnetopause in comparison with the GSM coordinate system. $\hat{N}$ is the direction normal to the magnetopause

square of the electric field, in the given data, is the smallest possible, see Chapter 9 in Ref. Paschmann and Daly [89]. We define the quantity:

$$D(\mathbf{V}) = \frac{1}{N}\sum_{i=1}^{N}\left|E'^{(i)}\right|^2 = \frac{1}{N}\sum_{i=1}^{N}\left|(u^{(i)} - V)\right|^2 \wedge \mathbf{B}^{(i)}$$

where the value of V that minimize $D(\mathbf{V})$ corresponds to the HT velocity. This value is obtained imposing that $\nabla_{\mathbf{V}} D = 0$ and we call V_{HT} this velocity. The component of the DeHoffman-Teller velocity along the normal to the magnetopause $\mathbf{u}_{HT} \cdot \hat{n}$, gives the velocity of the magnetopause (supposing the magnetopause moving along the normal $\hat{n}$).

3.3.4 *The boundary normal coordinate system (LMN)*

A common coordinate system used for the satellite data investigation is the local coordinate system, using a set of coordinates ($\hat{L}$, $\hat{M}$, $\hat{N}$). In figure 13 we show this coordinate system in comparison with the Geocentric Solar Magnetospheric (GSM) one. The $\hat{L}$ and $\hat{M}$ directions lie in a plane tangential to the boundary while $\hat{N}$ is perpendicular to it. In the case of the magnetopause, the normal is usually defined as positive away from the Earth, see figure 13. To determine the normal to the magnetopause, $\hat{N}$, one can use a model of the magnetopause

or the minimum variance analysis, see section 3.3.1. The $\hat{L}$ direction is determined projecting the solar magnetospheric $\hat{Z}$ direction into the plane perpendicular to $\hat{N}$ and the $\hat{M}$ direction is built in order to have a right handed cartesian coordinate system, see Ref. Hapgood [48].

Part II

TURBULENCE IN KELVIN-HELMHOLTZ VORTICES

4

TWO FLUID NUMERICAL SIMULATION OF TURBULENCE IN K-H VORTICES

During the evolution of the Kelvin-Helmholtz instability, the vortices that are formed in the non-linear phase, can interact with each other merging and pairing or they can be disrupted due to the development of secondary instabilities around the vortex arms, like secondary K-H, Rayleigh-Taylor (R-T) and magnetic reconnection (MR), Ref. Matsumoto and Hoshino [73]. The final stage of the instability is a turbulent complex pattern characterized by small current sheet structures. In this work a two dimensional two-fluid code is used to investigate the turbulence that spontaneously develops inside the K-H vortices.

Turbulence is very common phenomenon in nature, it characterizes many different environments from fluids, Ref. Lesieur [69], Thorpe [119], to astrophysical plasmas, like the solar wind, Ref. Bruno and Carbone [11], planets magnetospheres, like Earth, Ref. Borovsky and Funsten [9], Rezeau and Belmont [96] or Jupiter, Ref. Saur et al. [102], accretion disks, Ref. Balbus and Hawley [3], and laboratory as well, like in fusion plasma experiment, Ref. Hasegawa and Wakatani [49], Horton [59], Tynan et al. [123]. In this thesis we focus on turbulence spontaneously developing inside Kelvin-Helmholtz vortices. This instability, indeed is one of the main driver of the turbulence observed in the magnetosheath or in the polar cusps, Ref. Zimbardo et al. [133]. In this thesis, the environment of interest is the low latitude magnetopause, where K-H role is of fundamental importance, during northward interplanetary magnetic field condition, for solar wind transport, Ref. Dungey [26], Miura [75], Nykyri and Otto [83], Hasegawa et al. [50], Faganello et al. [30], Hasegawa [54], Farrugia et al. [36].

K-H instability can be divided in three principal phases, one is called 'linear phase', it corresponds to the phase where the perturbations are small enough to make a linearization possible, small with respect to the average quantity (small velocity perturbation with respect to the velocity of the flow for instance), i.e. when the instability has started but without the formation of the characteristic vortices, the second one is 'the non-linear phase' when vortices are formed and they start to interact by merging or by secondary instabilities and finally the 'saturated phase' when vortices are destroyed. In fig-

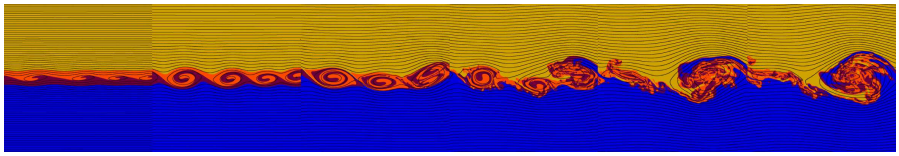

Figure 14: Time evolution of the passive tracer (a scalar quantity advected by the flow) of a Kelvin-Helmholtz Two-Fluid simulation (see Appendix B for numerical details) initialized with a velocity shear. The solar wind is represented in yellow and the magnetosphere in blue.

ure 14 we show the time evolution of the K-H instability from the linear (on the left) to the turbulent saturated phase (on the right).

The vortices disruption is led by the evolution of secondary instabilities around the edge of the primary KH vortices or inside the vortex itself. The final stage is characterized by a mixing layer where solar wind and magnetosphere interact. Observations have confirmed the presence of a broad boundary layer during northward interplanetary magnetic field, Ref. Phan et al. [92], Wing and Newell [131]. Most of the numerical simulations on this topic are MHD, Ref. Miura and Pritchett [78], Miura [77], Frank et al. [41], Matsumoto and Seki [74], Otto and Fairfield [86], Matsumoto and Hoshino [72], Fairfield et al. [35], Salvesen et al. [101]. MHD simulations have been used to investigate the role played by secondary instabilities in the development of turbulence, Ref. Matsumoto and Hoshino [72] and in particular the importance of a density shear for the onset of the turbulence. A comparison between MHD and PIC simulations can be found in Ref. Matsumoto and Hoshino [72], Matsumoto and Seki [74], where differences between these two kind of simulations occur in the formation of the mixing layer and in the analysis of the dissipation scales. Hybrid simulations (kinetic ions, fluid electrons), Ref. Cowee et al. [20], stressed the importance of a density gradient in forming turbulence, because of the formation of secondary instabilities and the K-H diffusive plasma transport. Recent PIC simulations, Ref. Karimabadi et al. [62], Wan et al. [130], Leonardis et al. [68] have analyzed in 2D and 3D the turbulence induced by Kelvin-Helmholtz instability from ion to electron scales and in particular the small scale structures formed inside the large final turbulent vortex, where small scale current sheets formed and these small areas contribute mostly to the total dissipation.

In this work we have used a 2D version of the two fluid code, described in the appendix B. The importance of this code is to have access both to the large scale dynamics down to the ion scales structures, that are formed during the turbulent cascade. The turbulence induced by a large scale velocity shear reproduces possibly what is occurring in the mixing layer at the interface between solar wind and the magnetosphere, Ref. Zimbardo et al. [133]. The mixing layer is

often in a turbulent state and it has been investigated in the recent and past literature using various numerical simulations. Many open questions are still to be clarified, e.g. understand the exact mechanisms occurring at small scales and responsible for the solar wind plasma transport or the contribution to diffusion through small scale magnetic reconnection events occurring inside the turbulent pattern.

In this chapter we first discuss the initial conditions used in our simulations, section 4.1; then in the second part we present the turbulence analysis performed on the results of our simulations, section 4.2.

4.1 INITIAL PLASMA CONFIGURATION

The 2D version of the two fluid simulation is initialized by a velocity shear perpendicular to the flow direction. In the code the y-axis is the solar wind direction and the x-axis is the inhomogeneous direction. The velocity shear has the form of an hyperbolic tangent profile centred in the middle of the simulation box:

$$\mathbf{U} = \frac{\Delta U_0}{2} tanh\left(\frac{x - x_c}{L_{eq}}\right)\hat{e}_y \tag{25}$$

where $x_c = L_x/2$ with L_x the x-dimension of the simulation box, ΔU_0 is the total velocity jump and L_{eq} the velocity shear length. The total velocity jump, ΔU_0, between solar wind and the almost static magnetosphere is represented in the code by a variation of the velocity from $-\Delta U_0/2$ in the magnetosphere to $\Delta U_0/2$ in the SW, obtained by doing a Galilean transformation of the velocity field. In figure 15 we plot the iso-contours of the velocity field, $U_{iy}(x, y)$. The velocity shear, shown in eq. 25, is represented with a superposed white continuous line. In this figure the positive and negative value of the velocity profile are represented respectively with upward and downward arrows. The magnetosphere is represented in blue in the left half-side of the simulation box and the solar wind, on the right, is represented in orange.

The velocity shear length used in this simulation is $L_{eq} = 6\ d_i$ and the total velocity jump is $\Delta U_0 = 2v_A$ where v_A is the Alfvèn velocity in the magnetosheath side, see section 2.2 for the normalization used in the code. The initial magnetic field is directed mostly in the z-direction with a small in plane component initially directed along the flow.

$$\mathbf{B}(x) = B_0(x)sin\vartheta\hat{e}_y + B_0(x)cos\vartheta\hat{e}_z \tag{26}$$

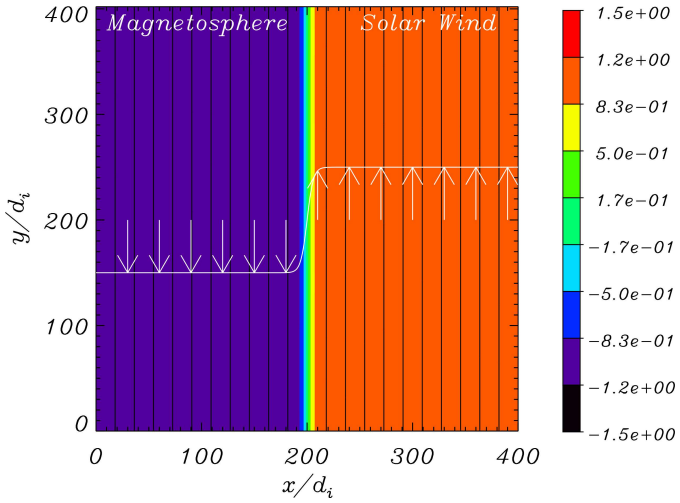

Figure 15: Iso-contours of the velocity $U_{iy}(x, y)$, in this configuration the magnetosphere is on the left side of the simulation box and it is represented in blue while the solar wind/magnetosheath plasma is shown on the right in orange. The velocity shear, amplified for clarity reason, is shown with a white continuous line. The arrows represent the shear velocity value, when downwards the velocity is negative, $-\Delta U_0/2$, and when upwards the velocity is positive, $+\Delta U_0/2$.

where $\vartheta = 0.02$. Density and temperature are initially constants. All the quantities are normalized to their value in the magnetosheath, corresponding to the right side of the simulation:

$$\begin{cases} n(x) = n(x_+) = 1.0 \\ B(x) = B(x_+) = 1.0 \\ T_{e,i}(x) = T_{e,i}(x_+) = 0.5 \end{cases} \tag{27}$$

The size of the simulation box is $L_x \times L_y = [400 \times 402]\ d_i$, the total number of points is $N_x \times N_y = 4096 \times 8192$ and consequently the spatial resolution is $dx \times dy = L_x/N_x \times L_y/N_y = 0.1\ d_i \times 0.05\ d_i$. The same simulation without an in-plane component field has been run as well and in the future we will analyse and compare how turbulence develops with and without a magnetic field along the flow. In the following section we limit ourself to the case where the in plane magnetic is included.

4.2 TURBULENCE ANALYSIS

After the development of the K-H instability, vortices are dominated by the pairing mechanism and by the development of secondary instabilities. These latter mechanisms are responsible for the vortices disruption and the consequent formation of small scales structures of scale length of the order of the ion inertial length or less. In fig-

ure 16 top panel we plot, in the saturated phase of the instability, the iso-contour of the out-of-plane component of the current, J_z, with overplotted the magnetic potential field lines. In this figure there are two boxes. The first one with red margins is selected inside the most turbulent area and has dimensions $dx_{box-in} \times dy_{box-in} = [180 - 240]\ d_i \times [70 - 130]\ d_i$; the second one, with blue margins is selected outside the K-H dynamics in the range $dx_{box-out} \times dy_{box-out} = [50 - 100]\ d_i \times [250 - 300]\ d_i$. In the bottom panel we plot a zoom of the same quantity for the red box. We note the presence of structures of dimensions around the ion inertial scale characterized by a strong current. Inside each of the boxes defined above, we calculate separately the magnetic field fluctuations around the average field, defined as:

$$\delta B_i(x, y) = B_i(x, y) - \langle B_i(x, y) \rangle \tag{28}$$

with $i = x,\ y,\ z$, so that the magnetic energy of the fluctuations is:

$$\delta B^2(x, y) = \delta B_x^2(x, y) + \delta B_y^2(x, y) + \delta B_z^2(x, y)$$

In order to obtain the two dimensional distribution of the spectral magnetic energy, $\delta B^2(k_x, k_y)$ we need to have periodicity in both directions of the boxes so as to be able to apply the 2D Fast Fourier Transform. For this purpose an Hann window is applied in both directions. We will discuss this window in the next section.

4.2.1 *Hann window*

The Hann window has been applied in both directions of the selected boxes. The window function has the form of half of a cosine wave, see eq. 29. Generally, there are two main reasons why it is preferable to other windows, i.e. the detection of the signal in presence of a broadband noise and the resolution (the ability to distinguish narrowband spectral components). The Hann window is defined as:

$$w(n) = 0.5 \left(1 - \cos\left(\frac{2\pi n}{N - 1}\right)\right), \quad 0 \leqslant n \leqslant N - 1 \tag{29}$$

where N is the number of points on which the window is defined. In figure 17 we show a series of windows in the time domain to compare Hann window (represented in dark green) to other kind of windows. Typically the narrower the main lobe the higher the frequency resolution since it increases its ability to distinguish two closely spaced frequency components. Looking at figure 17, Hann window shows narrower main lobe with respect to a Gaussian window. An important aspect to consider is that if the main lobe decreases the remaining energy goes to the side lobes decreasing the amplitude accuracy, that means decreasing the detection capability. An equilibrium between

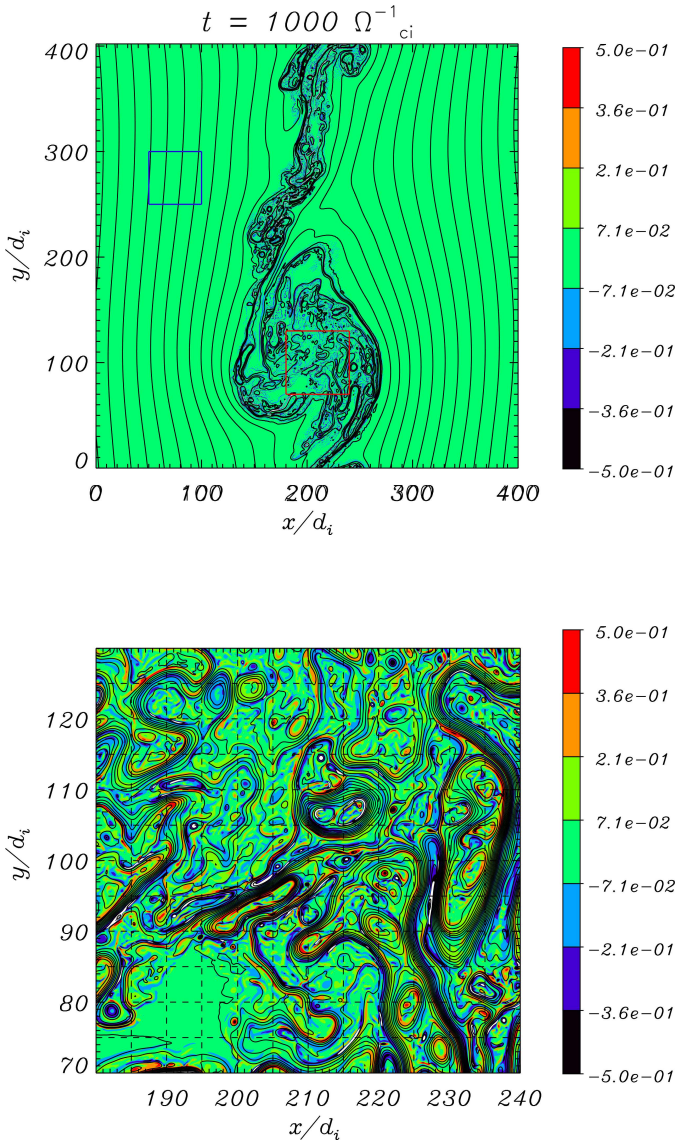

Figure 16: Two dimensional iso-contours of $J_z(x, y)$ at the saturated turbulent stage of K-H instability, $t = 1000\ \Omega_{ci}^{-1}$ is shown in the top panel. Magnetic potential is shown with black overplotted lines in all the panels. There are two colored boxes, the one with red margins, of dimensions $dx_{box-in} \times dy_{box-in} = [180 - 240]\ d_i \times [70 - 130]\ d_i$, is selected inside the area of the large final K-H vortex (BI). The blue box of size $dx_{box-out} \times dy_{box-out} = [50 - 100]\ d_i \times [250 - 300]\ d_i$ instead has been chosen outside the K-H dynamics. A zoom of the box inside the turbulent region is shown in the bottom panel.

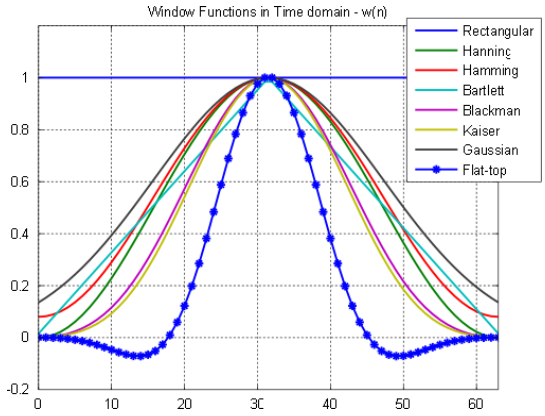

Figure 17: Time response of various typologies of windows. Hann window is plotted in dark green.

accuracy and spectral resolution is needed. Side lobes should fall-off rapidly in a good window, since they directly affect how much adjacent frequency components can drop into adjacent frequency bins, Hann window is preferable also in this case compared to a Gaussian window.

4.2.2 *Anisotropy*

Once established periodicity, thanks to Hann window, the total 2D spectral density of magnetic energy has been calculated in the red box inside the vortex region, shown in figure 16. In figure 18 the bidimensional spectral energy $\delta B^2(k_x, k_y)$ is shown in the (k_x, k_y) space, from top left to right for time $t = 600\ \Omega_{ci}^{-1}$,$t = 750\ \Omega_{ci}^{-1}$,$t = 850\ \Omega_{ci}^{-1}$ and $t = 1000\ \Omega_{ci}^{-1}$. Observing the top panel on the left, we see that initially energy is not distributed isotropically in the (k_x, k_y) space; however, during the non-linear evolution of the instability the system turns into an almost isotropic state, see panel on the bottom right corresponding to time $t = 1000\ \Omega_{ci}^{-1}$. Indeed, the system is initially strongly not isotropic since a velocity shear is imposed in the x-direction and the vortex structures are also not circle shaped.

A quantitative measure of the level of isotropy of a system is the Shebalin angle, Ref. Shebalin et al. [106], Valentini et al. [124]. It is a measure of the ratio between the energy in the perpendicular direction and in the parallel direction, with respect to the magnetic field and it is defined as:

$$\tan^2(\vartheta) = \frac{\sum_k k_x^2 |\delta \mathbf{B}(k,t)|^2}{\sum_k k_y^2 |\delta \mathbf{B}(k,t)|^2} \tag{30}$$

The distribution of the energy in the $(k_x,\ k_y)$ plane is isotropic when $\vartheta = 45°$, so $\tan^2(\vartheta) = 1$. In figure 19 we show the evolution in time of the $\tan^2(\vartheta)$. At the beginning, during the linear phase of the primary K-H, $\tan^2(\vartheta)$ value is of the order of 4 that correspond to $\vartheta = 63°$.

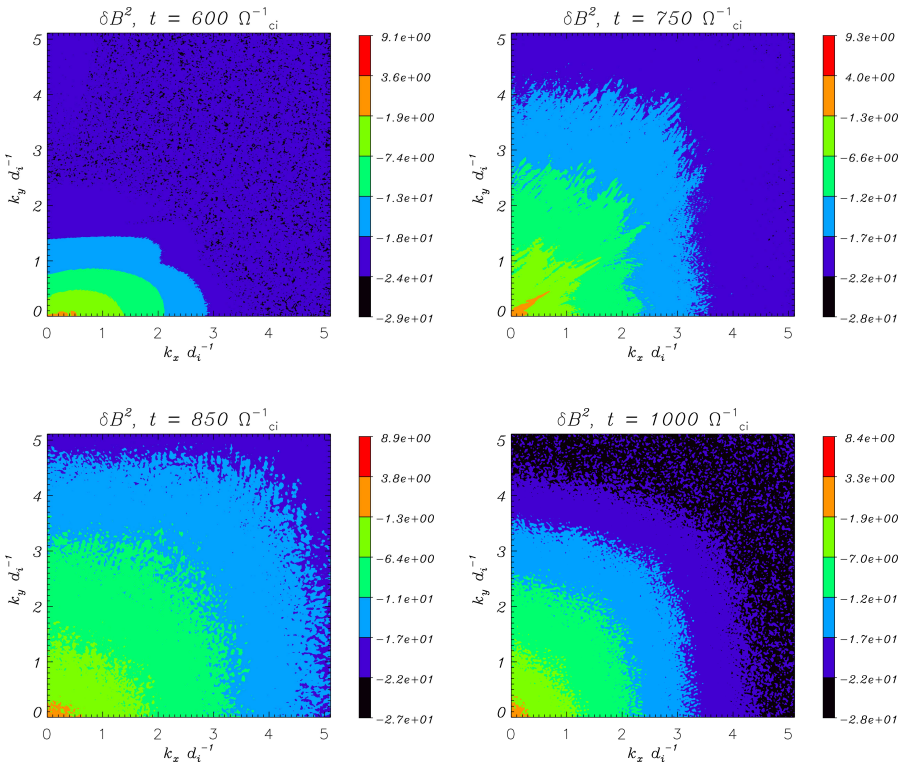

Figure 18: Two dimensional density of magnetic spectral energy at four different times of the simulation, from top left to bottom right, for t = 600 Ω_{ci}^{-1},t = 750 Ω_{ci}^{-1},t = 850 Ω_{ci}^{-1} and t = 1000 Ω_{ci}^{-1}. A growing isotropy of the system can be observed.

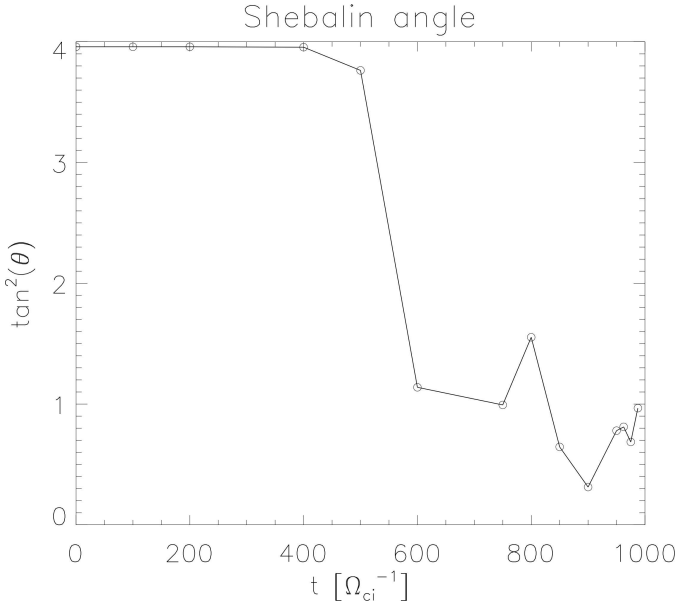

Figure 19: Evolution in time of the $tan^2(\vartheta)$, when this quantity is equal to 1 it means that the system is isotropic. It can be observed a tendency to an isotropy configuration during the time evolution of the instability.

However as soon as the vortices non-linear dynamics take place, the secondary instabilities develop and destroy the asymmetry of the system consequently the Shebalin angle value decreases until it reaches the isotropic value of the order of one at the end of the simulation, $t = 1000\ \Omega_{ci}^{-1}$. Once the isotropic spectral configuration has been achieved, we calculate the magnetic energy spectrum.

Two dimensional spectral energy of magnetic field fluctuations has been integrated over concentric shells from $k = 2\pi/L_x = 0.1\ d_i^{-1}$ to $k = 2\pi/2dx = 32\ d_i^{-1}$. In figure 20, the 2D integrated spectra is shown as a function of $k_\perp$. The dashed vertical line at $k_\perp = 1/l_{inj} = 0.04\ d_i^{-1}$ corresponds to the most unstable wave vector of the primary K-H instability and the corresponding wavelength gives the initial vortex size. The dashed vertical line at $k_\perp = 1\ d_i^{-1}$, marks the wavevector corresponding to the ion inertial scale. The light blue part of the spectrum involves scales at which the filters start to act, corresponding to the region where the spectrum decays exponentially. A spectral filter is used along the periodic y and a sixth order spectral like filtering scheme along the inhomogeneous x-direction, Ref. Lele [67], Faganello et al. [31] and see appendix B for more details. Simulations with different numerical grids have been tested to verify that the effect of the filters do not alter the shape of the spectrum at ion scales; the numerical model does not allow to solve the electron scale so we limit to study the ion region.

A power-law of $k_\perp^{\sim=8/3}$ is recovered between $k_\perp = 0.2\ d_i^{-1}$ and $k_\perp = 2\ d_i^{-1}$, represented with a green line in figure 20.

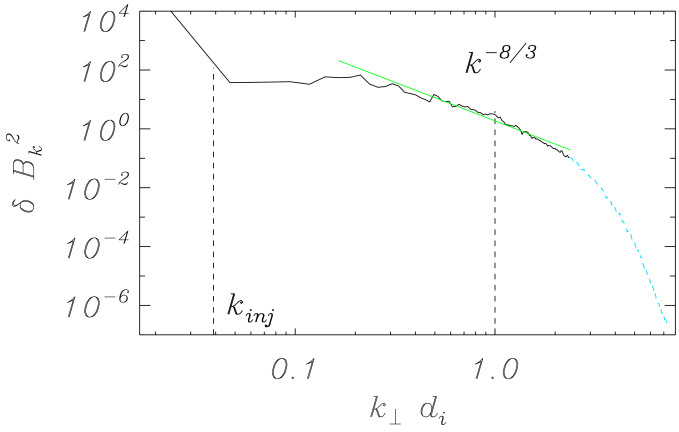

Figure 20: Bidimensional integrated spectrum over concentric shells at t = 1000 Ω_{ci}^{-1}. From left dashed lines represents injection and ion scales respectively. Green line is a linear fit performed between k = 0.2 and k = 2. Part of the spectrum marked in light blue shows the scales where filters begin to act.

This slope has been found as well in 2D PIC simulations, Ref. Karimabadi et al. [62], Wan et al. [130], Camporeale and Burgess [13], Haynes et al. [55]. It is worth to note that the simulation box, chosen in order to study the dynamics at ion scales, is not large enough, in terms of the wave-vector k, to lead the system develop the inertial range that indeed we do not observe. Incidentally, a similar slope has been found in plasma environments like the magnetosheath, where (using the Taylor hyphothesis to replace the temporal with the spatial scales) studies of in-situ measurements showed above the ion scales, a scaling of $\delta B^2_{\perp,\parallel} \sim k^{-2.5}$, recovered for both the perpendicular and the parallel fluctuations, see Ref. Alexandrova et al. [2] and at the flanks of the magnetopause, see Ref. Zimbardo et al. [133]. A k-filtering technique applied to Cluster magnetosheath data has provided a $k^{-2.6}$, see Ref. Sahraoui et al. [100], for the magnetic energy as a function of the wave vector component in the flow direction. In general in the magnetosheath a break around Ω_{ci} in the spectrum slope, similar to the one observed in the solar wind, is recovered. Indeed satellites observations have revealed a Kolmogorov spectrum $\delta B^2_\perp \sim k^{-5/3}$ for the magnetic field fluctuations at MHD scales followed by a spectral slope at ion scales given by $\delta B^2_\perp \sim k^{-\alpha}$ with $\alpha \sim [2.3 - 3]$, see Ref. Zimbardo et al. [133], Camporeale and Burgess [13] and references therein. The scaling at frequencies higher than ion frequencies is attributed to non-linear processes linked to the Hall effect, see Ref. Yordanova et al. [132]. The Kolmogorov spectrum is not always observed in the magnetosheath, see Ref. Alexandrova [1], Czaykowska et al. [22], but it develops when the non-linear time of the interactions is smaller then the transit time, Ref. Alexandrova [1]. In a similar way in PIC simulation, Ref. Karimabadi et al. [62], at longer times a fluid dynamics and a Kolmogorov spectrum is observed. In our numeri-

cal simulation the range of wavelengths is not sufficiently large to observe a Kolmogorov spectrum.

4.2.2.1 *Increments and PDFs*

Beyond the spectrum, turbulence can be studied by looking at the probability distribution functions (PDFs) of the magnetic field increments. Increments are calculated for the B_x and the B_y components of the magnetic field in both the directions of the simulation box and they are defined as:

$$\begin{cases} dB_i(\ell_x) = \delta B_i(x+\ell, y) - \delta B_i(x, y) \\ dB_i(\ell_y) = \delta B_i(x, y+\ell) - \delta B_i(x, y) \end{cases} \tag{31}$$

Here ℓ defines the scale at which increments are calculated and $i = x,\ y$ the component of the magnetic field. The range of scales considered is $[1.5 \leqslant \ell \leqslant 19]\ d_i$. Probability distribution functions (PDFs) of these four quantities have been calculated inside and outside the turbulent region, respectively in the box with red and in the box with blue margins, shown in figure 16. Since the PDFs look similar for the increments in the two directions (as expected from the analysis on the isotropy performed on the previous section) we decide to unify the increments calculated in the two directions to increase the statistic, so we define:

$$dB_i(\ell) = dB_i(\ell_x) \cup dB_i(\ell_y)$$

In figure 21 we show in the top panels the PDFs calculated for all the increments, $dB_x(\ell)$, of the x-component of the magnetic field. Top left panel refers to the increments calculated in the box inside the turbulent area while top right panel to increments calculated in the box outside it. The blue dashed line represents a Gaussian distribution with $\sigma = 1$, used as a reference distribution. In the bottom panels of the same figure we plot the flatness, i.e. the fourth order moment of the increments, again left panel refers to red margin box (inside the turbulent area) and right panel to the box selected outside the turbulent area. In this panel the black dashed line represents the value of the flatness for a Gaussian distribution. Looking at the PDFs we observe the presence of tails with respect to a Gaussian distribution for the increments calculated inside the box in the turbulent region while PDFs follow almost a Gaussian shape when calculated in the box outside the turbulent region. Tails with respect to a Gaussian distribution are due to particularly intense magnetic field fluctuations, usually related to the presence of coherent structures. PDFs look non symmetrical with respect to zero, this is a universal feature typically observed in turbulence, Ref. Frisch [42]. 'Extended' tailed PDFs of the

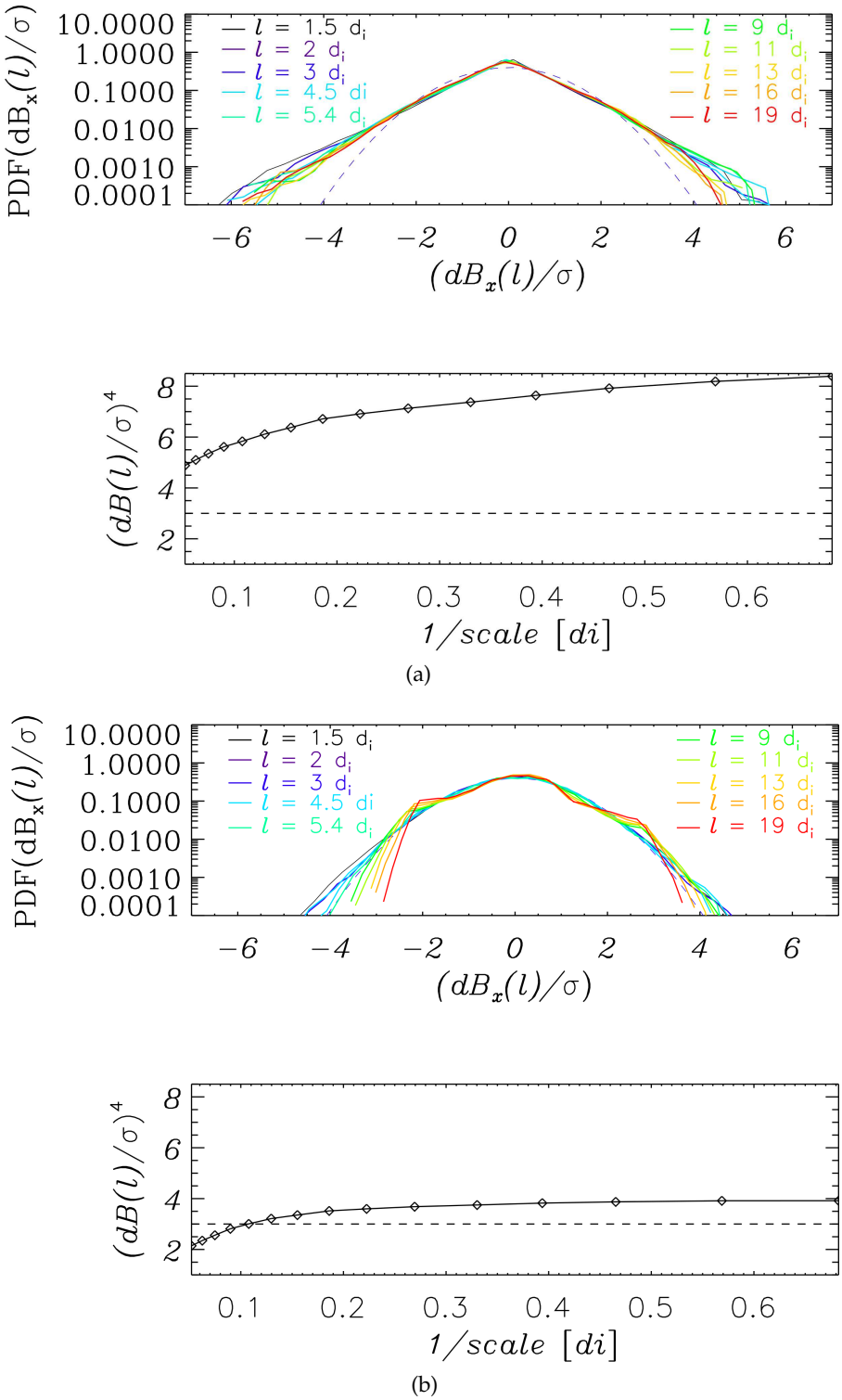

Figure 21: Probability distribution functions (PDFs) calculated at different scales, from $\ell = 1.5$ d_i to $\ell = 19$ d_i are shown in the top panels of figures (a) and (b). In the bottom panels of figures (a) and (b) flatness is plotted versus the inverse of the scale. Panel (a) refers to the box inside the turbulent region and panel (b) to the box selected outside it. In all the panels B_x increments are considered.

increments of the magnetic field have been as well found in PIC simulations of turbulence induced by a shear velocity, Ref. Karimabadi et al. [62]. Tails in the PDFs at different scales are a signature of intermittency. A way to quantify it, is the flatness, defined as the fourth order moment of the increments:

$$\mathcal{F}(\ell) = \frac{\left\langle dB_i(\ell)^4 \right\rangle}{\left\langle dB_i(\ell)^2 \right\rangle^2} \tag{32}$$

Flatness is increasing for the increments calculated inside the K-H turbulent region, see left bottom panel of figure 21, going from $\mathcal{F}(\ell) \sim 5$ for large scales (around $\ell \sim 19\ d_i$) to $\mathcal{F}(\ell) \sim 9$ for scales around $\ell \sim 1.5\ d_i$; instead it stays almost constant outside the vortices, see bottom right panel of figure 21. Tails quantified in this way are related to strong discontinuities.

4.2.3 *Current sheets and magnetic reconnection regions.*

Intermittency reveals the presence of relatively intense magnetic field fluctuations. To indentify and to characterize these structures we use the normalized Partial Variance of the Increments, Ref. Greco et al. [46], Servidio et al. [105], Chasapis et al. [17]. It is defined as the ratio of the absolute value of magnetic field increments, at a certain scale, over the variance:

$$\mathcal{PVI}(\ell) = \sqrt{\frac{|d\mathbf{B}(\ell)|^2}{\langle |d\mathbf{B}(\ell)|^2 \rangle}} \tag{33}$$

where $d\mathbf{B}(\ell)$ are the total magnetic field increments at each scale ℓ. PVI has been calculated on all the vertical and horizontal cuts shown in the bottom panel in figure 16 with black dashed lines. For each of these cuts, separated by 5 d_i, we calculate PVI for different scales: $\ell = 0.5\ d_i,\ 1\ d_i,\ 2\ d_i,\ 5\ d_i$. On the purpose of selecting structures with the most intense magnetic fluctuations, we analyse also the quantity $|J_z|/\sigma$ since strong magnetic field variations correspond to intense current regions. Then we count the total number of structures with a value of $|J_z|/\sigma$ and PVI higher than a threshold that is left to vary from 1σ to 3σ. In figure 22 we show the histograms of the total number of structures with intensity higher than 1σ, 2σ and 3σ represented with blue, red and yellow histograms respectively.

The most intense structures with PVI $> 3\sigma$ (corresponding to yellow histograms) appear to be mostly at scales around $\ell = 0.5,\ 1\ d_i$, i.e. of the order of the ion inertial length or less. It is important to underline here that PVI structures are usually associated to reconnecting current sheets, Ref. Servidio et al. [105], and and are important

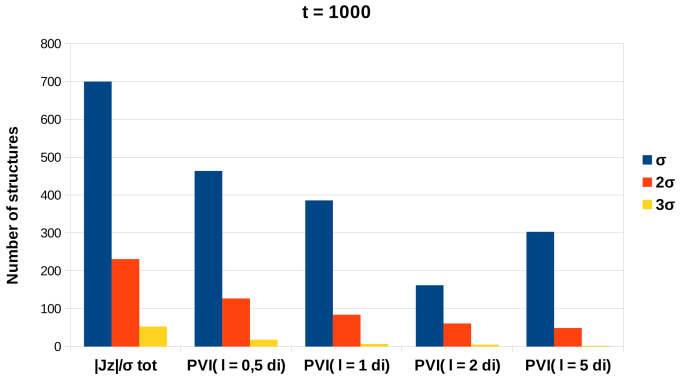

Figure 22: The total number of structures with $|J_z|/\sigma$ and PVI value higher than σ is represented with blue histograms, higher than 2 σ with red histograms and higher than 3σ with yellow histograms. Four different scales are considered for PVI $\ell = 0.5\ d_i,\ 1\ d_i,\ 2\ d_i,\ 5\ d_i$.

sites of energy dissipation, see for example Retinò et al. [95], Sundkvist et al. [113], Chasapis et al. [17]. Selecting structures as described above we analyse each of them to verify if they correspond to reconnection structures. As an example, in figure 23 we plot the PVI for a cut at $y = 90\ d_i$ for all the different scales considered. In particular, top left panel shows PVI calculated at the scale $\ell = 0.5\ d_i$, top right panel PVI for the scale $\ell = 1\ d_i$, bottom left panel corresponds to the PVI at the scale $\ell = 2\ d_i$ and bottom right PVI for the scale $\ell = 5\ d_i$. Horizontal lines correspond to the thresholds 1σ, 2σ and 3σ, plotted respectively with blue, red and yellow continuous lines.

High PVI structures are usually associated to reconnecting current sheets and are important sites of energy dissipation Sundkvist et al. [113], Retinò et al. [95], Chasapis et al. [17]. Using PIC codes it has been proved that large part of dissipation is occurring in relatively small areas characterized by high electric current density, Ref. Wan et al. [130]. Dissipation is localized inside the small coherent structures and the dissipated energy mostly goes into particle heating, Ref. Karimabadi et al. [62]. Our code is adiabatic so we can not measure the dissipation due to the small coherent structures, but we can still analyse these structures characterised by a strong current, PVI $> 2\sigma$. As an example we report the study on one of this structures. For the cut at $y = 90\ d_i$ we select a range where PVI is particularly high, in the x-range $[226.5 - 228]\ d_i$, see figure 23. By looking at the out-of-plane current in this interval, we select a range $[88 - 95]\ d_i$ in the y-direction around the cut ($y = 90\ d_i$) and we individuate the structure shown in figure 24. In this figure the iso-contours of the current are shown together with magnetic potential lines in the selected range. The vertical and horizontal red dashed lines mark the position of the X-point, that has coordinates $(x_{X-point},\ y_{X-point}) = (227.1,\ 91.5)\ d_i$. To analyse this structure we made two cuts on each side of the X-point along the y-direction,

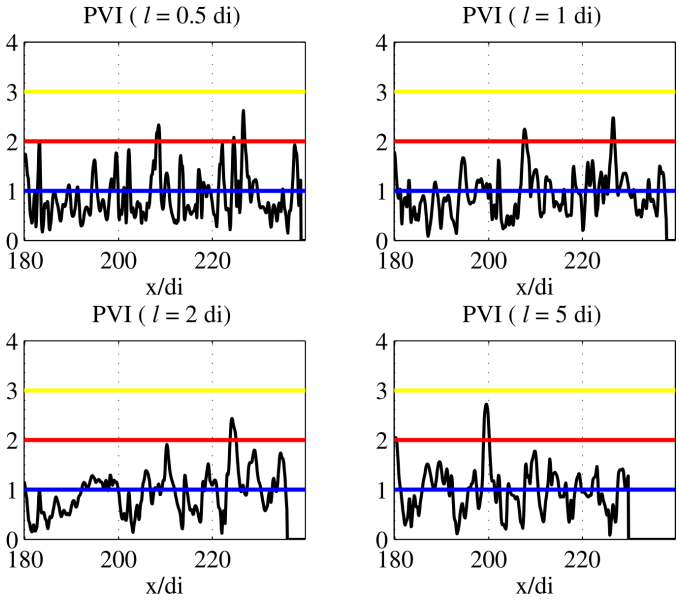

Figure 23: PVI calculated for the cut $y = 90$ $d_i$at different scales. From top left to bottom right panel for scales $\ell = 0.5$ d_i, $\ell = 1$ d_i, $\ell = 2$ d_i and $\ell = 5$ d_i.

respectively at $y_{cut\,I} = 91$ d_i and at $y_{cut\,II} = 92$ d_i, marked with black dashed horizontal lines in figure 24. In this figure we observe the presence of a characteristic asymmetrical distribution of the out-of-plane current along the separatrices, with respect to the X point as typically happens in the presence of a guide field, see Ref. Pritchett and Coroniti [93] and Birn and Priest [7]. Indeed, in the presence of a guide field, the out-of plane electric field driving reconnection has a component parallel to the magnetic field, consequently electrons are accelerated and a strong out of plane current is produced; in the plane electrons move along the newly reconnected field lines causing as well a density asymmetry, see Ref. Birn and Priest [7].

As discussed before, we will analyse this high current region by looking how different quantities behave along two cuts, by wondering how this structure would appear to an imaginary satellite crossing it. This is very important for future possible comparison with turbulent magnetic reconnection events detected by satellites. This kind of analysis implies the study of the magnetic reconnection in a turbulent background, which hides the typical symmetry of the patterns normally observed in suitable numerical simulations of magnetic reconnection. Nevertheless, a number of interesting features can be recovered, we will look at the inflow/outflow regions, the out of plane current and the magnetic field topology for each of the selected cuts. The figure 25 and the figure 26 refers to the cuts at $y = 91$ d_i and at $y = 92$ d_i respectively. In the first panels, we plot two components of the magnetic field: the normal component to the current sheet B_x and the reconnecting component B_y, respectively with continuous black

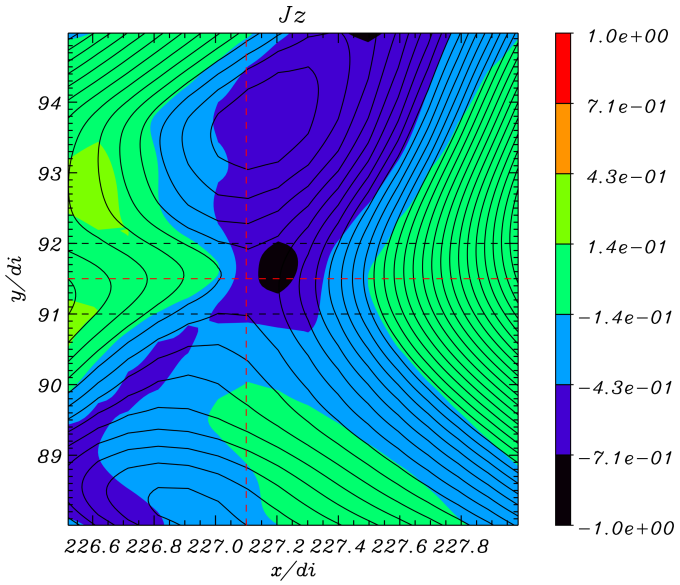

Figure 24: Iso-contours of the out of plane current, J_z, in the range $dx \times dy = [226.5 - 228]\ d_i \times [88 - 95]\ d_i$. Magnetic potential lines are shown in black. Red vertical dashed line marks the positiion of the X point. The two black dashed lines represents two cuts, at $x = 91\ d_i$ and at $x = 92\ d_i$ where the magnetic reconnection analysis will be performed.

and blue lines. For this specific current sheet the coordinate system calculated with the minimum variance technique, Ref. Paschmann and Daly [89], is a bit tilted with respect to the z-direction, however close to the simulation frame that we decide to use to analyse this structure (this is not always true for all the current sheet regions analysed). Neverthless we have uncertainties in the choice of the reference frame but qualitatively we recover an inflow symmetric with respect to the centre of the current sheet, that indicates a posteriori that this reference frame is close to the ideal one.

The B_x component is amplified by a factor 10 for the sake of clarity. In the second panels, we plot the out-of-plane current, J_z, in the third panels the inflow velocity, U_x, in the fourth panels the outflow velocities U_y and in the fifth panels the density n. In the third and fourth panel, electron and ion velocities are represented in blue and red respectively. All the velocities are in the X point reference frame by subtracting to each component the mean velocity field around the X point. A central vertical dashed line marks the position of the X point while the two continuous black lines mark the two inflow regions (going from the line towards the borders). In figures 25 and 26 we observe that the component of the magnetic field normal to the current sheet, i.e. B_x, is different from zero meaning that magnetic field lines have reconnected. Its value is positive for the cut at $y = 91\ d_i$ and negative for the cut $y = 92\ d_i$ as expected since the two cuts belong to two different sides of the X point, see dashed black

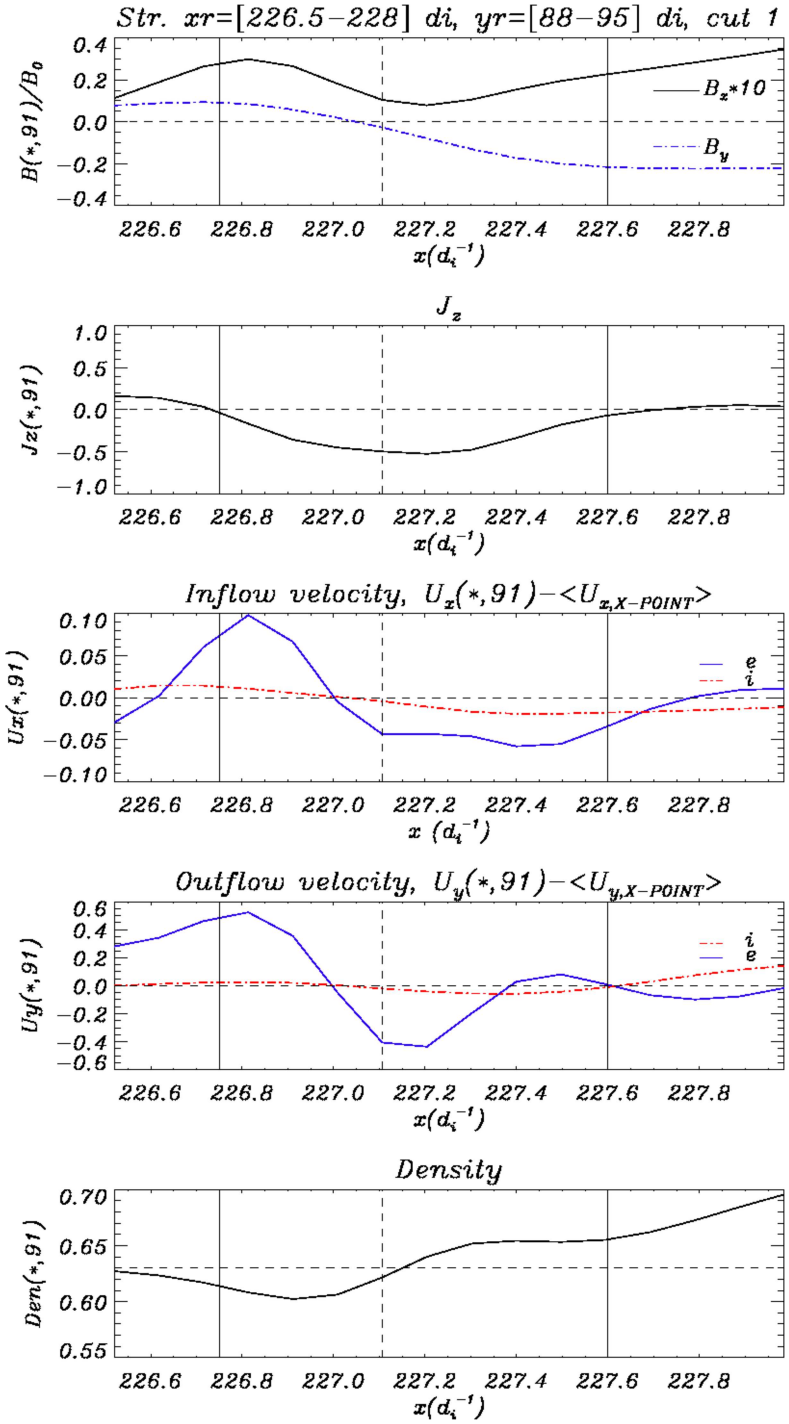

Figure 25: In the first panel we plot two components of the magnetic field, B_x in black amplified by a factor of ten and B_y blue. In the second panel we show the out-of-plane current, J_z, in the third panel the inflow velocity, U_x, in the fourth panel the outflow velocity, U_y and in the last panel the density n. In the third and fourth panels ions are represented in red and electrons in blue. Velocities are in the X point reference frame. Dashed vertical line marks the centre of the X point while continuous vertical lines points the inflow regions. All the panels refer to the cut $y = 91\ d_i$.

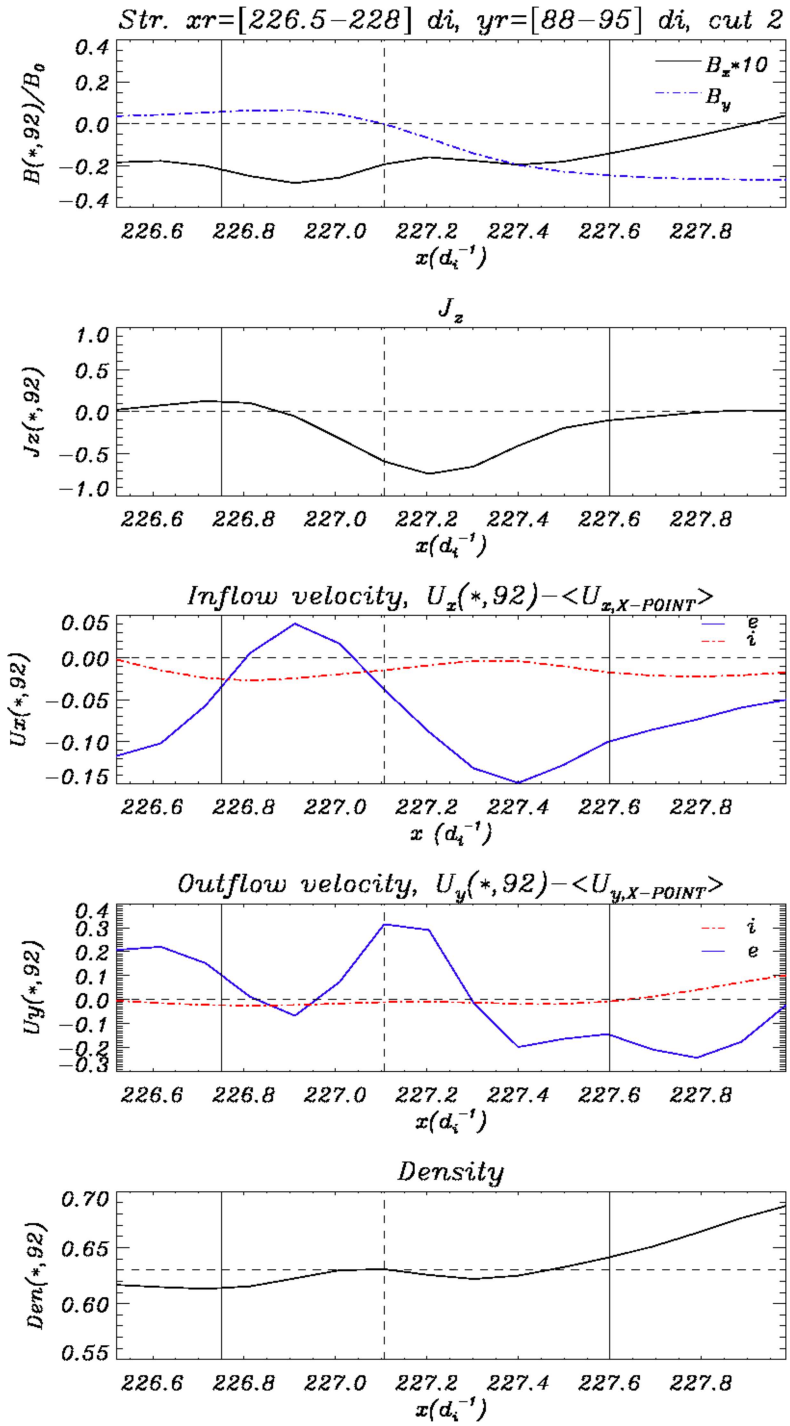

Figure 26: In the first panel we plot two components of the magnetic field, B_x in black amplified by a factor of ten and B_y blue. In the second panel we show the out-of-plane current, J_z, in the third panel the inflow velocity, U_x, in the fourth panel the outflow velocity, U_y and in the last panel the density n. In the third and fourth panels ions are represented in red and electrons in blue. Velocities are in the X point reference frame. Dashed vertical line marks the centre of the X point while continuous vertical lines points the inflow regions. All the panels refer to the cut $y = 92\ d_i$.

lines in figure **24**. The reconnecting component, B_y, plotted in blue, changes sign as crossing the separatrices going from positive to negative values in both cuts, see top panels of figures 25 and 26. This is expected since we are crossing two regions with magnetic field lines of opposite sign. In the second panels of the figures 25 and 26, we observe an increment of the out of plane current corrisponding, with a small displacement, to the X point. This is in agreement with the picture of asymmetric reconnection where the peak of the current is shifted towards the side where the magnetic field is stronger, Ref. Cassak and Shay [15], as even more clearly observed in the second panel of figure 26. The inflow velocity, in the third panels, is plotted for both ions and electrons. A positive electron velocity is observed to the left of the X point and a negative velocity to the right, since the velocity field lines are pointing towards the X-point. The mean value of the inflow velocity near the X point is $< U_{ex,Xpoint} >= 0.25$ for electrons and$< U_{ix,Xpoint} >= 0.23$ for ions. The outflow velocity in the x-direction is shown in the fourth panels in figures 25 and 26; also in this case the main flow has been subtracted. In this case, the mean outflow velocity near the X-point is $< U_{ey,Xpoint} >= 0.5$ (electrons) and $< U_{iy,Xpoint} >= 0.7$ (ions). The system is completely Hall-MHD, indeed electron and ion velocity separation (observed in both the inflow and outflow velocities) does not occur just in correspondance of the X point. For the cut under the X point at $y = 91\ d_i$, shown in figure 25, we observe, as expected, a strong negative electron velocity near the X point since electrons are accelerated in the downward direction (negative y-direction). A similar observation can be done for the cut $y = 92\ d_i$, fourth panel in figure 26. In this case, we observe an increase of electron velocity, since electrons are pushed in the positive y direction by reconnected field lines. Looking at both the inflow and outflow velocities we observe oscillations before and after the X point. Contrary, in typical magnetic reconnection configurations the outflow velocity increases only in the region of the outflow jet, in correspondance with the X point. One of the possible reason for these observations is that the structure in figure 24, is not perfectly parallel to the axis of the simulation, but it is slightly inclined towards the left in the bottom and towards the right in the half top, so that the reference frame we are considering is not perfectly aligned to the inflow/outflow directions. As a consequence part of the outflow velocity is probably affected by the inflow velocity. For comparison we analyse the same structure by making different cuts but along the inflow/outflow directions but no major differences have been found. So the other possibility is that these fluctuations are due to the surrounding dynamics. In this turbulent pattern indeed each structure is surrounded by several other similar structures, each one moving (because of vortex rotation) and possibly encountering other structures, so it is very difficult to study them, in particular to find a equilibrium

inflow/outflow regions. Moreover ions/electrons velocities at each side of the current sheets may be accelerated by other structures turbulent dynamic. Finally, electron motion along the separatrices in the presence of a guide field causes the characteristic density asymmetry, Ref. Birn and Priest [7], observed in the last panels of figures 25 and 26.

4.2.3.1 *Reconnection rate*

In our K-H Hall-MHD simulation, initializated with a guide field, the K-H vortices produce a turbulent pattern inside which magnetic reconnection is occurring. We calculate the reconnection rate and compare it with the results typically obtained in literature with similar simulations or observations. We put particular attention to the asymmetry of our reconnection structure. On this purpose we distinguish two inflow regions from each side of the X point. We indicate as R-I the inflow region in the range $[226.5 - 226.75]\ d_i$, and as R-II the inflow region in the x-range $[227.6 - 228]\ d_i$.

To select these regions we use the out-of-plane current and consider the regions where $J_z \sim 0$. In asymmetric turbulence the reconnection rate is obtained by multiplying the aspect ratio by the outflow speed and the mean magnetic field in the two inflow regions, Ref. Cassak and Shay [15]:

$$E \sim \frac{B_1 B_2}{B_1 + B_2} v_{out} \frac{2\delta}{L} \tag{34}$$

The aspect ratio is defined as δ/L, where δ is the half width and L is the half length of the reconnection layer.

In table 2 we report the calculation of some parameters in the two inflow regions. From top to bottom: the total magnetic field B_{tot}, the inflow velocity (U_x) over the local Alfvèn velocity in the inflow region, $V_{inf}/V_{A,inf}$, the opening angle B_x/B_y, the density n, the aspect ratio δ/L and the asymmetric reconnection rate, E, see eq. 34. In this table we indicate the cut at $y = 91\, d_i$ and at $y = 92\, d_i$ as cut I and II respectively.

First, we observe that the intensity of the total magnetic field, B_{tot}, is not the same in the two inflow regions. Considering cut I, we observe that its value varies from $B_{tot} = 0.67$ in R-I to $B_{tot} = 0.56$ in R-II, characteristic of asymmetric reconnection. In the second row of table 2, we observe that the mean value of inflow velocity over the local Alfvèn velocity changes in the two inflow regions, varying, for cut II, from $V_{inf}/V_{A,inf} = 0.18$ in the R-I to $V_{inf}/V_{A,inf} = 0.34$ in the R-II. This quantity is normally used as an estimation of the reconnection rate (RR) and since its value changes in the two inflow regions we can not say which of the values better correspond to the

	CUT I		CUT II	
	R-I	R-II	R-I	R-II
B_{tot}	0.67	0.56	0.68	0.59
$V_{inf}/V_{A,inf}$	0.30	0.34	0.18	0.34
$V_{A,inf}$	0.85	0.70	0.68	0.59
B_x/B_y	0.24	0.1	0.24	0.08
n	0.62	0.67	0.61	0.66
δ/L	0.47		0.32	
E	0.16		0.11	

Table 2: In this table we report the value of the total magnetic field, the inflow velocity over the local Alfvèn velocity, the opening angle B_x/B_y, the density n, the aspect ratio δ/L and the reconnection rate modified for the asymmetric case, E. These parameters are reported for both the two inflow regions of cut I and cut II.

actual RR. For this reason we need to estimate the RR considering the asymmetry of the system.

In the third row of this table, the quantity B_x/B_y is the ratio between the normal and the reconnecting component of the magnetic field. Also in this case, this quantity changes in the two inflow regions, varying from $B_x/B_y = 0.24$ to $B_x/B_y = 0.1$. Moreover, the system is also characterized by a density asymmetry, see fourth row of table 2, where density varies in the two inflow regions from $n = 0.62$ to $n = 0.67$ for cut I, and from $n = 0.61$ to $n = 0.66$ for cut II.

In order to take into account possible effects due to an asymmetric configuration, the aspect ratio δ/L can be estimated as it is done in Ref. Cassak and Shay [15], where it is estimated as:

$$\frac{\delta}{L} = \frac{\rho_1 v_1 + \rho_2 v_2}{2\rho_{out} v_{out}}$$

In this equation the outflow velocity is $v_1 \equiv v_{out-cut\ I}/v_A = 0.54$ for cut I and $v_2 \equiv v_{out-cut\ II}/v_A = 0.53$ for cut II. The outflow density is estimated as: $\rho_{out} \sim (\rho_1 B_2 + \rho_2 B_1)/(B_1 + B_2)$. By re-writing eq. 34, we obtain:

$$E = \frac{B_1 B_2}{B_1 + B_2} v_{out} \frac{2\delta}{L} = \frac{B_1 B_2}{B_1 + B_2} v_{out} 2 \left(\frac{\rho_1 v_1 + \rho_2 v_2}{2\rho_{out} v_{out}} \right) = \frac{B_1 B_2}{\rho_1 B_1 + \rho_2 B_2} (\rho_1 v_1 + \rho_2 v_2)$$

The correspondent reconnection rate, obtained from equation 34, gives then the normalized values of $E_{cut-I} = 0.16$ and $E_{cut-II} = 0.11$

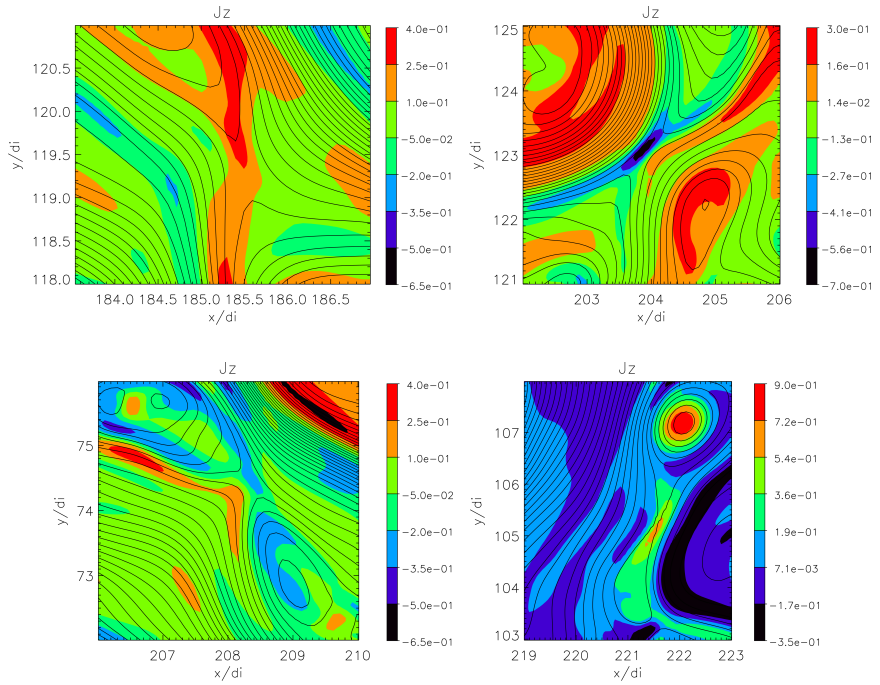

Figure 27: Zooms of the iso-contour of the out-of-plane current J_z , with magnetic potential field lines in black. The structures in the four panel have been detected using PVI method.

respectively obtained for cut I and II. These values are consistent with the ones obtained typically in Hall reconnection in the past literature, see e.g. Ref. Huba [61], Pritchett and Coroniti [93] and Retinò et al. [95].

4.2.3.2 *Other reconnection structures*

As discussed before, using the PVI method we single out the most intense current structures and we note that some of them are reconnection regions. In figure 27, we plot the iso-contours of the out-of-plane current, J_z, for few other reconnection regions, like the one described in section 4.2.3. The typical features of a reconnection event are recovered also for these cases, by doing, as before, a cut just above or under the X-point and analysing the magnetic field, the velocities in the inflow and outflow regions and the current (not shown here). In the top panels of figure 27, the asymmetric distribution of the current along the separatrices, already observed for the structures analysed in detail in section 4.2.3, is evident. In the bottom panels, instead, the reconnection is in a final stage, indeed magnetic island already formed so in these two last cases we do not observe anymore, for example, the typical outflow jet.

4.3 DISCUSSION AND CONCLUSIONS

In this work we have performed the analysis of the turbulence spontaneously developed inside a K-H vortex in its saturated phase, characterized by small scale structures of the order of one inertial length or less. 2D turbulence has been studied by selecting a square box inside the most turbulent area to avoid large scale non turbulent ribbons of the vortex itself.

The 2D spectral magnetic energy of the magnetic field fluctuations around the mean field shows an initial anisotropy in the $(k_x\ k_y)$ wavevector space. The anisotropy has been quantified using the Shebalin angle calculated at various times of the simulation; an increasing isotropy is observed going on with the simulation.

Once isotropy has been established, we calculate the 2D spectrum integrating over concentric shells the two dimensional spectral magnetic energy. A power-law spectrum with a slope of $k_\perp^{-2.6}$ has been recovered at ion scales, in agreement with recent PIC simulations, Ref. Karimabadi et al. [62]. To characterize the turbulence we look at the power distribution functions of the magnetic field increments (PDFs). Increments of the magnetic field have been calculated for various scales, from $\ell = 1.5\ d_i$ to $\ell = 19\ d_i$. PDFs show tails with respect to a Gaussian distribution and these tails are increasing when going to smaller scales, typical of intermittency in plasma turbulence. The steering away from Gaussianity is quantified through the flatness, i.e. the fourth order moment of magnetic field increments and we observe an increase of flatness going at smaller and smaller scales consistent as well with results of PIC simulations.

The same analysis has been performed, for comparison, on a second box selected outside the turbulent region. In this case, as expected, the PDFs follow nearly a Gaussian distribution and flatness is almost constant at all scales. Through the PVI, we have selected the structures that show the highest magnetic field fluctuations and are responsible of the tails observed in the PDFs. By counting the number of structures with a PVI and current $|J_z|/\sigma$ higher then a certain threshold we observe that the highest current regions occurs at scales of the order of one inertial length or less. By looking at these structure, we obtain that some of them are reconnection regions. The detailed analysis of one reconnection structure shows the main features of an asymmetric magnetic reconnection process. Magnetic reconnection has been studied as usually done when using satellite data by looking how different quantities behave along the crossing. This kind of analysis is usually not performed in simulations of turbulence because of the difficulties to isolate completely each reconnection structure from the full system. For example, it is not easy to select the inflow regions without these being influenced by the surrounding dynamics. In view of possible comparison with satellite observations

it is however important to perform such an analysis. Indeed it can be possible to find a series of observational events in which satellites cross the K-Hs vortices in the non linear phase and so being able compare simulations with spacecraft data turbulence and have better understanding of the small scale dynamic taking place.

From the numerical point of view, we plan in future to perform other simulations increasing the resolution such as to resolve even smaller scales and to study as well the dissipation of the magnetic reconnection structures.

Part III

SIMULATIONS OF KELVIN-HELMHOLTZ INSTABILITY AT THE MAGNETOPAUSE INITIALIZED WITH EXPERIMENTAL PROFILES

5

SIMULATIONS BASED ON SATELLITES CROSSINGS OF THE MAGNETOPAUSE

In this chapter we discuss how we can get experimental large-scale field profiles from satellite data to be used as initial conditions in two-fluid simulations of the Kelvin-Helmholtz instability. The possibility of finding the most realistic initialization for our simulations is a fundamental point. Indeed, the numerical analysis of these last ten years have shown that the system dynamics strongly depends on the initial large scale field profiles used to initialize the simulation by affecting the long time evolution of the K-H instability as a consequence of the competition between different non-linear processes arising on the shoulder of the vortices formed by the primary K-H instability, as discussed in chapter 2. This aspect has been stressed out by previous simulations considering different plasma conditions in studying the K-H, using different initial velocity jumps, different density and velocity gradients, see Ref. Nakamura et al. [80], Faganello et al. [30], Matsumoto and Seki [74], Henri et al. [56]. Often, numerical simulations are initialized with reasonable profiles based on characteristic values obtained from observational results, Ref. Takagi et al. [115], but initial conditions not always correspond to the observed configurations. Indeed the initialization of the simulation is often changed to reduce computational time and/or to study one particular aspect of the instability, for example how it is affected by the density jump, Ref. Faganello et al. [30]. In this work, Ref. Rossi et al. [98], we have performed simulations using the closest initial condition to the real observed ones by doing a fit on satellite crossings. This improvement is very important if we want to reproduce correctly the physics occurring in this region. For these reasons in this work, our strategy is to look for satellites crossings of the magnetopause favorable for K-H but without the instability being already developed in order to recover profiles as close as possible to actual condition to be used in our simulations.

In section 5.1 we present the criteria used for the selection of the events and we discuss the plasma conditions during the selected events; in particular we focus on the event of the 2001-11-20, discussed in section 5.2. The profiles obtained from the crossings are

shown in section 5.3 and finally in section 5.4 we present the results of the simulations initialized with realistic profiles.

5.1 SELECTION OF CLUSTER DATA EVENTS

During southward IMF, magnetic reconnection is the leading mechanism that plays at the dayside magnetopause, caused by the interaction between the IMF with northward geomagnetic field lines, while K-H is not favored. Dayside reconnection is responsible for solar wind (SW) plasma transfer into the Earth's magnetosphere; see section 1.3.1 for more details. Observations however reveal the presence of SW plasma populations also during northward IMF, Ref. Fujimoto et al. [44], Matsumoto and Seki [74] when dayside reconnection cannot develop. For this reason, the K-H instability is thought to be one of the possible mechanisms responsible of SW plasma transport during northwards conditions, see Ref. Scholer and Treumann [103]. Observations of K-H vortices during northward IMF can be find in Fairfield et al. [34], using Geotail and in Hasegawa et al. [50, 53], Foullon et al. [37] using Cluster satellites.

Since there wasn't any available list from earlier study on K-H instability already compiled, based on earlier observations, we have first made an event search in the Cluster Archive Archive (CAA) using the AMDA web tool. AMDA is an online tool that allows fast browsing of spaceraft data, including Cluster and Geotail (http://cdpp1.cesr.fr/AMDA-NG/index.html). Following the idea of looking for events favorable for K-H to occur, during which the instability has not developed yet, we search for events where a change in the interplanetary magnetic field (IMF) from southward to northward occurs at a time close to a satellite magnetopause crossing and stays positive for a long period. By selecting crossings just after the IMF rotation we have high probability to detect configurations in which K-H conditions just settled but the instability has not yet developed. Moreover, we have imposed that the satellite is located as close as possible to the equatorial plane ($|z_{GSM}| < 5R_E$), since the K-H instability can be inhibited by the presence of a magnetic field component along the flow direction (magnetic tension) we require the out-of plane magnetic field to be dominant with respect to the other components of the magnetic field. This research has been then refined by visual inspection. Due to the polar orbit of the Cluster mission, the above constraints are quite strong and the fulfilment of all these requirements is not straightforward so only a few events have been selected. In total we found eight events, three of them were selected as "good" e.g. characterized by a stable positive IMF and an appreciable velocity shear. These event are:

Event 1: 2001-05-26 in the time interval 08:00-18:00 (UT)

Event 2: 2001-05-30/31 in the time interval 20:00-09:00 (UT)

Event 3: 2001-11-20 in the time interval 08:00-12:00 (UT)

among them, we present in the next section the event of 2001-11-20.

5.2 EVENT 2001-11-20

Here we present one of the events we found in our statistics, the one of 2001-11-20, that has been already studied by Hasegawa et al. [50], Foullon et al. [37] and by Foullon et al. [37]. This event is of particular importance because we have the conjuction of Geotail, orbiting near the dayside magnetopause (MP), with Cluster crossing the MP at the dusk flank. During this event the IMF, measured by ACE in the Solar Wind, changes direction around 06:00 (UT) and it stays positive for a long time, about 18 hours, by Ref. Foullon et al. [37]. The closest crossing in time, of the after this inversion of the IMF is in the time interval [09:26:02-09:26:30] (UT) when Cluster satellites enter into the magnetosphere/boundary layer. A confirmation that this event is under favorable conditions for K-H to occur, is given by the observation of rolled-up K-H vortices, detected later in time, in the interval [20:26-20:42] (UT), by Cluster satellites, see Ref. Hasegawa et al. [50, 52]. The vortices observed at the dusk flank by Cluster can either origin at the nose, as shown by Ref. Hasegawa et al. [53], or they can origin locally in an intermediate position between Geotail and Cluster, see Ref. Foullon et al. [39, 37, 38].

During the time interval [19:19:10 - 19:36:30] (UT), Geotail crosses several times near the nose, measuring small perturbations that are supposed, Ref. Hasegawa et al. [50, 53], to be the initial small amplitude signatures of the instability observed later on with Cluster in the form of fully developed vortices. Neverthless, data also suggest the possibility for the instability to develop along the flank of the magnetopause itself. The relative position of the IMF induce indeed the formation of a region locally favorable for the K-H development, Ref. Foullon et al. [38, 39].

There are two different Cluster crossings, the first one is just after the IMF B_z inversion and it represents a good measure of an unperturbed magnetopause (before K-H develops) and the second crossing is about fifteen hours after the first, detecting instead vortices structures. This last case, clearly, is not considered in the research of the initial condition but it has been used to compare the observed K-H with the results of the simulations. We have analyzed all the multiple crossings of Geotail in the time interval [19:19:10 - 19:36:30] (UT), and the crossing of Cluster satellites in the time interval [09:26:02-09:26:30] (UT), where no vortices have yet formed, and check if they can be used as possible initial condition events for our simulation.

In figure 28, we show the position of the satellites during their respective periods in the GSM reference frame. In the Geocentric Solar Magnetospheric (GSM) reference frame the x-axis points from the Earth to the Sun, z-axis is directed toward Earth's geomagnetic north

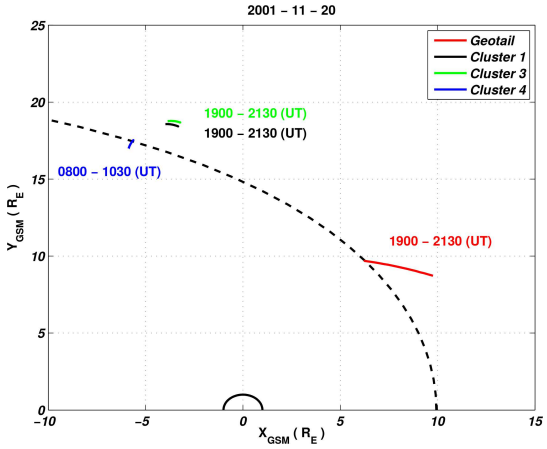

Figure 28: Geotail and Cluster orbits in the GSM reference frame during the event 2001/11/20. Geotail is represented with a red continuous line in the interval dt = [19:00–21:30] (UT). Cluster–1 and Cluster–3 orbit during the same time interval as Geotail are shown with a black and green continuous lines. Cluster–4 orbit in the time interval dt = [08:00–10:30] (UT) is plotted in blue. The magnetopause is shown with a black dashed line and its position is obtained using the Shue model, Ref. Shue et al. [108].

dipole and y-axis is obtained from their cross product. In this figure, Cluster partial orbit in the time interval [08:00:00 - 10:30:00] (UT) is represented with a blue continuous line. Geotail and Cluster orbits in the time interval [19:00:00 - 21:30:00] (UT) are show with a red, black (Cluster–1) and green (Cluster–3) continuous lines. Black dashed line represent the position of the magnetopause obtained using the Shue magnetopause model, Ref. Shue et al. [108]. For the sake of clarity, wider time intervals than the interval of the crossings have been selected. This figure shows the particularity of this event where we were able to measure at the same time the dayside and the dusk flank plasma.

The interplanetary magnetic field as a function of time is plotted in figure 29. It is measured by the ACE satellite and it is shifted in time of dt=[00:54:16] in order to be compared to Cluster measurements, by taking the difference between the time when the change of sign of B_z is observed by ACE and by Cluster (before crossing the magnetopause). This time lag is also confirmed by taking the Solar Wind propagation time into account. Indeed, since the bulk velocity is around 475 km/s and ACE-to-Cluster distance is around 244 R_E it should take around 54 minutes for the IMF to propagate to Cluster. The components of the magnetic field, B_x, B_y and B_z are plotted with black, blue and red continuous lines respectively. In this figure there are two light shaded regions.

The one in light blue corresponds to the time interval when Cluster is crossing the magnetopause, i.e. [09:26:02-09:26:30] (UT), while

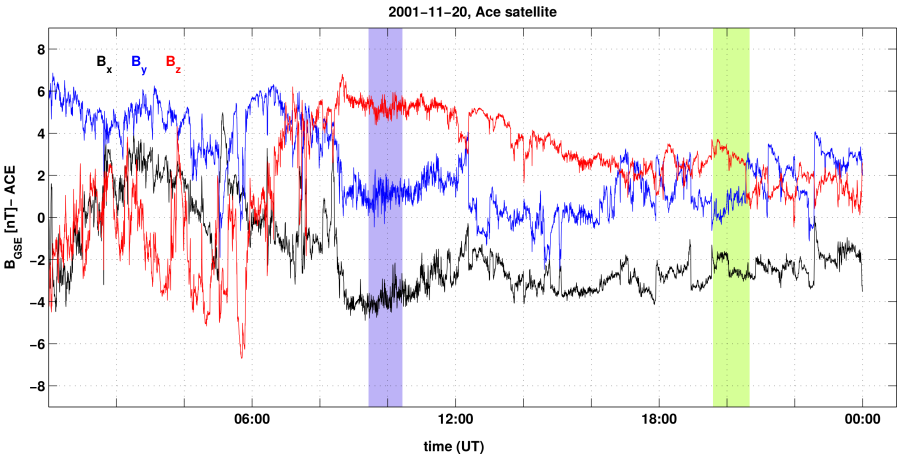

Figure 29: The plot of the IMF during the day of the 20th November 2001 as a function of time shifted of dt=[00:54:16] in comparison to Cluster measurements. B_x, B_y and B_z are plotted respectively with black, blue and red continuous lines. The light blue and light green shaded regions correspond respectively to the time when Cluster and Geotail are crossing the magnetopause.

the light green area corresponds almost to the time when Geotail is crossing the magnetopause, i.e. [19:19:10 - 19:36:30] (UT). ACE IMF data have been propagated at Cluster, the IMF data delay between Geotail and Cluster is of about 7 minutes, Ref. Foullon et al. [37]. Monitoring IMF during the selected crossings is very important to verify that it is constantly directed northwards. We focus now on the density and velocity profiles measured by satellites when crossing the magnetopause. Since, for the selected event, the magnetic field components are nearly parallel across the layer and variations in intensity are not particularly strong, we consider the variation of the moments when a satellite crosses this boundary together with the presence of a shear of the magnetic field as a typically signature of a magnetopause crossing, Ref. Hasegawa [54]. Indeed, going from the magnetosphere to the magnetosheath, during a magnetopause crossing, a satellite measures an increase of the density and a decrease of temperature, since the magnetosheath plasma is denser and colder compared to the magnetosphere and we select the crossing when such variations are observed together with a variation of the velocity field.

5.3 VELOCITY AND DENSITY PROFILE ESTIMATION

For all the selected crossings, we determine the velocity shear and the density profile by adopting a fit technique (Levenberg-Marquardt technique to solve the least-squares problem) with an hyperbolic tangent of the form:

$$f = A + B \tanh\left(\frac{x - x_C}{D}\right) \tag{35}$$

The fit is made to determine the parameters that in the least-squares sense fit at the best the data; i.e. the sum of the weighted squared differences between the model and data is minimized. It is remarkable that, in all cases we have analysed, the hyperbolic tangent function is a very good profile shape to represent the data. Using equation 35, we obtain information on the total jump of the mean velocity and density by using the parameters A and B, we recover the centre of the profile x_C and the characteristic shear length D. Before making the fit, we multiply the time interval of the selected crossing by the estimated magnetopause velocity, $\ell = v_{MP} \cdot \Delta t$, in order to understand how the profiles vary in space. The magnetopause velocity, v_{MP}, has been estimated by comparing the value obtained using the De Hofmann-Teller technique, see Ref. Paschmann and Daly [89], with the plasma flow in the normal direction, in the hyphothesis that the magnetopause is a tangential discontinuity. From the fit we obtain the velocity and density profiles and we use them as initial condition for the Two-Fluid simulation. In this code the velocity is normalized to the Alfvèn velocity in the magnetosheath and the density to its value in the magnetosheath; for this reason the total velocity and density jump will be normalized as $\triangle U/v_{A,msh}$ and $\triangle n/n_{msh}$.

In the next sections we show that a shift is recovered between the density and the velocity profile centers. In order to isolate the effect of this shift, in these simulations temperature is assumed constant, by taking its value from a mean on the data, and the magnetic field profile is obtained imposing an initial total pressure equilibrium. Nevertheless, in the data there is a strong variation of the temperature profile during the crossings (varying from about 400 eV in the magnetosheath up to 1200 eV in the magnetosphere) and as regards the magnetic field a small variation is observed as well (of the order of 10 nT recovered during the crossing of Cluster and of about 3 nT during Geotail crossings). In the future we will include also a fit of the temperature and magnetic field measured profiles in the initial condition in our simulations. In the next section we provide details of the density and velocity estimation for each crossing. The quality of the fit is given by the the correlation coefficient R^2, defined as

$$R^2 = 1 - \frac{\sum_{i=1}^{N} \left(f_i - \hat{f_i}\right)^2}{\sum_{i=1}^{N} \left(f_i - \bar{f_i}\right)^2}$$

i.e. one minus the sum of the square of the differences between the original f_i and the fitted $\hat{f_i}$ profiles, over the total sum of square, $f_i - \bar{f_i}$ where $\bar{f_i}$ it is the mean of the original data. R^2 varies from zero to one. When it is zero it means that the fit does not follow at all the original profile while when it approaches to one it means that the model fits good.

In the next sections we present the results of the fit applied to Cluster and to Geotail crossings, sections 5.3.1 and 5.3.2.1 respectively.

5.3.1 *Cluster Crossing*

In this section we describe the first magnetopause crossing by Cluster satellites after the IMF inversion from southward to northward, see figure 29, in the time interval [09:26:02-09:26:30] (UT). As discussed in section 5.2, this crossing represents a good approximation of an initial unperturbed magnetopause (MP) condition. In this case the MP is a thin tangential discontinuity with a thickness recovered, for the velocity and density shears, across this layer around one inertial length. This crossing occurs about nine hours before the one analysed by Hasegawa et al. [52, 53], Hasegawa [54] and three hours after the change of the B_z component of the IMF, see the light blue shaded region in figure 29 in comparison with the B_z (in red) inversion at [06:00] (UT) in the same figure. During this crossing, shown with a light blue continuous line in the left panel of figure 28, the satellites are not exactly in the equatorial plane. In particular, the Cluster position in GSM coordinates is $r_{Cluster} = [-8.6, 30.8, -3.8]\ R_E$. Data will be treated in a reference frame in which one of the axis corresponds to the direction of the cross product of the mean electric and the mean magnetic field, i.e. $\hat{e_i} =< \mathbf{E} > \wedge < \mathbf{B} >$; the second axis is given by the direction of the mean magnetic field, $\hat{e_j} =< \mathbf{B} >$, and the third axis is $\hat{e_k} = \hat{e_i} \wedge \hat{e_j}$ given by the $\mathbf{v} \wedge \mathbf{B}$ product. Using the Shue model, Ref. Shue et al. [107, 108], we estimate the normal to the magnetopause $\hat{N}_{Shue} = [0.32, 0.94, -0.14]$. This value is comparable with the direction $\hat{e}_k = [0.42, 0.91, -0.07]$ of our reference frame. The velocity field is obtained from the $E \wedge B$ drift and resampled to the CODIF, see section 1, measured velocity. Taking the $E \wedge B$ drift velocity is analogous to consider the perpendicular CODIF velocity. This choice has been made in order to isolate the shear component. Density is obtained using the spacecract potential, Ref. Pedersen et al. [91], to have higher resolution density measurements than CODIF instrument, equivalently PEACE electron moments can be used as done in Ref. Foullon et al. [37].

In figure 30 by observing the decreasing density and velocity field, respectively in the first and second panels, we know that the satellites are encountering a magnetospheric-like plasma, the electron boundary layer (EBL) region, as shown in Ref. Foullon et al. [37]. As expected temperature increases going towards the magnetosphere (third panel) and despite the approximation of constant magnetic field, a variation is observed as well in the magnetic field of about 20 nT (in the fourth panel), the same variation is seen in the Alfvèn velocity (in the fifth panel) in corrispondence with the density gradient. The Alfvèn velocity, in the bottom panel, is almost constant in the magnetosheath/magnetosheath boundary layer (MSH/BL) in the left side of this figure. The magnetopause velocity is used to get density and velocity profiles variations with respect to length before doing the fit,

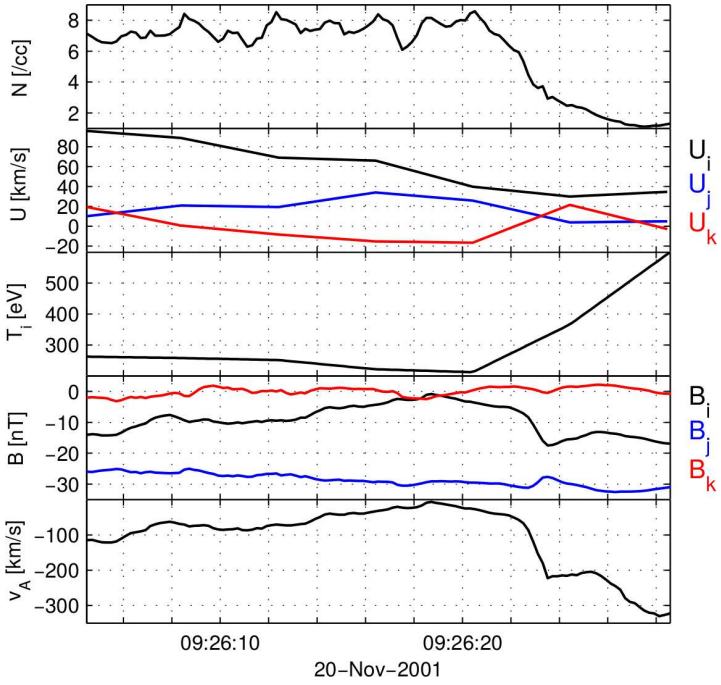

Figure 30: In the first panel we plot the density, in the second panel the velocity field, in the third panel the ion temperature, in the fourth panel the magnetic field and in the fifth panel the Alfvèn velocity, each panel in the time interval Δt = [09:26:02-09:26:30] (UT).

see section 5.3, and it is estimated to be $\langle v_{MP} \rangle = 16\,km/s$. Its positive value means that the magnetopause is moving in the positive direction of the normal, and since the normal vector points outward with respect to the magnetopause, it means that Cluster satellites are crossed by the magnetopause that is expanding. In other words, the satellites are going towards the magnetosphere region, as confirmed by figure 30. In figure 31 we plot in the top panel the velocity and in the bottom panel the density profile. The blue lines represent the profiles obtained from a fit with an hyperbolic tangent and the blue dots the center of these profiles. In each panel we include the estimation about the quality of the fit, R^2, the shear length L_{eq} and the separation between the centers of the density and velocity profiles, $|x_{c,n} - x_{c,U}|$.

Observing figure 31, first we notice that the choice of an hyperbolic tangent is well suited as confirmed by the value of R^2. This quantity is good for both fit, being $R^2 = 0.94$ and $R^2 = 0.96$ for the density and velocity profiles respectively. Moreover we observe that there is a shift between the density and the velocity profiles, defined by the quantity $|x_{c,n} - x_{c,U}|$, where $x_{c,n}$ and $x_{c,U}$ are the centers of the hyperbolic tangent of the density and velocity respectively , obtained from the fit. The separation, in ion inertial length units, is $|x_{c,n} - x_{c,U}| = 1.7\,d_i$ and it is of the same order of the velocity shear length, $L_{eq} = 1.6\,d_i$. A velocity shear outside the magnetopause, in the boundary layer

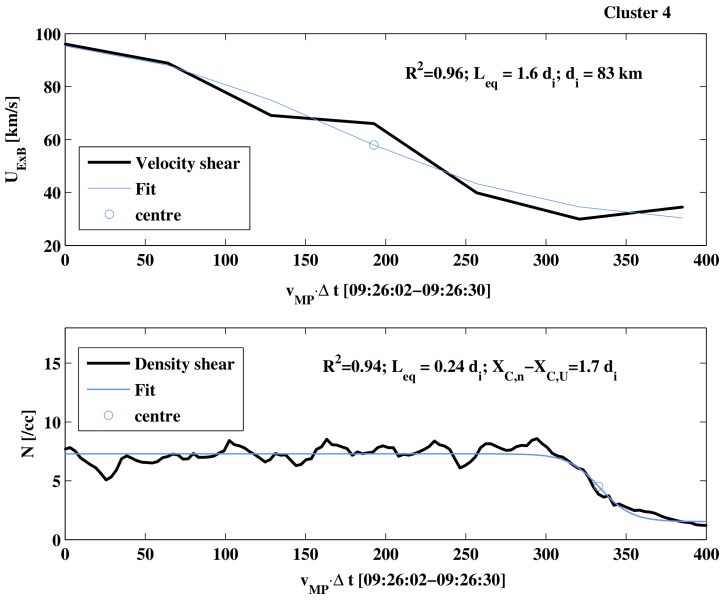

Figure 31: In the top panel the plot of the density and in the bottom panel the velocity, both shown with a black continuous line. The superposed blue line represents the fit profile and the blue dot represents the position of the centre of the hyperbolic function. In each panel there are the values of the goodness of the fit R^2, the shear length L_{eq} and the separation, in absolute value, between the center of the density and velocity profiles, $|x_{c,n} - x_{c,U}|$.

between the EBL and the MP has been observed as well during this event in Ref. Foullon et al. [37], consistently with our result. Considering possible uncertainties on the evaluation of the velocity of the magnetopause, that could influence the scale lengths, we can consider also the density shear length $L_{eq} = 0.24\, d_i$ to be also of the order of one ion inertial length as the other ones.

5.3.2 *Geotail data: Multi-crossings event*

As discussed before, the vortices observed at the flanks of the magnetopause during November the 20th 2001 in the time interval [20:26-20:42] (UT) by Cluster satellites can either take origin at the dayside magnetopause, Ref. Hasegawa et al. [53] or develop in a region between Geotail and Cluster position, see Ref. Foullon et al. [39, 38] for details. In the time interval [19:19:10-19:36:30] (UT) Geotail satellite, which position is approximately [7.5,10.5,0] R_E, crosses multiple times the dayside magnetopause and we consider each one of these crossings. We identify eight transitions, that present a clear velocity shear, they are marked in figure 32 with numbers and vertical dashed black lines. For each of them we will analyse density and the velocity profile. In this figure we plot in the first panel the density, in the second panel the velocity field, in the third panel the parallel and

perpendicular ion temperatures, in the fourth panel the three components of the magnetic field and in the fifth panel the Alfvèn velocity. Typically a magnetopause crossing is identified by a significant magnetic field shear and a variation of its intensity. During Geotail crossing, however magnetic field components are nearly parallel across the layer except an initial variation of the magnetic field from 20 nT to 40 nT measured around 19:18 (UT), see fourth panel. To identify a magnetopause crossing, together with a variation of the intensity of the magnetic field, it is necessary to analyse the other plasma properties. For this reason we use ion data as well to check when the satellite crosses the magnetopause, Ref. Le et al. [66], Bauer et al. [5]. In particular regarding plasma properties we identify possible MP crossings as where a strong velocity shear is combined with a variation of the density and of the temperature profiles, see end of section 5.2 and we mark these transitions with vertical dashed lines. Using a model of the magnetopause, Ref. Shue et al. [107, 108], that determines the location of the magnetopause by imposing a pressure balance between the SW dynamic pressure and the pressure of the geomagnetic field, we calculate the normal of the magnetopause. By knowing the coordinates of Geotail position we obtain that the normal is $\hat{N}_{Shue} = [0.8, 0.6, 0]R_E$. All the physical quantities for Geotail are treated in the boundary normal coordinate system, Ref. Russell and Elphic [99], see section 3.3.4, where $\hat{N}$ is the magnetopause normal obtained with the Shue model, $\hat{L}$ is in the plane perpendicular to $\hat{N}$ and almost directed northward the equatorial plane and finally $\hat{M}$ is chosen to complete the right handed reference frame; for more details see section 3.3.4.

The results of the analysis on the density and velocity profiles performed on each of the selected MP crossings are listed in table 3. The analysis on the experimental crossings suggests that the centers of the density and velocity profiles are shifted with respect to each other by a distance comparable to their shear length, i.e. around one inertial length.We underline here that these crossings are taken during the initial phase of the instability and as we know from the simulations (see following section 5.4.0.2 and figure 40 therein), in the linear phase, the initial plasma configuration is not affected by the instability so the observed shift is not a consequence of K-H development, but is preexisting and possibly corresponding to the boundary layers adjacent to the magnetopause, see Ref. Bauer et al. [5], Phan et al. [92], Fujimoto et al. [43]. Moreover it should be noted that as going from the magnetosphere to the magnetosheath regions, the shift is not occurring always in the same direction, as we observe in the last column of table 3. The direction of the shift does not also depend on the instability in the linear phase, see second row panels in figure 40. By analysing in detail the fits, we note however that only for two of them (Geotail crossings 1 and 6) it is possible to identify a clear hyperbolic tangent

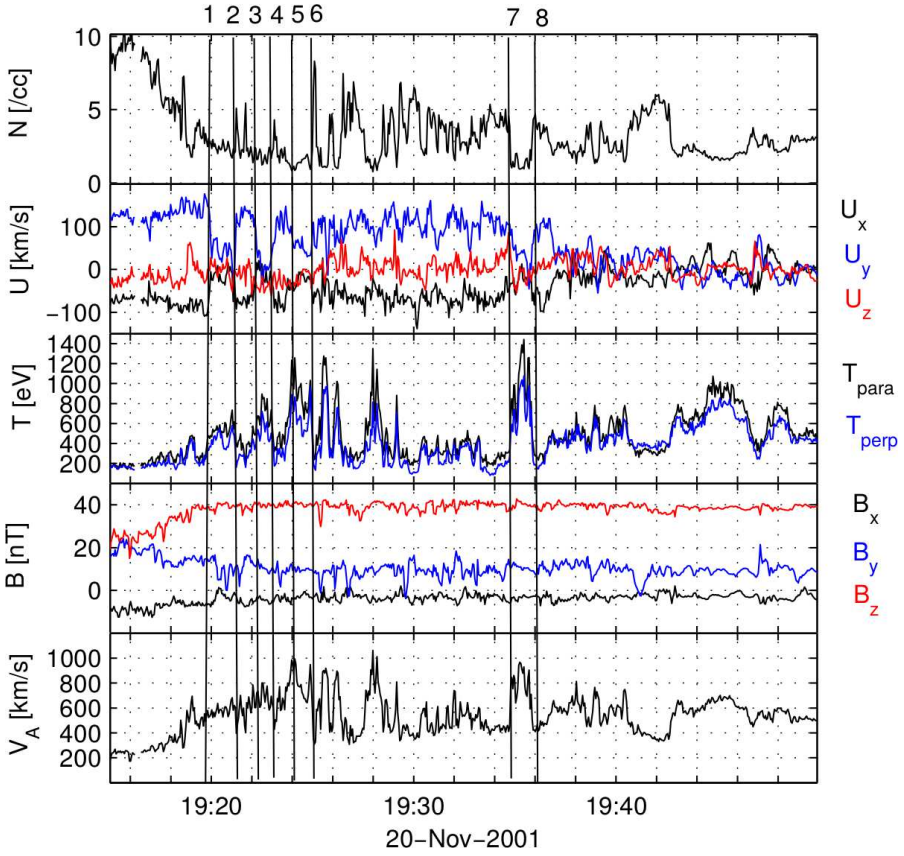

Figure 32: Overview of measurements at Geotail in the time range Δt = [19:15:00-19:50:00]. From top to bottom: density, velocity field (U_x in black, U_y in blue and U_z in red), parallel and perpendicular temperaures (in black and blue respectively), magnetic field (B_x in black, B_y in blue and B_z in red) and Alfvèn velocity. Dashed vertical lines stand for all the sharp variations in density or velocity multiple crossings that have been analyzed in the text.

for at the same time both N and V. The other cases show either a clear N profile or a V profile. Moreover the variations between 2 and 5 seem most likely to be inside the boundary layer, Ref. Le et al. [66], since the highest values of the density for these crossings does not reach the value measured in the magnetosheath, around 8 /cc.Cluster show a negative shift going from the magnetosphere to the magnetosheath regions ($x_{c,n} - x_{c,U} < 0$) that can be explained by the dual lobe reconnection, that can occur together with K-H instability when IMF is northward. Under such case, a closed and dense boundary layer is formed, caused by the double lobe reconnection, Ref. Song and Russell [110] or, due to a magnetosheath acceleration, a velocity shear is measured in the boundary layer just outside the magnetosheath. Geotail crossing 1 and crossing 6 show instead a positive shift going from the "magnetosphere" to the "magnetosheath" regions, possibly the velocity shear occurring in the inner side of the magnetopause. In any case, further investigation are required to understand the reason

of such observed shifts in the velocity and density profiles. Now we provide details of some of the Geotail crossings selected in the time interval [19:19:10-19:36:30] (UT).

5.3.2.1 *Details of Geotail Magnetopause crossing*

Analysing all the variations presented in figure 32, only few of them were presenting a clear density and velocity shear and were closed to a MP crossing such to evaluate correctly the shear lengths and the eventual separation between the profiles. Here we present the details of crossing 1 and crossing 6, as numbered in figure 32.

- Crossing 1, time interval Δt = [19:15:30-19:21:00] (UT).

In figure 33 we show a zoom on the principal quantities, density, velocity, temperature and the magnetic field during crossing 1. The velocity shear, in the top panel, is occurring after the density gradient (as going from the magnetosheath to the magnetosphere/inner BL). The density gradient is smooth and simultaneous with the B gradient, shown in the fourth panel of figure 33. Then in corrispondance of the temperature gradient (T increasing as going towards the magnetosphere) the satellite measures a strong velocity shear, characterized by a sharper gradient with respect to the density and magnetic shear length. In figure 34 we show the first of the multiple crossings by Geotail. In the top panel we plot the m component of the velocity field and in the bottom panel we plot the density. A fit with an hyperbolic tangent is shown by a green line and the center of the fitted profile by a green dot. Inside each panel we explicity show the quality of the fit, that is $R^2 = 0.83$ for the velocity profile and, $R^2 = 0.92$, for the density one. The shear lengths are $L_{eq,U} = 0.3\, d_i$ for the velocity and $L_{eq,n} = 19.5\, d_i$ for the density gradient while the separation between the centers of the two profiles around $|x_{c,n} - x_{c,U}| = 27.5\, d_i$. The satellites are initially in the magnetosheath and then they cross the magnetopause entering into the boundary layer close to the magnetosphere, indeed both the velocity and the density are decreasing. Both plots are given as function of space in km, obtained multiplying the magnetopause velocity, $v_{mp} = 15\,km/s$, by the selected time range, i.e. $\ell = v_{mp} \cdot \Delta t$.

Looking at the bottom panel of figure 34 we observe that the density has not a clear shear but that it gradually decreases, making difficult to estimate the exact position of the center of the profile. It is clear, however, that a shift between the profiles exist and it is of the same order of the length of the density gradient, covering the full magnetopause thickness. The velocity shear instead is sharper of the order of $0.3\, d_i$ and in the boundary layer close to the magnetopause. From the fit we recover also information on the total velocity and density jump, being respectively $\triangle U/v_A = 0.76$ and $\triangle n/n_{msh} = 0.84$.

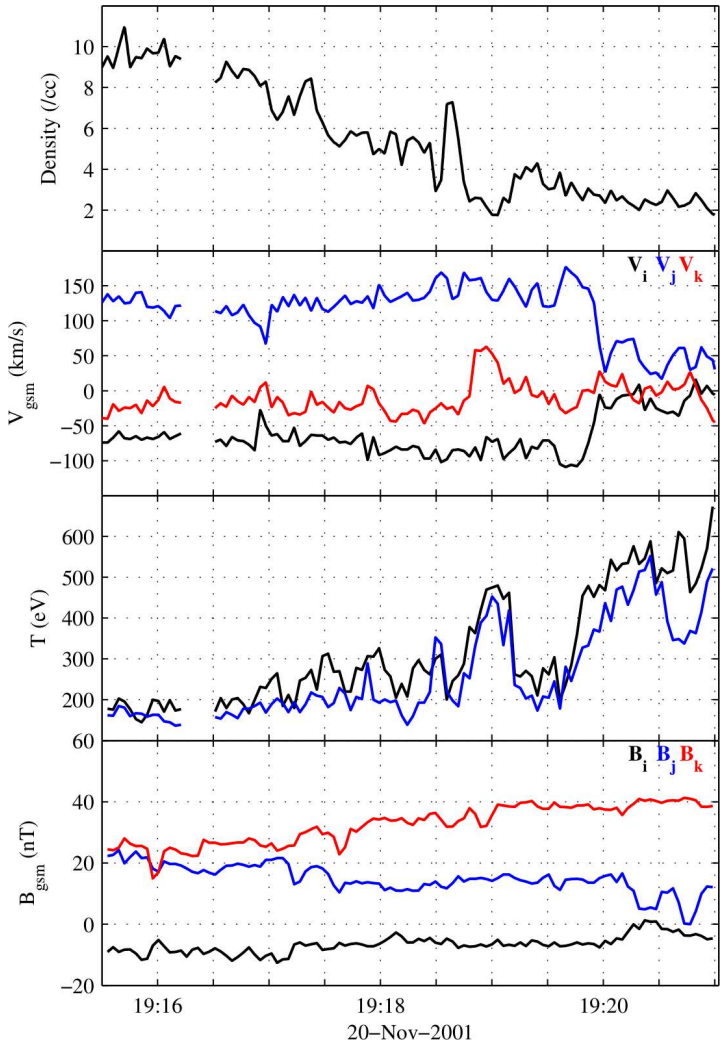

Figure 33: Zoom of the first of the crossing of Geotail, in the top panel the density, in the second panel the velocity in the GSM reference frame, in the third panel the parallel (in black) and perpendicular (in blue) temperature and in the fourth panel the three components of the magnetic field, B_i, B_j and B_k represented with black, blue and red lines respectively.

- Crossing 6, time interval Δt = [19:24:50-19:25:09] (UT)

Another significative crossing among those selected in figure 32 is the crossing 6, shown in figure 35. During this time interval the satellite is going from the magnetosphere/EBL to an almost magnetosheath plasma, the values of density reached after 19:25:00 (UT) are indeed comparable with those of the magnetosheath, see crossing of the magnetopause at 19:18:00 (UT) shown in the top panel in figure 33. During this crossing, as in crossing 1, the velocity shear is occurring after the density gradient as going from magnetosheath-like plasma to the inner region of the magnetopause. As before the velocity shear seem to occur simultaneously with the temperature variation while the mag-

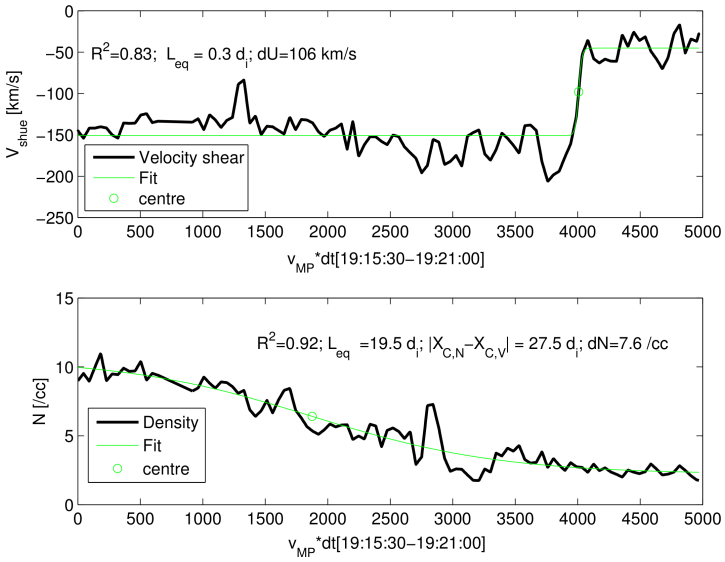

Figure 34: In the top panel the velocity and in the bottom panel the density profile as a function of the scale length, $\ell = v_{mp} \cdot \Delta t$, obtained multiplying the magnetopause velocity for the time interval of the selected crossing Δt = [19:15:30-19:21:00] (UT). Green lines are the fitted profiles and the green dot represents the centre of the estimated hyperbolic tangent. Inside each panel there are the information regarding the quality of the fit, R^2, shear lengths L_{eq} and the separation of the centres $|x_{c,n} - x_{c,U}|$.

netic field during this crossing stays almost constant. This crossing is probably covering from the inner boundary layer (the region closest to the magnetosphere in the inner side of the magnetopause) to the plasma depletion layer (the region just outside the magnetopause in the magnetosheath side). In figure 36 we show the same plot of figure 34 but for the crossing 6. The magnetopause velocity for this crossing is $v_{mp} = 26\,km/s$, for the time interval of the selected crossing, Δt = [19:24:50-19:25:09].

Both the fits are good despite the total velocity jump, see top panel of this figure, is underestimated using the fit. So we recover the total velocity jump by subtracting the maximum to the minimum value, obtaining $\triangle U/v_{A,msh} = 0.5$ and for the density $\triangle n/n_{msh} = 0.9$. The velocity and density shear lengths are comparable, their values are $L_{eq,U} = 0.5$ and $L_{eq,n} = 0.8$ respectively. The separation of the two profiles is $|x_{c,n} - x_{c,U}| = 1.3\,d_i$. Here the density gradient is sharper with respect to crossing 1, since probably this is not a full magnetosphere-magnetosheath crossing but the satellite is in the boundary layer. On the other hand the velocity shear length is comparable with the one estimated in crossing 1.

In table 3 we summarize the details of the above analized crossings including also two other cases inside the boundary layer, that are crossing 7 and 8 (not described above). In the table we report the

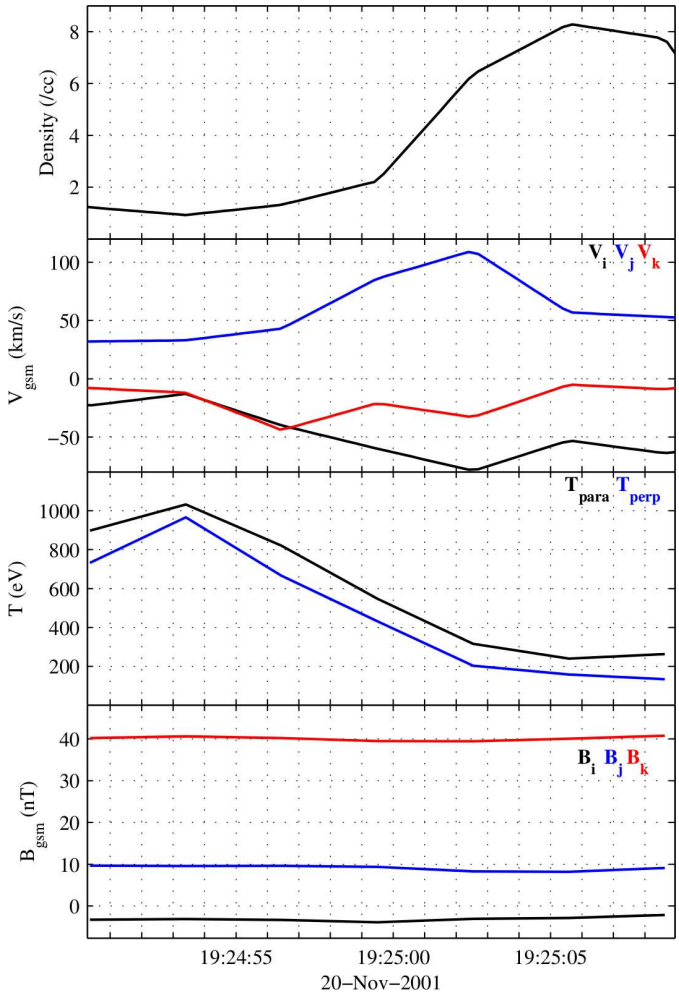

Figure 35: In the first panel the density is plotted as a function of the time interval of the crossing; in the second panel the three components of the velocity field in the GSM reference frame V_i, V_j and V_k represented in black, blue and red respectively; in the third panel the parallel temperature in black and the perpendicular temperature in blue and finally in the fourth panel the three components of the magnetic field (in GSM) B_i, B_j and B_k represented with black, blue and red continuous lines respectively. All the quantities are plotted versus the time interval of crossing 6.

values of the time interval $\triangle t$, the velocity shear length, $L_{eq,U}$, the total velocity jump normalized to the Alfvèn velocity in the magnetosheath $\triangle U/v_{A,msh}$, the density shear length $L_{eq,n}$, the total density jump $\triangle n/n_{msh}$ and the distance between the velocity and density centers, $x_{c,n} - x_{c,U}$, as going from the magnetosphere-like plasma to the magnetosheath plasma. In this table the first row refers to Cluster crossing and the last four rows to Geotail multiple crossings.

The difference between the centers of the profiles of density and velocity, $x_{c,n} - x_{c,U}$, is often of the same order of their shear lengths, except for the first crossing of Geotail, indicated as GT1. In this last

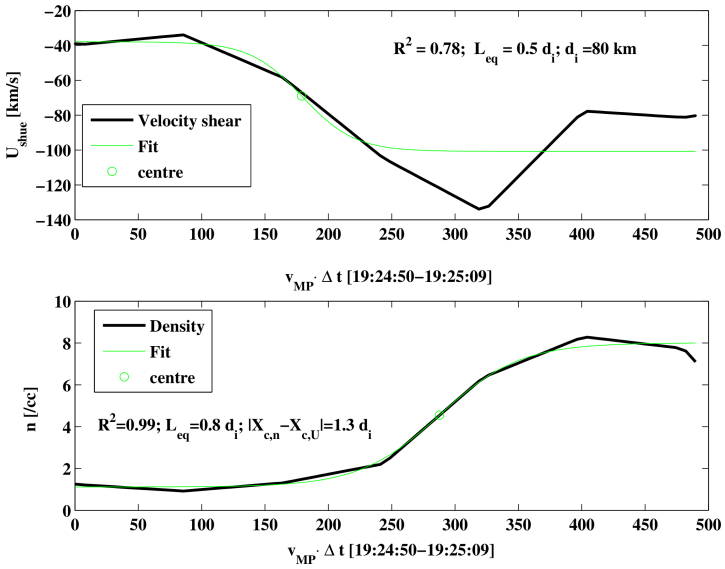

Figure 36: In this figure, in the top panel, there is the velocity in the Shue reference frame and, in the bottom panel, the density as a function of the scale length, $\ell = v_{mp} \cdot \Delta t$, obtained multiplying the magnetopause velocity, that for this case is $v_{mp} = 26\,km/s$, for the time interval of the selected crossing, Δt =[19:24:50-19:25:09]. In green the plot of the profiles obtained fitting the real profile with an hyperbolic tangent. The centres of these profiles are marked with a green dot. Inside each panel there are the information regarding the goodness of the fit, R^2, shear lengths L_{eq} and the separation of the centres $|x_{c,n} - x_{c,U}|$.

case indeed the crossing covers the full magnetopause thickness while the other cases are measuring variations in the boundary layers close to the magnetopause discontinuity. Considering all possible errors on the estimation of the velocity of the magnetopause influencing the scale length of the profiles, we can consider that Cluster crossing, GT6, GT7 and GT8 are of the same order, i.e. around one inertial length. It is a reasonable choice then to use, for the simulation, a density and velocity shear length of 1 d_i and a separation of the profiles of the same order, so $|x_{c,n} - x_{c,U}| = 1\ d_i = L_{eq,U} = L_{eq,n}$. As discussed before, the observed shift is not a consequence of the evolution of the instability since crossings are selected during the linear phase of the instability, i.e. when no vortices are detected. Indeed during its linear phase, the instability does not affect the initial plasma condition on which it develops, as confirmed by simulations. Neverthless, the experimental result suggested by the data is that the velocity and the density gradient are not occurring simultaneously. Observing all the selected crossings we note that the shift is not always occurring in the same direction, see the last column in table 3. For this reason we have decided to initialize the simulations with a shift between the centers of the density and velocity gradients given by $x_{c,n} \sim = x_{c,U} = \sim = 1, 0, +1\ d_i$,

CROSSING	$\triangle t$ (UT)	$l_{eq,u}$	$\frac{\Delta u}{v_{a,msh}}$	$l_{eq,n}$	$\frac{\Delta n}{n_{msh}}$	$msp \rightarrow msh$ $(x_{c,n} - x_{c,U})$
Cluster	[09:26:02-09:26:30]	1.6 d_i	0.3	0.24 d_i	0.9	$-1.7\ d_i$
GT 1	[19:15:30-19:21:00]	0.3 d_i	0.8	19.5 d_i	0.8	27.5 d_i
GT 6	[19:24:50-19:25:09]	0.5 d_i	0.5	0.8 d_i	0.9	1.3 d_i
GT 7	[19:34:00-19:35:30]	5 d_i	0.4	0.2 d_i	0.8	0.8 d_i
GT 8	[19:35:20-19:36:30]	0.5 d_i	0.3	0.3 d_i	0.8	$-0.3\ d_i$

Table 3: Parameters obtained from the fit with an hyperbolic tangent in the first row for the Cluster crossing (shown in figure 31) and for the seven multiple Geotail crossings selected in figure 32, shown in figure 31. Shear lengths for velocity ($L_{eq,U}$) and density ($L_{eq,n}$) and total jumps $\triangle n/n_{msh}$ and $\triangle U/v_{A,msh}$ are normalized to the density and Alfvèn velocity in magnetosheath.

so taking into account all possible configurations. The configuration $x_{c,n} \sim = x_{c,U} = \sim = 1\ d_i$ corresponds to the case measured by Cluster satellite on the flank of the magnetopause with the velocity shear on the outer side/magnetosheath boundary layer while the simulation initialized with $x_{c,n} \sim = x_{c,U} = +1\ d_i$ corresponds to the configuration detected by Geotail satellite near the nose.

As regards the velocity and density jump, a typical value among those obtained in all crossings has been chosen. For the velocity the total jump (normalized to the Alfvèn velocity in the magnetosheath) has a mean value of $\triangle U/v_{A,msh} = 0.4$, while the average total density jump is about $\triangle n/n_{msh} = 0.8$. For the sake of simplicity in order to study the role of the shift in the profiles, at the beginning the temperature is assumed as constant while the magnetic field profile is obtained by imposing total pressure equilibrium. Furthermore, in our numerical simulation for the sake of computational reasons, we have made a Galilean transformation of the velocity field such that the velocity varies from $\sim = \Delta U/2$ to $\Delta U/2$. Obviously, such velocity transformation does not affect at all the correctness of our numerical results.

5.4 SIMULATION USING EXPERIMENTAL INITIAL CONDITIONS

The initial large scale velocity and density profiles, obtained from data fit in section 5.3, are used to initialize the simulations. Their analytical form is expressed by the following equations:

$$\begin{cases} n = 1 - 0.5 \triangle n \{1 - \tanh[(x - x_{c,U} - x_c)/L_{eq,n}]\}; \\ U_y(x) = 0.5 \triangle U \tanh\left[(x - x_{c,U})/L_{eq,U}\right]); \\ T_i = 0.9 \\ T_e = 0.1 \end{cases} \tag{36}$$

where n is the density normalized to its value in the magnetosheath and U_y the velocity normalized to the Alfvèn velocity in the magnetosheath. The Alfvèn velocity in the magnetosheath, has been estimated during the selected crossings, and it is around $v_{A,msh} \sim 472\,km/s$ for Geotail crossings and about $v_{A,msh} \sim 236\,km/s$ for Cluster crossing. The temperatures values are taken from Cluster crossing since no electron moments are available for Geotail in this event. T_i and T_e are the ion and electron temperatures respectively, their values have been normalized to the total temperature in magnetosheath, i.e. $< T >_{msh} = < T_e >_{msh} + < T_i >_{msh} \sim 247\ eV$ where $< T_e >_{msh} \sim 26\ eV$ and $< T_i >_{msh} \sim 221\ eV$. The normalized values are obtained as $T_{e,i} = < T_{e,i} >_{msh} / < T >_{msh}$. The center of the velocity profile is chosen in the middle of the simulation box $x_{c,U} = L_y/2$ while the center of the density profile is determined by the value of x_c, a parameter that we change in our simulations. The total density and velocity jump are $\triangle n = 0.8$ and $\triangle U = 0.4$. Magnetic field is mostly out of plane with a small component in the flow direction:

$$\mathbf{B} = [0, B_0 sin(\vartheta), B_0 cos(\vartheta)] \tag{37}$$

with $\vartheta = 0.02$ rad and $B_0 = 1.0$.

We discuss now three simulations varying the center of the gradient of the density profile with respect to that of the velocity. As discussed in the previous section, this is achieved by using different values for x_C in Eq. 36, namely $x_C = 0, -1, 1\,d_i$. The value, $x_C = 0$ is taken as a reference case because most of the previous numerical simulations in in the literature of these last years use this choice, Ref. Cowee et al. [19], Faganello et al. [30, 31, 33], Henri et al. [56], Huba [60], Miura [76], Nakamura and Fujimoto [79], Nakamura et al. [81], Otto and Fairfield [86], Palermo et al. [87], Takagi et al. [115], Tenerani et al. [116], Thomas and Winske [118]. The last two values correspond to different set of observations that, when going from the magnetosheath to the magnetosphere, observe the density gradient either before or after the velocity shear, see last column of table 3. We define these three reference cases as the centered, left-shifted and right-shifted case (Cc, Lsc, Rsc), respectively. We use a simulation box with a numerical domain given by $L_x \times L_y = (200\,d_i) \times (30\,\pi\,d_i)$ and a resolution $dx \times dy = 0.19\ d_i \times 0.18\ d_i$, corresponding to $N_x \times N_y = 1024 \times 512$ points.

5.4.0.2 *Result of the simulations*

In figure 37 we show the passive tracer for the three simulations, Cc, LSc, RSc, in the first, second and third row respectively. In particular we plot the tracer at the beginning of the non linear phase, $t = 500\,\Omega_{ci}^{-1}$ (first column) and at the end of the simulation, $t = 800\,\Omega_{ci}^{-1}$

(second column). The passive tracer is a scalar quantity, *Tr*, advected by the flow and obtained by integrating the following equation:

$$\frac{dTr}{dt} = \left[\frac{\partial}{\partial t} + U \cdot \nabla\right] Tr \tag{38}$$

We observe a similar dynamics of the system during the initial evolution of the Lsc, Cc and Rsc cases. This is shown in figure 37, where we draw the shaded iso-contours of the passive tracers at the end of the linear phase, left column and in the advanced non linear phase after vortex pairing has took place, right column.In all cases we observe the formation of a vortex chain made by four main vortices corresponding to the fast growing mode (FGM) of the system, namely $m = 4$.

In the right column, we observe that all simulations result in a single final vortex configuration due to the efficiency of the vortex pairing mechanism.

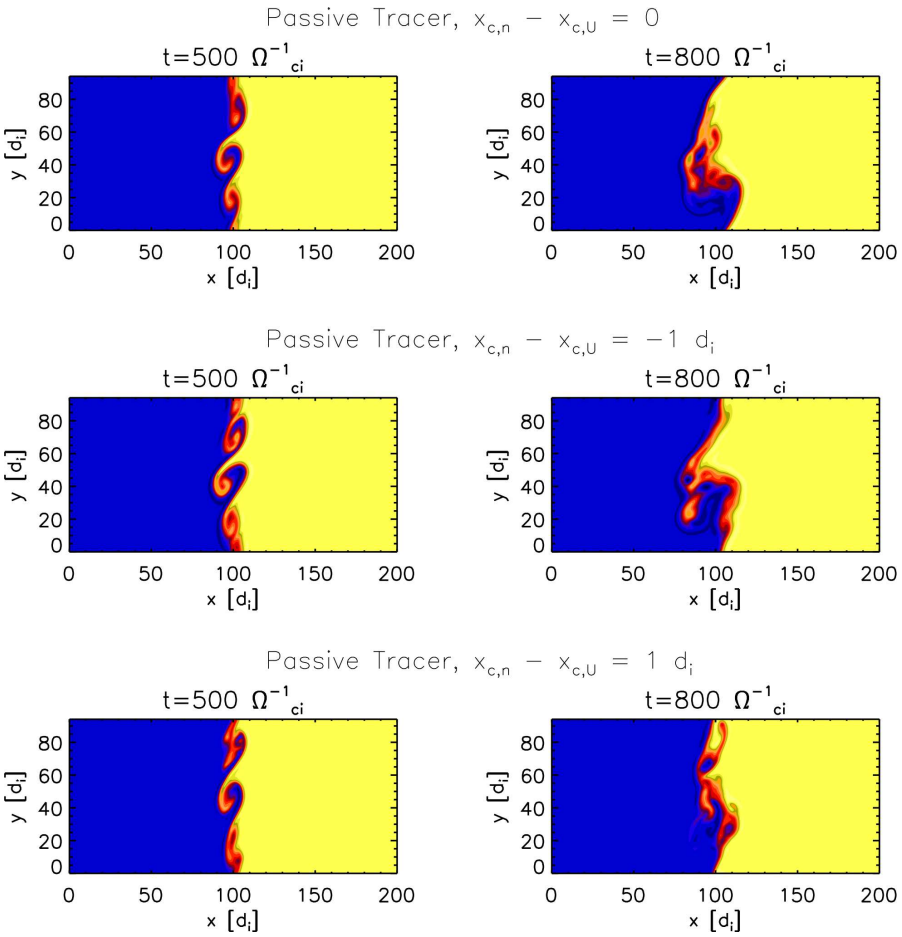

Figure 37: Time evolution of the passive tracer for the initially centred case (first row), left shifted case (second row) and right shifted simulation (third row) for two different time of the simulation. In the first column the tracer at $t = 500\,\Omega_{ci}^{-1}$ in the beginning of the non linear phase and in the second column at the end of the simulation, $t = 800\,\Omega_{ci}^{-1}$.

The evolution of the modes of the x-component of the velocity field has been analysed by doing a Fourier transformation along y and by taking a mean in the x-direction, $< |U_{ix}(m,\ t)| >_x$, for different time steps of the simulation. The time evolution of the amplitudes of these modes is shown in figure 38 during the linear phase of the instability. In this figure we present the results of the simulation initialized with centred density and velocity profiles (Cc). In agreement with the formation of four vortices as shown by the passive tracer in figure38, we do observe that the amplitude of the fourth mode is the largest one.

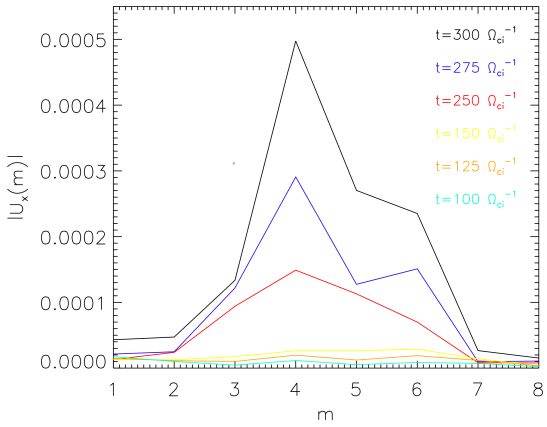

Figure 38: Time evolution of the amplitudes of the unstable modes of the $< |U_{ix}(m,\ t)| >_x$during the linear phase, from $t = 150\ \Omega_{ci}^{-1}$ to $t = 300\ \Omega_{ci}^{-1}$

Following, Ref. Miura and Pritchett [78], in figure 39 we plot the growth rate γ normalized to the velocity shear length $L_U = 1\ d_i$ and the total velocity jump $U_0 = 0.4$ as a function of the normalized wavelength $2k_y L_U$ for the three simulations LSc, Cc and RSc, plotted using red, black and blue lines, respectively.

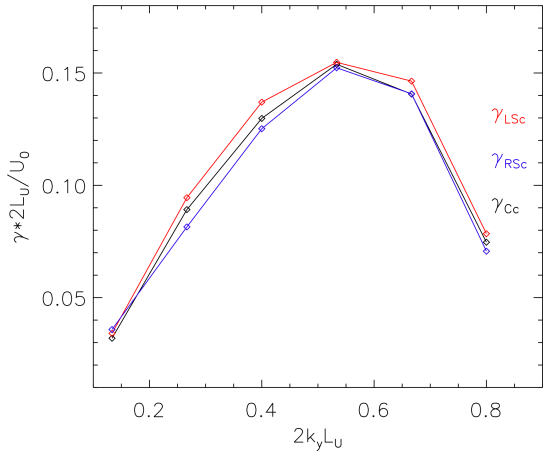

Figure 39: Normalized growth rate $\gamma 2L_U/U_0$ as function of the normalized wave number $2k_y L_U$. In black for the Cc, in blue for the RSc and in red for the LSc.

Lsc case has the largest growth rate since it corresponds to the case where the vortices are generated in an almost constant density plasma with the largest value of the density. As expected, the highest growth rates occur for the LSc and the peak, corresponding to the fastest growing mode, occurs between $0.5 \lesssim 2k_{y,\,FGM}L_U \lesssim 0.7$ both for the LSc and Rsc case. Let us consider the Cc, the highest value of γ occurs at about $2k_{y,\,FGM}L_U \sim 0.53$, so $k_{y,\,FGM} \sim 0.27/L_U$ and the wavelength of the FGM is:

$$\lambda_{FGM} \sim \frac{2\pi}{k_{y,\,FGM}} \sim 23.7\ L_U$$

The mode corresponding to the FGM, Ref. Miura and Pritchett [78] is:

$$m = \frac{L_y}{\lambda_{FGM}} = \frac{30\pi}{23.7} \sim 4$$

Indeed in our simulation we recover m=4 is the dominant mode, corresponding to the development of four vortices. In figure 40 we plot, in the first row, the growth rates of the most unstable modes (the first five) for the U_x component of the velocity field by making a Fourier transformation along y and by taking an average in the x-direction. In the second row, we plot the distance between the centers of the density and velocity profiles, i.e. $|x_{c,n}(t) \sim = x_{c,U}(t)|$, where $x_{c,n}(t)$ and $x_{c,U}(t)$ indicate the centers of the density and velocity profiles respectively, at each time step, used to initialize our simulations. In the third row we plot in black the density shear length, $L_{eq,n}$, and in red the velocity shear length, $L_{eq,U}$. The values of the centers $x_{c,n}(t)$, $x_{c,U}(t)$ and of the velocity and density shear lengths, $L_{eq,U}$ and $L_{eq,n}$, are obtained by fitting at a given time the velocity and density profiles, averaged over the y-direction, with an hyperbolic function. In this figure the first column refers to the Cc, the second column to the LSc and the third column to the RSc simulation.

Looking at the first row we see that in all cases, after the initial phase where the FGM $m = 4$ dominates, the inverse cascade (i.e. vortex pairing) takes place eventually leading to the $m = 1$ mode that emerges over the others. Indeed, as discussed before, the final stage of these three simulations is similar, characterized by a single vortex configuration and this is confirmed here observing that the $m = 1$ mode dominates over the others in the saturated stage, approximately from $t = 500\,\Omega_{ci}^{-1}$ onwards. The growth rates for the fast growing mode (FGM) are shown in the panel below:

CENTRED	LEFT-SHIFTED	RIGHT-SHIFTED
$\gamma_{m=4} = 0.031$	$\gamma_{m=4} = 0.032$	$\gamma_{m=4} = 0.029$

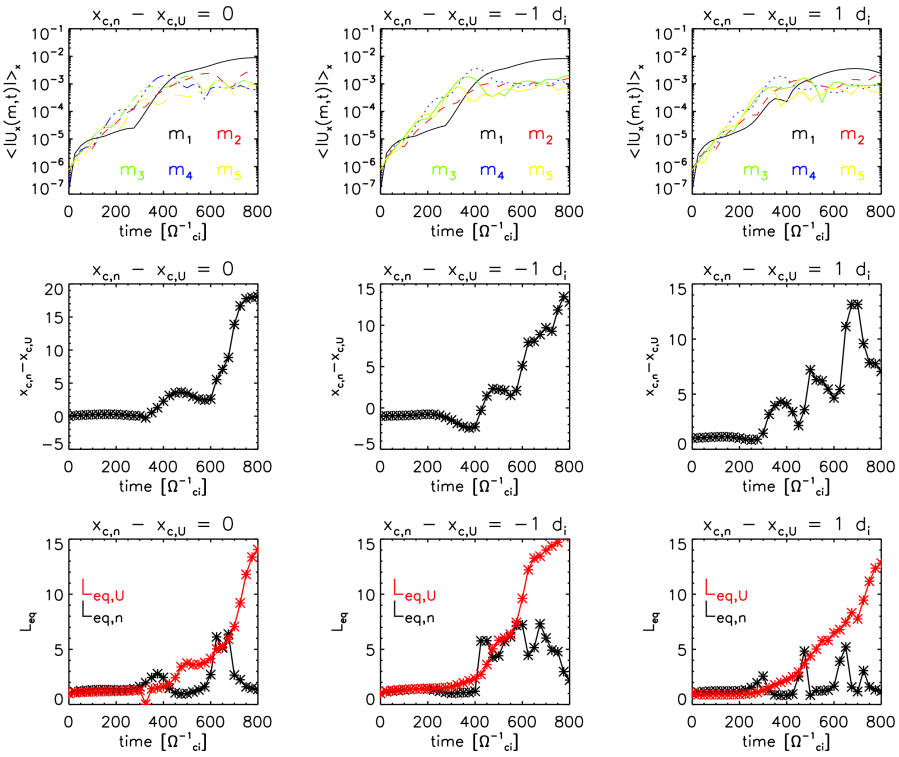

Figure 40: In the first row there are the growth rates for the first five modes respectively in black, red, green, blue and yellow lines; in the second row it is shown the evolution of the distances between the centers of n and U in time and in the third row the evolution of the shear lengths during the simulation time. From left to right column these quantities are plotted for the Cc, LSc and RSc.

Despite of the fact that we observe that in the LSc the growth rate is slightly higher compared to the other two, we cannot conclude that there is a significant difference in the three cases. The observed shift between the centers of the velocity and density profiles it is not a consequence of the K-H instability. The selected satellites crossings are taken during the very initial phase of the instability, the linear phase. During this phase the initial plasma conditions are not modified. This aspect is clearly shown in the second and third row of figure 40 where we plot the distance of the centers $|x_{c,n} \sim = x_{c,U}|$ and the shear lengths $L_{eq,U}$ and $L_{eq,n}$, respectively. We observe, as it should, that doing a cut at $y = L_y/2$ these quantities do not change at all during the linear phase, until $t = 300\,\Omega_{ci}^{-1}$ for the initially centered case and up to $t = 200\,\Omega_{ci}^{-1}$ for the initially shifted cases. In other words, these quantities stay constant all along the linear growth of the instability. In the non-linear phase, instead the distance between the initial position of the velocity and density increases as well as their shear lenghts. There are various mechanism acting in this phase like the motion of the vortices that start to roll up and interact with each other.

5.5 SIMULATIONS WITH HIGHER VELOCITY JUMP

The ion moments are measured by the Low Energy Particle (LEP) experiment onboard of Geotail, possibly counts are saturated in the magnetosheath resulting in an underestimation of the density during this event.

The consequences of this underestimation affects also the Alfvèn velocity (that depends on the density) used to normalize the total velocity jump. The total density jump recovered from the data is:

$$\frac{\Delta n}{n_{msh}} = \frac{n_{msh} - n_{msp}}{n_{msh}} = 1 - \frac{n_{msp}}{n_{msh}} = 0.8$$

By considering the density in the magnetosheath underestimated by a factor 2, for example, we get:

$$\left(\frac{\Delta n}{n_{msh}}\right)_{corrected} = 1 - \frac{1}{2}\frac{n_{msp}}{n_{msh}} = 0.9$$

The total velocity jump, obtained from the data is:

$$\frac{\Delta U}{v_{A,msh}} = \frac{U_{msh} - U_{msp}}{v_{A,msh}} = 0.4$$

Taking into account the possible underestimation of the density we correct the Alfvèn velocity and of the magnetosheath velocity:

$$\left(\frac{\Delta U}{v_{A,msh}}\right)_{corrected} = \frac{2U_{msh} - U_{msp}}{v_{A,msh}/\sqrt{2}} = 0.8$$

This indicates that higher density and velocity shear are most realistic initial conditions for the simulations. For technical and time reasons we could not ran simulations with many different values of density jump and velocity shear.

Therefore, we have taken one simulation among those already available, that has an higher velocity jump, $\triangle U/v_{A,msh} = 1$, and with an almost similar value of the total density jump to the previous set of simulations, $\triangle n/n_{msh} = 0.7$. Additionaly we have run such a simulation with such jumps shifted profiles. In summary we have two simulations, with and without the initial density shift, corresponding in equation 36 to a value of the center of the density shear equal to $x_C = 1, 0$ respectively. In this case we just consider these two configurations and not the LSc, because we are interested on the effect of the profile shift on the dynamics, so that we just consider one of the two shifted configurations with respect to the centered case. As before, we indicate as "centered-case" (Cc) the simulation with $x_C = 0$ and as "Right shifted-case" (RSc) the simulation with $x_C = 1$. The simulation box, used for these last two simulations is $L_x \times L_y = (120\, d_i) \times (20\, d_i \times 2 \times \pi)$, with a resolution

$dx \times dy = 0.1 \times 0.06$. We plan, in future, to perform additional runs with higher density and velocity jumps, and shifted profiles to investigate carefully how the K-H instability depends on such parameters.

5.5.0.3 *Result of the simulations*

In figure 41 we plot, in the first column, the iso-contours of the passive tracer in the non linear phase of the primary K-H instability for the Cc at $t = 175\,\Omega_{ci}^{-1}$ (top panel) and for the Sc at $t = 200\,\Omega_{ci}^{-1}$ (bottom panel). In the central column we plot the same quantity during the saturated phase of the K-H instability for the Cc at $t = 400\,\Omega_{ci}^{-1}$ (top panel) and for the RSc at $t = 600\,\Omega_{ci}^{-1}$ (bottom panel). The right column shows the time evolution of the most unstable modes for the Cc (top panel) and for the Sc (bottom panel).

In these simulations we observe a clear difference between the Cc and the RSc. First, observing the vortices in the non linear phase we note that in the Cc, secondary instabilities take place on the arms of the vortices, see top-left panel. Indeed since the velocity shear is located in the same region as the density shear, strong density gradients are carried on along the vortex arms. As a result, the final stage of the simulation is characterised by a fully developed "mixing layer" where the K-H vortices are completely destroyed, see central-top panel in figure 41. The lack of a dominant vortex structure in the system at the end of the Cc simulation is confirmed by the time evolution of the unstable modes, shown in the top right panel, where the final stage of the non-linear regime, $t > 300\,\Omega_{ci}^{-1}$, is characterised by several modes reaching comparable amplitudes. On the other hand, in the RSc, the velocity shear occurs in a region of more or less homogeneous density, so that the vortex arms are now of almost equal density; therefore, secondary instabilities are much less efficient and the vortices appear as very coherent, in particular if compared to the Cc. In this case, the non-linear evolution of the K-HI is dominated mainly by vortex pairing, leading to a large one vortex final configuration. The bottom-right panel indeed confirms that the mode $m = 1$ is largely dominant with respect to the others. The above results tell us that when the velocity and density profiles are centred, one should observe the formation of a turbulent layer driven by the development of secondary instabilities; instead, when the two fields are shifted one with respect to the other, the pairing mechanism dominates and one should observe large-scale vortices. A different dynamic is recovered just when the velocity jump is sufficiently high. Indeed, for the simulations initialized with the parameters obtained from the satellite data fits, i.e. using a density jump $\triangle n/n_{msh} = 0.8$ but a smaller velocity jump $\triangle U/v_{A,msh} = 0.4$, the velocity jump is much less efficient in destabilising the vortices by secondary instabilities even when the two gradients of the velocity and density profiles are centered. The first conclusion is that the shift between the two profiles is a very

important ingredient only in the presence of a relatively strong flow. Indeed, with a larger velocity jump, the shift is a very important element in the simulations, since when a shift is included results are coherent with the data observed by satellites.

5.6 COMPARISON WITH OBSERVATIONAL RESULTS

The event 2001-11-20 has been studied in 2004 when for the first time K-H vortices have been detected in low latitude magnetopause using four satellites measurements, see Ref. Hasegawa et al. [50]. Fluctuations observed at the dayside during the same event but earlier in time by Geotail have been considered as the initial seed of the vortices observed later on along the flanks by Ref. Hasegawa et al. [53]. Neverthless, these perturbations may be unrelated to the Cluster observations and the waves measured at low latitude by Cluster can instead origin in a region along the flank, see Ref. Foullon et al. [37, 38, 39]. Using Roelof and Sibeck [97] and Shue et al. [107] magnetopause models, the thickness of the inner boundary layer during Geotail crossing has been estimated to be $(1206 \pm 695)\,km$, Ref. Foullon et al. [37], corresponding to about $(12 \pm 7)\,d_i$ (using here as a realistic value for the ion inertial length $d_i \sim 100\,km$). The velocity shear layer at the dayside has been also estimated in Ref. Hasegawa et al. [53], where the authors used a method for the reconstruction of the velocity field developed by Ref. Sonnerup et al. [111]. They obtained a full width of the velocity shear of $1000\,km$ corresponding to $L_{eq} = 500\,km \sim 5\,d_i$. The estimation of the velocity shear length we made is smaller, around one inertial length, this is possibly depending on the fact that some of our crossings are not complete, i.e. going from the magnetosphere to the magnetosheath region but instead are covering a region near the magnetopause, between the magnetosheath boundary layer and the inner boundary layer. Also we need to consider, that our estimation of the width of the shear layer is affected by the possible uncertainities in the estimation of the magnetopause velocity, see section 5.3, so the actual width could be different. A different width of the shear layer affect the propagation time of the vortices. A total velocity width of $1000\,km$ corresponds to a wavelength for the most unstable mode of about $8000\,km$, see Ref. Miura and Pritchett [78] where the linear analysis of the K-H instability has been performed on a sheared finite thickness flow in opposition to the single magnetopause boundary used in previous models.

From the simulations it is possible to estimate the growth time of the vortices and compare this time with the satellites observations. In table 4 we report the time needed for the vortices to develop for the centred and right shifted cases, comparing the simulations initialized with two different initial velocity jumps, i.e. $dU/v_A = 0.4$ and $dU/v_A = 1$.

Case $dU/v_A = 0.4$,Vortices Growth time

CENTRED	RIGHT-SHIFTED	TIME DIFFERENCE IN %
$t = 325\,\Omega_{ci}^{-1} = 18$ minutes	$t = 300\,\Omega_{ci}^{-1} = 17$ minutes	5%

Case $dU/v_A = 1$, Vortices Growth time

CENTRED	RIGHT-SHIFTED	TIME DIFFERENCE IN %
$t = 100\,\Omega_{ci}^{-1} = 5$ minutes	$t = 150\,\Omega_{ci}^{-1} = 8$ minutes	60%

Table 4: Growth times for the simulations initialized with a total velocity jump of $dU/v_A = 0.4$ in the first row and $dU/v_A = 1$ in the second row. The first column refers to simulations with initially centred profiles of density and velocity, the second column to simulations initialized with the density profile shifted on the right with respect to the velocity profile of one inertial length and in the third column the time difference in percentage between the shifted and centred simulations is reported.

Using the measured value of $\Omega_{ci} = 0.3$ Hz in the magnetosheath, we obtain that for the simulations initialized with a total velocity jump of the time needed to form full roll-up vortices is comparable among the two cases, being around 17, 18 minutes, with a difference of the 10% between these values. A larger difference is instead obtained in the simulations with an initial total velocity jump of $\Delta U/v_A = 1$. Indeed in this case the presence of an initial shift between the velocity and density profiles centers strongly affects the evolution of the instability as pointed outin figure 41.

Let us now consider the simulations initialized with $\Delta U/v_A = 0.4$, a value recovered from the observations of Geotail and Cluster, we can estimate the phase speed in this case. Since vortices are not propagating in our simulations, the phase speed is given by half the velocity jump, $v_\phi \sim \Delta U/2 = 0.2\,v_A$. Taking into account the two different Alfvèn velocities measured by Geotail and Cluster, we can estimate a phase speed at Geotail of $v_\phi \sim \Delta U/2 = 0.2\,v_A = 94.4\,km/s$, using $v_{A,GT} \sim 472\,km/s$ and a phase speed at Cluster of about $v_\phi \sim \Delta U/2 = 0.2\,v_A = 47.2\,km/s$, using the calculated $v_{A,CLUSTER} \sim 236\,km/s$. Taking a mean value between the two, we obtain $\overline{v}_\phi \sim 70.8\,km/s$. If vortices origin at the nose, then we could estimate the time needed for the K-H wave to travel from Geotail to Cluster position, considering a distance between Geotail and Cluster of $15\,R_E$, Ref. Hasegawa et al. [53]. The estimated time would be around 22 minutes, corresponding to $t = 400\,\Omega_{ci}^{-1}$. The phase speed during this event has been also estimated in Ref. Foullon et al. [37, 39], where it has been calculated using four-spacecraft timing, obtaining an average value around $\overline{v}_\phi \sim 64\,km/s$, considering a mean value between the one estimated at Geotail of $v_\phi \sim 50\,km/s$ and at Cluster of $v_\phi \sim 85\,km/s$. Using this value, than it would take around 25 minutes for the in-

stability to travel from the nose to the magnetopause flank comparable with our results. A larger phase speed instead is obtained in Ref. Hasegawa et al. [53], where a mean wave phase speed of $\sim 150\,km/s$ is obtained taking intermediate value between the values of the phase speed estimated at Cluster, that is $v_\phi = 211\,km/s$ and at Geotail, $v_\phi = 115\,km/s$ (using ion velocity measurements). In this case the time needed for the instability to travel from the nose to Cluster position, is about 11 minutes. Given the total thickness of the shear layer that they estimated to be $1000\,km$, a velocity jump $200\,km/s$ and the initial wavelength of the dominant K-H mode, in the simulations, Ref. Takagi et al. [115], the dominant mode would take about 10 minutes to develop rolled-up vortices, being a comparable time with their estimation. In our simulations initialized with $\Delta U/v_A = 0.4$ we found instead that the time for vortices to form is around 18 minutes, closer to the estimations of Ref. Foullon et al. [37].

Since we do not have information about the degree of development of the vortices detected by the satellites that we should consider for the comparison with simulations, we analyse the simulation at the time predicted for the vortices to propagate from the nose to the tail, i.e. around 10 minutes using the phase speed estimated by Ref. Hasegawa et al. [53], and 22 minutes as estimated from our simulations and in agreement with speeds derived by Ref. Foullon et al. [37]. For the simulations initialized with $\Delta U/v_A = 0.4$ vortices structures in the simulation begin to form after 10 minutes ($t = 180\,\Omega_{ci}^{-1}$) as we can observe in table 4. On the other hand vortices structures are observed around 22/25 minutes, corresponding to $t = 450\,\Omega_{ci}^{-1}$.

In the simulations with a higher initial velocity jump, instead, the time needed to develop vortices is, for shifted case, $t \sim 8$ minutes and for the centred case $t \sim 5$ minutes, the difference is of the 60%. In this case only when an initial shift between the density and the velocity profiles is imposed at the beginning, the time needed to form roll-up vortices is comparable to the time estimated by Ref. Hasegawa et al. [53], 10 minutes, and vortex-like structures are still present at $t \sim 20$ minutes. In the simulation initialized with centred profiles, instead at around 10 minutes corresponding to $t = 180\,\Omega_{ci}^{-1}$, vortices are already in the saturated phase and no vortex structure is preserved. To summarize the results of the simulations we can say that qualitatively with shifted profiles the dynamic is slower, more stable, yet we need to run a parametric study to be more quantitative.

5.7 DISCUSSION AND CONCLUSIONS

Kelvin-Helmholtz instability is an important mechanism for solar wind plasma transport in the magnetosphere. Past simulations have demonstrated that the dynamics inside the vortices depends strongly on the plasma initial condition, since phenomena like reconnection or

secondary instabilities can take place differently according to the initial large scale fields. The velocity profile has certainly a fundamental role on the evolution of this instability since the K-H modes depend on the characteristic scale of variation of the instability, $L_{eq,U}$, see Ref. Miura and Pritchett [78], and they grow proportionally to the total velocity jump, $\triangle U$. Moreover, the strength of the initial velocity field also influences the evolution in the non-linear phase, after vortices are formed. As presented in section 1.6, also an initial magnetic field in the flow direction can strongly affect the evolution of the instability, either by suppressing the primary instability itself or by changing the long time, non-linear evolution of the system, for example by inhibiting the development of secondary instabilities. The competition between the secondary instabilities and the pairing mechanism is also influenced by, for example, the presence of a sufficiently high density jump that drives the development of secondary Rayleigh-Taylor instabilities, causing then vortex disruption before pairing acts, leading the system into a mixed turbulent layer. The evolution and the final dynamics of the K-H instability can be reproduced the closest to reality using simulations with initial condition as close as possible to the observed configuration. This point has mainly motivated the research of the observational profiles of the principal physical quantities across the magnetopause during events favorable for K-H instability to be used as initial condition in our simulations.

We consider one event in particular, during the day 2001-11-20, in which we have at the same time the crossing of Geotail at the dayside magnetopause and two crossings of Cluster at the dusk flank, one before K-H develops and one after. By analysing all crossings before vortices formation, we found, as a common feature, that the velocity and density shear profiles during this event have the centers of the gradients shifted one with respect to the other .

Such shift is of the same order as the characteristic length of the density and velocity gradient, which turns out to be about one inertial length. This value is different with respect to the boundary layer thickness as estimated in Ref. Foullon et al. [37], Hasegawa et al. [53] but in a region close to the magnetopause between the magnetosheath boundary layer and to the EBL/outer boundary layer.

The presence of a shift between the two profiles, not always occurring on the same side, is a very important result since it changes the conditions for vortex formation. In the presence of a shift, indeed, the vortices do form in a region of almost constant density leading to more robust structures with respect to secondary instabilities. Considering this, simulations have been initialised in three different ways, taking the density and velocity large scale fields superposed (as usually done in the literature on this topic), shifted with the density shear displaced on the left and on the right by one inertial length with respect to the velocity shear. Using the observed values for the velocity

and density jumps, i.e. $\Delta U/v_A = 0.4$ and $\Delta n/n_{msh} = 0.8$, we have obtained that in all cases the vortex pairing is the dominant mechanism. Time needed for the vortices to full roll-up is comparable for the three simulations, around 20 minutes. Considering the typical values used in the past literature and a possible underestimation of the total velocity and density jumps in Geotail measurements, we consider other simulations, initialized with a total velocity and density jump of $\Delta U/v_A = 1$ and $\Delta n/n_{msh} = 0.7$ and taking the density and velocity profiles superposed or shifted. For the simulations with an higher velocity jump, the vortex structures are destroyed in the simulation with centred profiles because of the development of secondary instabilities. Initially shifted profiles cause instead a much slower evolution of the secondary instabilities, giving time for the vortices to pair and to form a final single vortex structure. The time needed for the formation of the vortices is comparable with the time estimated for the instability to travel from the nose to the flanks of the magnetopause only for the simulation initialized with shifted profiles. Either using the velocity jump obtained from the fit, $\Delta U/v_A = 0.4$, or an higher velocity jump but with shifted density and velocity profiles we have results comparable with observations.

In the next future we plan to include realistic profiles of temperature and magnetic field to investigate also their role in the K-H formation and development. As regards the shift between density and velocity field, further investigation are necessary to understand the mechanisms responsible for it and a larger statistic of events is needed to generalize also this result.

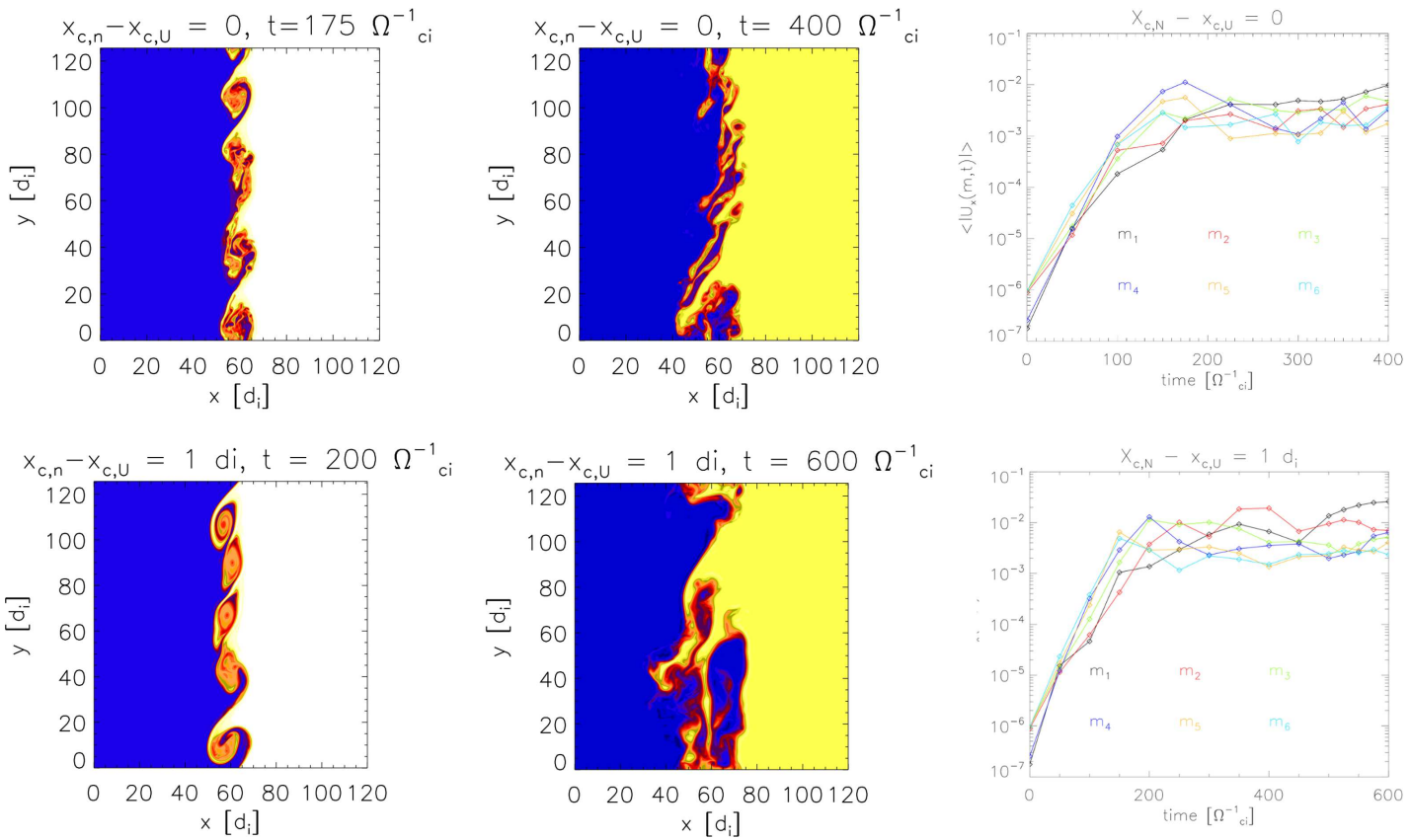

Figure 41: The first row refers to the simulation initialized with centred profiles of density and velocity. In the top panel on the left the iso-contours of the passive tracer at the non linear hase of the instability, $t = 175\,\Omega_{ci}^{-1}$, in the top central panel the same quantity is plotted in the saturated phase of the instability, i.e $t = 400\,\Omega_{ci}^{-1}$. In the top panel on the right the first six unstable modes for the mean of the x component of the velocity field, $< U_{i,x}(m,t) >_x$. The second row refers to the simulation initialized using a density profile shifted with respect to the velocity one of $|x_{c,n} - x_{c,U}| = 1\,d_i$, where $x_{c,n}$ is the centre of the density profile and $x_{c,U}$ is the centre of the velocity shear. In the bottom panel on the left, the iso-contours of the passive tracer in the non linear phase of the instability, $t = 200\,\Omega_{ci}^{-1}$ and in the bottom central panel the tracer in the saturated phase of the instability, $t = 600\,\Omega_{ci}^{-1}$. In the bottom right panel, the time evolution of the first six unstable modes.

Part IV

CONCLUSIONS AND OUTLOOK

CONCLUSION AND PERSPECTIVE

The interaction between the solar wind and the Earth's magnetosphere is one of the most important problems in the Space Weather contest and in Astrophysics in general. This interaction is mediated by many processes occurring at the magnetopause, the boundary region that separates the two different plasma regions. Among these processes, the Kelvin-Helmholtz (K-H) instability plays a fundamental role in the contest of solar wind (SW) plasma transport in the Earth's magnetosphere. The work of this thesis intends to contribute to the understanding of the role of the Kelvin-Helmholtz instability as a main driver of the dynamics occurring at the magnetopause. This instability originates from the velocity shear occurring between the solar wind and the magnetosphere and it has been detected by satellites observations having in-situ measured typical structures consistent with K-H vortices, Ref. Fairfield et al. [34], Hasegawa et al. [50]. Once vortices are formed, in the non-linear phase, they can either interact with each other, merging and forming larger vortices or developing secondary instabilities along the arms of the vortices. In this last case, the evolution of secondary instabilities cause vortices disruption and lead to the formation of a mixing layer characterized by small scale structures eventually leading to a full turbulent state.

Numerical simulations have demonstrated that the evolution and final configuration of the K-H instability strongly depends on the initial system conditions. Indeed, the strength of the initial velocity field, the presence of a density gradient, the strength of the magnetic field along the flow direction define the so-called initial conditions determining the evolution in the linear and non-linear phase of the instability. Motivated by these aspects, in this thesis we focus on two main topics:

- Work 1: Analysing the turbulence that spontaneously develops, in the long time evolution, inside the Kelvin-Helmholtz vortices and characterizing the dynamics occurring at small scales;
- Work 2: Investigating the plasma conditions across the magnetopause during events favorable for the Kelvin-Helmholtz instability to develop and how the realistic initial conditions affect the simulations.

These objectives have been pursued by combining, on one side, the numerical approach based on the Two-Fluid code developed at the Department of Physics of the University of Pise and on the other side, the satellite in situ measurements analysis of the magnetopause, using ACE, Geotail and Cluster satellites.

Turbulence induced by the Kelvin-Helmholtz instability

As briefly mentioned above, the solar wind plasma transport into the Earth's magnetosphere is a fundamental problem in plasma physics. The evolution of K-H vortices often leads to a final stage where a turbulent pattern full of small scale structures is recovered, this turbulent mixing layer is helping in turn the solar wind plasma transport. It is important then to identify the microphysical mechanisms responsible for plasma transport and to characterize such a rich dynamics. In particular, in this thesis we have investigated the turbulent properties of this system by the use of 2D two fluid numerical simulations. The saturated turbulent phase of the instability has been studied. We have started by looking at the distribution of the spectral energy of the magnetic field fluctuations in the (k_x, k_y) wave-vector space. As expected, initially there is a strong anisotropy in the energy distribution due to the presence of a velocity shear imposed in one direction as well as to the fact that the vortices are not circled shaped. As the simulation evolves, the vortices are destroyed and an almost isotropic configuration is reached. In this phase, we calculate the magnetic field spectrum by integrating the spectral magnetic energy over concentric shells. A power law spectrum is obtained and a slope of $k_\perp^{-8/3}$ is recovered at ion scales, consistentely with the results of previous kinetic simulations, Ref. Wan et al. [130]. The power distribution functions (PDFs) of the magnetic field increments, calculated at different scales, show the presence of tails with respect to a Gaussian distribution. Tails are due to intense magnetic field increments, typically linked to the presence of coherent structures. Tails increase as going towards smaller scales and this is a signature of intermittency. The steering away from a Gaussian distribution is quantified by the flatness (the fourth order moment of the increments). As expected, we have observed an increase of the flatness going towards smaller and smaller scales. Turbulence has been analysed using a statistical approach. Furthermore, we have identified the structures responsible for the observed intermittency. In particular by making different cuts in the turbulent region, we have calculated the number of structures with the "larger" current intensity $|J_z|/\sigma$, corresponding to the presence of intense magnetic fluctuations. We have also calculated the Partial Variance of Increments (PVI) for each of the cuts in order to identify the most intense fluctuations. Increments are calculated for various length scales, going from half of the box size to about one inertial length, letting us to identify the scale size of the most intense fluctuations responsible for the tails observed in the PDFs. By analysing in detail each structure, we have observed that most of them correspond to reconnection regions. Magnetic reconnection has been investigated by looking how different quantities behave as crossing a single structure in analogy to the kind of study typically performed when dealing with experimental satellite data. Typical features of asymmet-

ric reconnection have been recovered for one particular structure. We note that this kind of analysis is usually not performed in a turbulent pattern because of the difficulties to study each reconnection structure without the influence of the surrounding turbulent system. The typical features of a magnetic reconnection event are often hard to recover because reconnection here it is not-set up by starting from a schematic Harris-type configuration, but it arises in full turbulent configuration. However, a number of significant features have been pointed out that could be particularly useful in view of future analysis of turbulent magnetic reconnection with satellite data. In other words, our idea is to find a series of observational events in which satellites cross the K-Hs vortices in the non-linear/saturated phase where one should recover signatures of reconnection events (more generally of small scale dynamics) similar to what was presented here. Cluster orbits near the terminator are ideal for such studies. Moreover, the multispacecraft measurements of NASA/MMS (launched in March 2015), built to study microphysics of phenomena, like the magnetic reconnection and turbulence, will further help to investigate small scale reconnection regions at times where the spacecraft will cross the flank magnetopause.

Realistic Initial Condition

Magnetic reconnection is one of the phenomena that takes place during the non-linear/saturated phase of the Kelvin-Helmholtz instability. Indeed, the dynamics inside the vortices is very rich and strongly depends on the plasma initial conditions, since secondary instabilities can drive the dynamics in different ways. Satellite crossings of the magnetopause, in conditions favorable for the K-H to occur but still not developed, have been searched in the Cluster Active Archive (CAA). Detecting realistic initial conditions for the K-H has been an interesting challenge, not present in the literature. We have focussed on one event in particular, in 2001-11-20, during which Geotail crosses the dayside magnetopause and, at the same time, there are two different stage observations of the dusk flank by Cluster, one before K-H develops and one after.

By analysing all the crossings before vortices formation, we have obtained the important new result that the velocity and the density gradient do not appear at the same time as crossing the magnetopause but there is a shift between them. This shift is more or less of the same order of the velocity and density gradient, that we found to be comparable to one inertial length, d_i. Moreover, going from magnetosheath toward magnetosphere the shift is not always occurring in the same direction. Taking into account this important result that the observations seem to suggest, simulations have been initialized in three different ways, first by taking density and velocity superposed (as usually done in the literature on this topic), or shifted with the

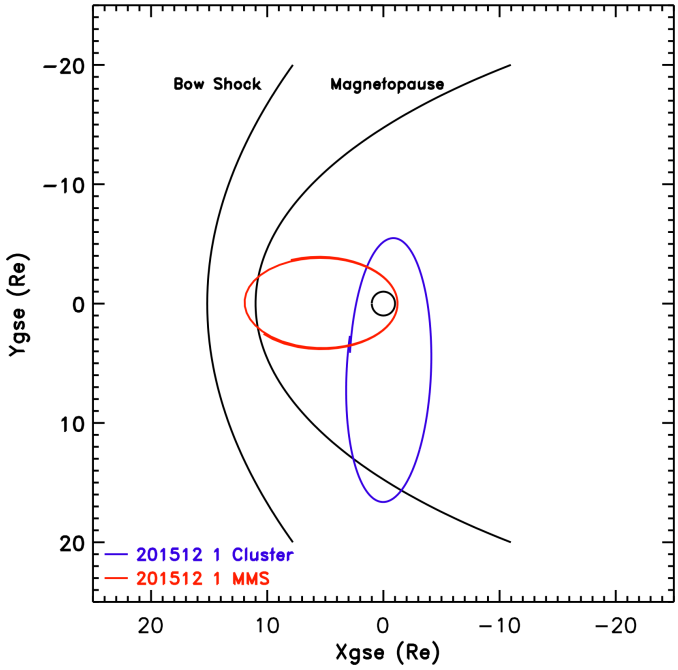

Figure 42: Cluster orbit represented in blue and MMS orbit represented in red, in 2015, projected in the (x_{GSE}, y_{GSE}) equatorial plane. Image courtesy of: P. Escoubet

density gradient moved before or after by 1 d_i with respect to the velocity shear. Running simulations with the total velocity and density jump as obtained from observations, we have found that for all the three cases the pairing process is, at the end, the dominant mechanism. The results of all simulations are therefore consistent with the presence of K-H vortices as observed by Cluster. The agreement is found first in terms of the dynamics but also in terms of the time needed for the vortices to roll-up. Keeping the same parameters but increasing the total velocity and density jumps, as typically done in previous works in the literature on this topic, we have found differences among the simulations with density and velocity shear superposed or shifted. In particular, using a larger velocity jump, vortex structures are faster disrupted in the simulations with centred profiles because of the development of secondary instabilities. On the other hand, in the simulation with initially shifted profiles the secondary instabilities evolve much slower, giving time to the vortices to pair and to form at the end of the simulation a single vortex structure. In the next future we plan to include realistic profiles of temperature and magnetic field to investigate also their role in the system dynamics. A parametric simulation study, varying both the initial shift and total jump of the profiles and including an estimation of the other quantities (like temperature, magnetic field) from observations, will give us an understanding of the effect of the shift in various configurations. Moreover, we plan to compare also the turbulence developing

in the very end of the instability, in simulations initialized with and without an initial shift so as to investigate eventual differences in the development and characteristics of the turbulence.

As regards the shift between density and velocity profiles, further investigations are necessary to understand the mechanisms at play at the magnetopause, responsible of such configurations and a larger statistic of events is needed to generalize also this result. For this purpose we plan also to use the data from the Themis (NASA) mission. The advantage of this mission is that, for orbital reasons Cluster and Themis are at the same time on two opposite sides of the magnetopause and also Themis has the advantage of orbiting in the equatorial plane, that is one of the requirements we used for searching K-H events. Furthermore, it will be possible, in the next future, to combine multispacecraft measurements of MMS with ESA/Cluster data. In figure 42, the orbit of Cluster (blue) and MMS (red) during 2015 are shown in the equatorial plane. The synergy between Cluster and MMS observations is crucial for these studies, in particular considering the much better resolution of particle measurements onboard MMS compared to Geotail. Such measurements are crucial to obtain accurate profiles across the magnetopause.

Another very interesting future development is certainly the possibility to investigate the system dynamics in a 3D configuration. The numerical code is still available. The first step will be to reconstruct the three dimensional dynamics of the magnetopause in order to understand the formation of small scale fluctuations and structures as well as the global evolution that should enable the entry of solar wind plasma into the magnetosphere. A key question is the role of small scale structures and/or reconnection in the transport properties of such system. A key ingredient in such 3D approach will be the inclusion of initial profiles varying, in 3D, with the latitude, as for example done in Ref. Faganello et al. [32].

Part V

APPENDIX

A

GENERALIZED OHM'S LAW

The Ohm's law is very important in plasma physics, it relates the electric field **E** with the current density **J** and it can be determined by summing electrons and protons momentum equations:

$$\rho_\alpha \left(\frac{\partial}{\partial t} + \mathbf{u}_\alpha \cdot \nabla \right) \mathbf{u}_\alpha = -\nabla P_\alpha + q_\alpha \left(\mathbf{E} + \frac{\mathbf{u}_\alpha \wedge \mathbf{B}}{c} \right) - \sum_\beta \rho_\alpha \nu_c (\mathbf{u}_{\beta} - \mathbf{u}_{\alpha})$$

where $\alpha = i, e$ indicates the species and $\rho_\alpha = n_\alpha m_\alpha$ the density. The term $\sum_\beta \rho_\alpha \nu_c (\mathbf{u}_{\beta} - \mathbf{u}_{\alpha})$ is the momentum exchange between electrons and ions and ν_c is the mean collision frequency. Assuming quasi neutrality in a plasma, i.e. $n_i \sim n_e = n$, the motion equations can be written as:

$$n \left(\frac{\partial}{\partial t} + \mathbf{u_e} \cdot \nabla \right) \mathbf{u_e} = -\frac{1}{m_e} \nabla P_e - \frac{e}{m_e} \left(\mathbf{E} + \frac{\mathbf{u_e} \wedge \mathbf{B}}{c} \right) - n \nu_c (\mathbf{u_e} - \mathbf{u_i}) \tag{39}$$

$$n \left(\frac{\partial}{\partial t} + \mathbf{u_i} \cdot \nabla \right) \mathbf{u_i} = -\frac{1}{m_i} \nabla P_i + \frac{e}{m_i} \left(\mathbf{E} + \frac{\mathbf{u_i} \wedge \mathbf{B}}{c} \right) \tag{40}$$

The current density is defined as $\mathbf{J} = ne(\mathbf{u_i} - \mathbf{u_e})$ giving

$$\frac{\partial \mathbf{u_e}}{\partial t} = \frac{\partial \mathbf{u_i}}{\partial t} - \frac{1}{ne} \frac{\partial \mathbf{J}}{\partial t}$$

In the low frequency regime the current displacement can be neglected and from the AmpÃšre law $\mathbf{J} = (c/4\pi) \nabla \wedge \mathbf{B}$, we can write:

$$\frac{\partial \mathbf{u_e}}{\partial t} = \frac{\partial \mathbf{u_i}}{\partial t} - \frac{c}{4\pi e} \frac{\partial}{\partial t} (\nabla \wedge \mathbf{B})$$

Faraday equation, $\partial \mathbf{B}/\partial t = -c \nabla \wedge \mathbf{E}$, allow us to write:

$$\frac{\partial \mathbf{u_e}}{\partial t} = \frac{\partial \mathbf{u_i}}{\partial t} + \frac{c^2}{4\pi e} [\nabla \wedge (\nabla \wedge \mathbf{E})]$$

Using the definition of the current density $\mathbf{J} = ne\,(\mathbf{u_i} - \mathbf{u_e})$, the term $\mathbf{u_e} \cdot \nabla n \mathbf{u_e}$ in eq.s 39 and 40 can be written as:

$$\mathbf{u_e}\cdot\nabla n\mathbf{u_e} = \left(\mathbf{u_i} - \frac{\mathbf{J}}{ne}\right)\cdot\nabla\left(n\mathbf{u_i} - \frac{\mathbf{J}}{e}\right) = \mathbf{u_i}\cdot\nabla n\mathbf{u_i} - \mathbf{u_i}\cdot\nabla\left(\frac{\mathbf{J}}{e}\right) - \frac{\mathbf{J}}{e}\cdot\nabla\mathbf{u_i} + \frac{\mathbf{J}}{ne}\cdot\nabla\left(\frac{\mathbf{J}}{e}\right)$$

By subtracting eq. 40 from eq. 39 and defining $\widetilde{\mu} = 1/m_e + 1/m_i$ we get:

$$\widetilde{\mu}en\mathbf{E} + \frac{c^2}{4\pi e}\nabla\wedge(\nabla\wedge\mathbf{E}) =$$

$$= \frac{\nabla\cdot P_i}{m_i} - \frac{\nabla\cdot P_e}{m_e} + \frac{1}{m_e c}(\mathbf{J}\wedge\mathbf{B}) - \widetilde{\mu}ne\left(\frac{\mathbf{u_i}\wedge\mathbf{B}}{c}\right) +$$

$$+\mathbf{u_i}\cdot\nabla\left(\frac{\mathbf{J}}{e}\right) + \frac{\mathbf{J}}{e}\cdot\nabla\mathbf{u_i} - \frac{\mathbf{J}}{ne}\cdot\nabla\left(\frac{\mathbf{J}}{e}\right) - n\nu_c(\mathbf{u_e} - \mathbf{u_i})$$

By defining $\mu = \mu/m_e$ and dividing all the terms by m_e/ne, the above equation becomes:

$$\mu\mathbf{E} + d_e^2\nabla\wedge(\nabla\wedge\mathbf{E}) =$$

$$= \frac{1}{ne}\frac{m_e}{m_i}(\nabla\cdot P_i) - \frac{\nabla\cdot P_e}{ne} + \frac{1}{nec}(\mathbf{J}\wedge\mathbf{B}) - \mu\left(\frac{\mathbf{u_i}\wedge\mathbf{B}}{c}\right) +$$

$$+\frac{m_e}{ne^2}[\mathbf{u_i}\cdot\nabla\mathbf{J} + \mathbf{J}\cdot\nabla\mathbf{u_i}] - \frac{m_e}{n^2e^3}\mathbf{J}\cdot\nabla\mathbf{J} - \frac{m_e n\nu_c}{ne}(\mathbf{u_e} - \mathbf{u_i})$$

Neglecting terms depending on m_e/m_i , we obtain:

$$\mathbf{E} = -\frac{\nabla\cdot P_e}{ne} - \frac{\mathbf{u_i}\wedge\mathbf{B}}{c} + \frac{1}{nec}(\mathbf{J}\wedge\mathbf{B}) +$$

$$+\frac{m_e}{ne^2}\left\{[\mathbf{u_i}\cdot\nabla\mathbf{J} + \mathbf{J}\cdot\nabla\mathbf{u_i}] - \frac{1}{ne}\mathbf{J}\cdot\nabla\mathbf{J}\right\} + \frac{m_e\nu_c}{ne^2}[ne(\mathbf{u_i} - \mathbf{u_e})] =$$

$$= -\frac{\nabla\cdot P_e}{ne} - \frac{\mathbf{u_i}\wedge\mathbf{B}}{c} + \frac{1}{nec}(\mathbf{J}\wedge\mathbf{B}) + \frac{m_e}{ne^2}\frac{\partial\mathbf{J}}{\partial t} + \frac{m_e}{ne^2}\left\{[\mathbf{u_i}\cdot\nabla\mathbf{J} + \mathbf{J}\cdot\nabla\mathbf{u_i}] - \frac{1}{ne}\mathbf{J}\cdot\nabla\mathbf{J}\right\} + \frac{\mathbf{J}}{\sigma}$$

where $\sigma = ne^2/m_e\nu_c$ is the electrical conductivity. Removing neglectable terms and ordering in terms of importance, from large to smaller scales, the generalized Ohm's law becomes:

$$\mathbf{E} + \frac{\mathbf{u_i}\wedge\mathbf{B}}{c} = \frac{\mathbf{J}}{\sigma} + \frac{1}{nec}(\mathbf{J}\wedge\mathbf{B}) - \frac{\nabla\cdot P_e}{ne} + \frac{m_e}{ne^2}\frac{\partial\mathbf{J}}{\partial t} \tag{41}$$

The terms of the above equation can be ordered. The terms on the left side are dominant and of the same order (the electric field in the

plasma reference frame is zero in absence of currents). At MHD scales, when $l \gg \lambda_{i,e}, \rho_{i,e}$ then both electrons and ions are magnetized and, neglecting collisions, Ideal Ohm's law becomes:

$$\mathbf{E} + \frac{\mathbf{u_i} \wedge \mathbf{B}}{c} = 0$$

The conductivity can be expressed in terms of electron plasma frequency $\sigma = \omega_{pe}^2/(4\pi)\nu_c$ so:

$$\frac{\mathbf{J}/\sigma}{(\mathbf{u_i} \wedge \mathbf{B})/c} \sim \frac{c^2}{4\pi\sigma L u} = \frac{c^2\nu_c}{\omega_{pe}^2 L u} = d_e^2 \frac{\nu_c}{L u}$$

where L and U are the characteristic length and velocity scale of the studied phenomena. This term is important either if collisions are frequent either if the length scale L becomes comparable with the electron skin length d_e. The Hall term $\mathbf{J} \wedge \mathbf{B}/ne$ is the first correction to the Ohm's law. It becomes important at ion scales, $l \sim \lambda_i$ when ions are not magnetized anymore:

$$\frac{\mathbf{J} \wedge \mathbf{B}/nec}{\mathbf{u_i} \wedge \mathbf{B}/c} \sim \frac{c\mathbf{B}}{4\pi neL\mathbf{u}} \sim \frac{\Omega_{c,i}}{\omega_{p,i}^2} \frac{c}{LU} \sim \frac{\nu_A}{U} \frac{d_i}{L}$$

where ν_A is the AlfvÃšn velocity defined as $\nu_A = \mathbf{B}/\sqrt{4\pi\rho}$. The electron pressure term, $\nabla \cdot P_e/ne$ is proportional to :

$$\frac{\nabla \cdot P_e/ne}{\mathbf{u_i} \wedge \mathbf{B}/c} \sim \frac{P}{necLUB} \sim \frac{\nu_A d_i 4\pi P}{ULB^2} \sim \frac{\nu_A}{U} \frac{d_i}{L} \frac{\beta}{2}$$

where $\beta = 8\pi P/B^2$ is the ratio between kinetic and magnetic pressures. This term, when L approaches i, is still negligeable if the plasma is strongly magnetized, $\beta \ll 1$.

B

THE NUMERICAL CODE

The 2D Two-Fluid numerical code, used in this thesis, has periodic boundary conditions in the y-direction and transparent in the inhomogeneous x-direction. The code uses a standard third order Runge-Kutta method for temporal discretization and a sixth-order compact finite difference scheme with spectral-like resolution for spatial derivative along the inhomogeneous x-direction. Fast Fourier transform routines are used for spatial derivative along the periodic y -direction, see Ref. Faganello et al. [31] for details. Since at the x-boundary the system is far from the central region, there it can be described by using ideal MHD instead of the two fluid equations. For this reason the projected characteristics along x-direction of the set of hyperbolic partial differential equations of Ideal MHD have been implemented at this boundary, see Faganello et al. [31].

B.0.0.4 *Temporal discretization*

Runge-Kutta methods are a single step class of methods used for temporal discretizations. In the code we use a third order Runge-Kutta (RK3) method that approximates the solution of a differential equation $y'(t) = f(t, y(t))$ with the initial condition $y(t_0) = y_0$, evaluating $f(t, y(t))$ at three intermediate times per step at discrete time t_i, where $t_i = t_0 + i\Delta t$. The integral of the differential equation is:

$$y_{i+1} = y_i + \int_{t_i}^{t_{i+1}} f(t, y(t))dt \tag{42}$$

To obtain the value of y at the desired time step the idea is to express y_{i+1} as a combination of y_i and f_i :

$$y_{i+1} = y_i + ak_1(t_i, y_i) + bk_2(t_i, y_i) + ck_3(t_i, y_i) + E(\Delta t) \tag{43}$$

where the coefficients k_1, $k_2$and k_3 are given by:

$$k_1 = f(t_i, y_i)$$

$$k_2 = f(t_i + \alpha\Delta t, y_i + \alpha_1 k_1)$$

$$k_3 = f(t_i + \beta\Delta t, y_i - \beta_1 k_1 \Delta t + \gamma_1 k_2 \Delta t)$$

and α, α_1, β, $\beta_1$and γ_1 are coefficients to be determined to have an accuracy at third order, i. e. $E(\Delta t) \sim \mathcal{O}(\Delta t^4)$. By expanding in Taylor series the coefficients k_1, $k_2$and k_3 and comparing the expansions with eq. 43, we get the values of the coefficients. The RK3 scheme, up to third order , is then:

$$y_{i+1} = y_i + \frac{1}{6}\Delta t\,(k_1 + 4k_2 + k_3) \tag{44}$$

with:

$$k_1 = f(t_i, y_i)$$

$$k_2 = f(t_i + \frac{1}{2}\Delta t, y_i + \frac{\Delta t}{2} k_1)$$

$$k_3 = f(t_i + \Delta t, y_i - k_1 \Delta t + 2k_2 \Delta t)$$

For more details, see Canuto et al. [14].

B.0.0.5 *Spatial derivative*

As discussed before spatial derivatives in the periodic y-direction are performed using the Fast Fourier transform routines while along the inhomogeneous x-direction a sixth order finite difference scheme is applied, see Lele [67]. In the finite difference schemes the approximation to the first derivative of a certain function f, is obtained through a combination of the values of the function on a series of nodes, $f_i \equiv f(t_i, y_i)$. The finite difference approximation of the first derivative f'_i on the node i, depends on the values of the function f_i on the nodes closed to i:

$$\beta f'_{i-2} + \alpha f'_{i-1} + f'_i + \alpha f'_{i+1} + \beta f'_{i+2} =$$

$$= c\frac{f_{i+3} - f_{i-3}}{6\Delta x} + b\frac{f_{i+2} - f_{i-2}}{4\Delta x} + a\frac{f_{i+1} - f_{i-1}}{2\Delta x} \tag{45}$$

The coefficients in the above equation are obtained by matching with the Taylor coefficients at the various orders. The implicit sixth order difference scheme is obtained setting $\alpha = 1/3$ and its coefficients are:

$$\beta = 0 \quad a = \frac{14}{9}, \quad b = \frac{1}{9}, \quad c = 0 \tag{46}$$

B.0.0.6 *Filters*

Numerical stability is achieved through the use of filters, a spectral filter along the periodic y direction and a sixth order spectral like filtering scheme along the inhomogeneous x-direction, Ref. Lele [67]. Compact schemes, described above can be used for filtering techniques. Here they are used to remove short scale length. The filtered values of the function, $\hat{f}_i$, at the node x_i, are found using the following approximation:

$$\beta\hat{f}_{i-2} + \alpha\hat{f}_{i-1} + \hat{f}_i + \alpha\hat{f}_{i+1} + \beta\hat{f}_{i+2} =$$

$$= af_i + \frac{d}{2}(f_{i+3} - f_{i-3}) + \frac{c}{2}(f_{i+2} - f_{i-2}) + \frac{b}{2}(f_{i+1} - f_{i-1}) \quad (47)$$

Analysing the above equation in the Fourier space, we derive the associated transfer function of this filtering scheme as a function of the scaled wavenumber $w = 2\pi kh/L$, with $h = L/N$ and w in the domain $[0, \pi]$. Transfer function is defined as the ratio between the output over input signal, and for this case it has the form:

$$T(w) = \frac{a + b\cos(w) + c\cos(2w) + d\cos(3w)}{1 + 2\alpha\cos(w) + 2\beta\cos(2w)} \quad (48)$$

For all the filters we require that $T(\pi) = 0$. As before, by matching the Taylor series coefficient at various order, we obtain the coefficient relation for the sixth order scheme:

$$a = \frac{1}{16}(11 + 10\alpha - 10\beta)\,;\; b = \frac{1}{32}(15 + 34\alpha + 30\beta)\,;$$

$$c = \frac{1}{16}(-3 + 6\alpha + 26\beta)\,;\; d = \frac{1}{32}(1 - 2\alpha + 2\beta)\,; \quad (49)$$

Imposing $\beta = 0$, we use this explicit sixth order scheme in the inhomogeneous x-direction.

The nodes near the boundaries must be treated separately. The near boundary formulas at fourth order accuracy are:

$$\begin{cases} \hat{f}_1 = \frac{15}{16}f_1 + \frac{1}{16}(4f_2 - 6f_3 + 4f_4 - f_5) \\ \hat{f}_2 = \frac{3}{4}f_2 + \frac{1}{16}(f_1 + 6f_3 - 4f_4 + f_5) \\ \hat{f}_3 = \frac{5}{8}f_3 + \frac{1}{16}(-f_1 + 4f_2 + 4f_4 - f_5) \end{cases}$$

Imposing the additional filtering constraint:

$$\frac{d^2T}{dw^2}(\pi) = 0$$

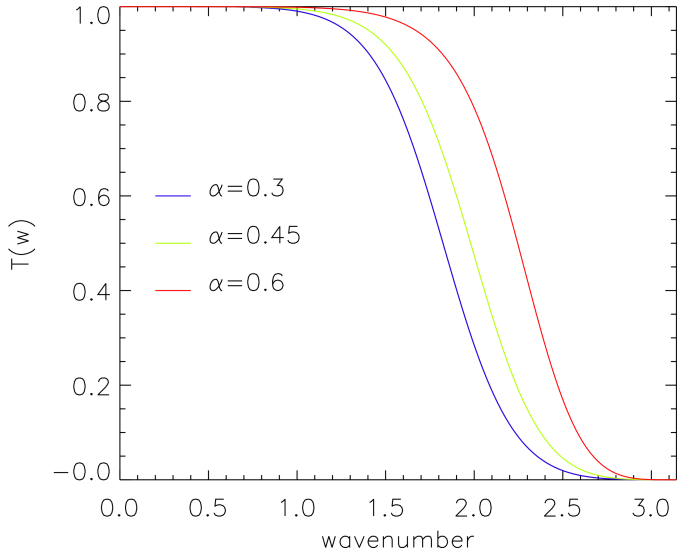

Figure 43: Filtering transfer function, $T(w)$, as a function of the wavenumber. $T(w)$ is plotted in blue for $\alpha = 0.3$, in green for $\alpha = 0.45$ and in red for $\alpha = 0.6$.

i.e. imposing that the transfer function goes slowly to zero at the boundary and adding the sixth order constraints when matching with Taylor coefficients we get the following relation between coefficients:

$$\beta = \frac{3-2\alpha}{10};\ a = \frac{2+3\alpha}{4};\ b = \frac{6+7\alpha}{8};\ c = \frac{6+\alpha}{20};\ d = \frac{2-3\alpha}{40}$$

This sixth order spectral-like filtering scheme is used in the periodic y-direction.

In figure 43 we plot the transfer function as a function of the 'scaled wavenumber' for various values of α. The transfer function is plotted in blue for $\alpha = 0.3$, in green for $\alpha = 0.45$ and in red for $\alpha = 0.6$. We observe that by reducing the coefficient α the filter acts more towards small waves.

B.0.0.7 *Initial velocity field perturbations*

Initial small amplitude perturbations $\delta\mathbf{u}$ are applied at the velocity field:

$$\begin{cases} U_x(y) = \delta u_x \\ U_y(x) = U_y + \delta u_y \\ U_z = 0 \end{cases} \tag{50}$$

Velocity perturbations are incompressible, doing so all the perturbation energy is used for the onset of the instability otherwise part of the perturbation energy would be used to also compress the plasma. The initial incompressible velocity perturbations can be written in

terms of the stream function φ, i.e. as $\delta\mathbf{u} = \hat{e}_z \wedge \nabla\psi$ where each component reads: $\delta u_x = -\frac{\partial\varphi}{\partial y}$ and $\delta u_y = \frac{\partial\varphi}{\partial x}$. The initial perturbations of the stream function are defined as:

$$\varphi(x,y) = A \sum_{m=1}^{N_y/2} f(x)\cos(k_m y + \phi)\frac{1}{m}$$

where A is the amplitude of the perturbations. In our case the initial amplitude of the velocity perturbations is 10^{-3}. In the above equation $f(x) = exp\left\{-\left[(x - x_c)/3L\right]^2\right\}$, N_y is the total node number in the y-direction, $k_m = 2\pi m/L_y$ are the wavenumber of the resonant modes and ϕ is a random phase.

BIBLIOGRAPHY

[1] O Alexandrova. Solar wind vs magnetosheath turbulence and alfvén vortices. *Nonlinear Processes in Geophysics*, 15(1):95–108, 2008.

[2] Olga Alexandrova, Catherine Lacombe, and Andre Mangeney. Spectra and anisotropy of magnetic fluctuations in the earth's magnetosheath: Cluster observations. *arXiv preprint arXiv:0810.0675*, 2008.

[3] Steven A Balbus and John F Hawley. Instability, turbulence, and enhanced transport in accretion disks. *Reviews of modern physics*, 70(1):1, 1998.

[4] George Keith Batchelor. *An introduction to fluid dynamics*. Cambridge university press, 2000.

[5] TM Bauer, G Paschmann, N Sckopke, RA Treumann, W Baumjohann, and T-D Phan. Fluid and particle signatures of dayside reconnection. In *Annales Geophysicae*, volume 19, pages 1045–1063, 2001.

[6] Gérard Belmont, Roland Grappin, Fabrice Mottez, Filippo Pantellini, and Guy Pelletier. *Collisionless plasmas in astrophysics*. John Wiley & Sons, 2013.

[7] Joachim Birn and Eric Ronald Priest. *Reconnection of magnetic fields: magnetohydrodynamics and collisionless theory and observations*. Cambridge University Press, 2007.

[8] Scott A Boardsen, Torbjörn Sundberg, James A Slavin, Brian J Anderson, Haje Korth, Sean C Solomon, and Lars G Blomberg. Observations of kelvin-helmholtz waves along the dusk-side boundary of mercury ś magnetosphere during messengerś third flyby. *Geophysical Research Letters*, 37(12), 2010.

[9] Joseph E Borovsky and Herbert O Funsten. Role of solar wind turbulence in the coupling of the solar wind to the earth's magnetosphere. *Journal of Geophysical Research: Space Physics (1978–2012)*, 108(A6), 2003.

[10] Joseph E Borovsky, Michelle F Thomsen, and Richard C Elphic. The driving of the plasma sheet by the solar wind. *Journal of Geophysical Research: Space Physics (1978–2012)*, 103(A8):17617–17639, 1998.

[11] Roberto Bruno and Vincenzo Carbone. The solar wind as a turbulence laboratory. *Living Reviews in Solar Physics*, 2:4, 2005.

[12] Leonard F Burlaga. Interplanetary magnetohydrodynamics. *Interplanetary magnetohydrodynamics, by LF Burlag. International Series in Astronomy and Astrophysics, Vol. 3, Oxford University Press. 1995. 272 pages; ISBN13: 978-0-19-508472-6*, 3, 1995.

[13] Enrico Camporeale and David Burgess. The dissipation of solar wind turbulent fluctuations at electron scales. *The Astrophysical Journal*, 730(2):114, 2011.

[14] C. Canuto, M. Y. Hussaini, A. Quarteroni, and T. A. Zang. *Spectral Methods: Fundamentals in Single Domains*. Springer Science & Business Media, 1 edition, 2007.

[15] PA Cassak and MA Shay. Scaling of asymmetric magnetic reconnection: General theory and collisional simulations. *Physics of Plasmas (1994-present)*, 14(10):102114, 2007.

[16] Subrahmanyan Chandrasekhar. *Hydrodynamic and hydromagnetic stability*. Courier Corporation, 2013.

[17] Alexandros Chasapis, Alessandro Retinò, Fouad Sahraoui, Andris Vaivads, Yuri Khotyaintsev, Dimitri Sundvisk, Antonella Greco, Luca Sorriso-Valvo, and Patrick Canu. Thin current sheets and associated electron heating in turbulent space plasma. February 2015. Astrophysical Journal, Letters.

[18] Luca Comisso and Felipe A Asenjo. Thermal-inertial effects on magnetic reconnection in relativistic pair plasmas. *Physical review letters*, 113(4):045001, 2014.

[19] MM Cowee, D Winske, and SP Gary. Two-dimensional hybrid simulations of superdiffusion at the magnetopause driven by kelvin-helmholtz instability. *Journal of Geophysical Research: Space Physics (1978–2012)*, 114(A10), 2009.

[20] MM Cowee, D Winske, and SP Gary. Hybrid simulations of plasma transport by kelvin-helmholtz instability at the magnetopause: Density variations and magnetic shear. *Journal of Geophysical Research: Space Physics (1978–2012)*, 115(A6), 2010.

[21] SWH Cowley. Evidence for the occurrence and importance of reconnection between the earth's magnetic field and the interplanetary magnetic field. *Magnetic Reconnection in Space and Laboratory Plasmas*, pages 375–378, 1984.

[22] A Czaykowska, TM Bauer, RA Treumann, and W Baumjohann. Magnetic field fluctuations across the earth's bow shock. In *Annales Geophysicae*, volume 19, pages 275–287, 2001.

[23] I Dandouras and A Barthe. User guide to the cis measurements in the cluster active archive (caa). 2010.

[24] PME Décréau, P Fergeau, M Lévèque, Ph Martin, O Randriamboarison, FX Sené, JG Trotignon, P Canu, H De Feraudy, A Bahnsen, et al. Whisper: A sounder and high-frequency wave analyser experiment. In *Cluster: Mission, Payload and Supporting Activities*, volume 1159, page 49, 1993.

[25] Philip G Drazin and William Hill Reid. *Hydrodynamic stability*. Cambridge university press, 2004.

[26] J. W. Dungey. The interplanetary magnetic field and the auroral zones. *PRL*, 6(2):47–48, 1961.

[27] James Wynne Dungey. Electrodynamics of the outer atmosphere. In *Physics of the Ionosphere*, volume 1, page 229, 1955.

[28] JW Dungey. The structure of the exosphere or adventures in velocity space. *Geophysics, The Earth's Environment*, 503, 1963.

[29] Alexander I Ershkovich. Kelvin-helmholtz instability in type-1 comet tails and associated phenomena. *Space Science Reviews*, 25(1):3–34, 1980.

[30] M Faganello, F Califano, and F Pegoraro. Competing mechanisms of plasma transport in inhomogeneous configurations with velocity shear: the solar wind interaction with earth's magnetosphere. *Physical review letters*, 100(1):015001, 2008.

[31] M Faganello, F Califano, and F Pegoraro. Being on time in magnetic reconnection. *New Journal of Physics*, 11(6):063008, 2009.

[32] M Faganello, F Califano, F Pegoraro, and T Andreussi. Double mid-latitude dynamical reconnection at the magnetopause: An efficient mechanism allowing solar wind to enter the earth's magnetosphere. *EPL (Europhysics Letters)*, 100(6):69001, 2012.

[33] M Faganello, F Califano, F Pegoraro, T Andreussi, and S Benkadda. Magnetic reconnection and kelvin–helmholtz instabilities at the earth's magnetopause. *Plasma Physics and Controlled Fusion*, 54(12):124037, 2012.

[34] DH Fairfield, A Otto, T Mukai, S Kokubun, RP Lepping, JT Steinberg, AJ Lazarus, and T Yamamoto. Geotail observations of the kelvin-helmholtz instability at the equatorial magnetotail boundary for parallel northward fields. *Journal of Geophysical Research: Space Physics (1978–2012)*, 105(A9):21159–21173, 2000.

[35] DH Fairfield, MM Kuznetsova, T Mukai, T Nagai, TI Gombosi, and AJ Ridley. Waves on the dusk flank boundary layer during very northward interplanetary magnetic field conditions: Observations and simulation. *Journal of Geophysical Research: Space Physics (1978–2012)*, 112(A8), 2007.

[36] Charles J Farrugia, Fausto T Gratton, and Roy B Torbert. Viscous-type processes in the solar wind-magnetosphere interaction. *Space Science Reviews*, 95(1-2):443–456, 2001.

[37] Claire Foullon, Charles John Farrugia, AN Fazakerley, Christopher J Owen, FT Gratton, and Roy Banks Torbert. Evolution of kelvin-helmholtz activity on the dusk flank magnetopause. *Journal of Geophysical Research: Space Physics (1978–2012)*, 113 (A11), 2008.

[38] Claire Foullon, Charles J Farrugia, Christopher J Owen, Andrew Fazakerley, and FT Gratton. Kelvin-helmholtz multispacecraft studies at the earth's magnetopause boundaries. 2010.

[39] Claire Foullon, Charles John Farrugia, AN Fazakerley, Christopher J Owen, FT Gratton, and Roy Banks Torbert. On the multispacecraft determination of periodic surface wave phase speeds and wavelengths. *Journal of Geophysical Research: Space Physics (1978–2012)*, 115(A9), 2010.

[40] Claire Foullon, Erwin Verwichte, Valery M Nakariakov, Katarina Nykyri, and Charles J Farrugia. Magnetic kelvin-helmholtz instability at the sun. *The Astrophysical Journal Letters*, 729(1):L8, 2011.

[41] Adam Frank, TW Jones, Dongsu Ryu, and Joseph B Gaalaas. The mhd kelvin-helmholtz instability: A two-dimensional numerical study. *arXiv preprint astro-ph/9510115*, 1995.

[42] Uriel Frisch. *Turbulence: the legacy of AN Kolmogorov*. Cambridge university press, 1995.

[43] MASAKI Fujimoto, T Mukai, H Kawano, M Nakamura, A Nishida, Y Saito, T Yamamoto, and S Kokubun. Structure of the low-latitude boundary layer: A case study with geotail data. *Journal of Geophysical Research: Space Physics (1978–2012)*, 103(A2):2297–2308, 1998.

[44] MASAKI Fujimoto, T Terasawa, T Mukai, Y Saito, T Yamamoto, and S Kokubun. Plasma entry from the flanks of the near-earth magnetotail: Geotail observations. *Journal of Geophysical Research: Space Physics (1978–2012)*, 103(A3):4391–4408, 1998.

[45] Johannes Geiss, G Gloeckler, and R Von Steiger. Origin of the solar wind from composition data. *Space Science Reviews*, 72 (1-2):49–60, 1995.

[46] A Greco, P Chuychai, WH Matthaeus, S Servidio, and P Dmitruk. Intermittent mhd structures and classical discontinuities. *Geophysical Research Letters*, 35(19), 2008.

[47] G Gustafsson, R Bostrom, B Holback, G Holmgren, A Lundgren, K Stasiewicz, L Åhlén, FS Mozer, D Pankow, P Harvey, et al. The electric field and wave experiment for the cluster mission. In *The Cluster and Phoenix Missions*, pages 137–156. Springer, 1997.

[48] MA Hapgood. Space physics coordinate transformations: the role of precession. In *Annales Geophysicae*, volume 13, pages 713–716. Springer, 1995.

[49] Akira Hasegawa and Masahiro Wakatani. Plasma edge turbulence. *Physical Review Letters*, 50(9):682, 1983.

[50] H Hasegawa, M Fujimoto, T-D Phan, H Reme, A Balogh, MW Dunlop, C Hashimoto, and R TanDokoro. Transport of solar wind into earth's magnetosphere through rolled-up kelvin–helmholtz vortices. *Nature*, 430(7001):755–758, 2004.

[51] H Hasegawa, M Fujimoto, Y Saito, and T Mukai. Dense and stagnant ions in the low-latitude boundary region under northward interplanetary magnetic field. *Geophysical research letters*, 31(6), 2004.

[52] H Hasegawa, M Fujimoto, K Takagi, Y Saito, T Mukai, and H Rème. Single-spacecraft detection of rolled-up kelvin-helmholtz vortices at the flank magnetopause. *Journal of Geophysical Research: Space Physics (1978–2012)*, 111(A9), 2006.

[53] H Hasegawa, A Retinò, Andris Vaivads, Yuri Khotyaintsev, Mats André, TKM Nakamura, W-L Teh, BU Sonnerup, SJ Schwartz, Y Seki, et al. Kelvin-helmholtz waves at the earth's magnetopause: Multiscale development and associated reconnection. *Journal of Geophysical Research: Space Physics (1978–2012)*, 114(A12), 2009.

[54] Hiroshi Hasegawa. Structure and dynamics of the magnetopause and its boundary layers. *Monogr. Environ. Earth Planets*, 1(2):71–119, 2012.

[55] Christopher T Haynes, David Burgess, and Enrico Camporeale. Reconnection and electron temperature anisotropy in subproton scale plasma turbulence. *The Astrophysical Journal*, 783 (1):38, 2014.

[56] P Henri, F Califano, M Faganello, and F Pegoraro. Magnetised kelvin-helmholtz instability in the intermediate regime between subsonic and supersonic regimes. *Physics of Plasmas*, 19(7):072908, 2012.

[57] P Henri, SS Cerri, F Califano, F Pegoraro, C Rossi, M Faganello, O Šebek, PM Trávníček, P Hellinger, JT Frederiksen, et al. Nonlinear evolution of the magnetized kelvin-helmholtz instability: From fluid to kinetic modeling. *Physics of Plasmas (1994-present)*, 20(10):102118, 2013.

[58] EW Hones, J Birn, SJ Bame, JR Asbridge, G Paschmann, N Sckopke, and G Haerendel. Further determination of the characteristics of magnetospheric plasma vortices with isee 1 and 2. *Journal of Geophysical Research: Space Physics (1978–2012)*, 86(A2): 814–820, 1981.

[59] Wendell Horton. Spectral distribution of drift-wave fluctuations in tokamaks. *Physical Review Letters*, 37(19):1269, 1976.

[60] JD Huba. Hall dynamics of the kelvin-helmholtz instability. *Physical review letters*, 72(13):2033, 1994.

[61] JD Huba. Hall magnetic reconnection: Guide field dependence. *Physics of plasmas*, 12(1), 2005.

[62] H Karimabadi, V Roytershteyn, M Wan, WH Matthaeus, W Daughton, P Wu, M Shay, B Loring, J Borovsky, Ersilia Leonardis, et al. Coherent structures, intermittent turbulence, and dissipation in high-temperature plasmas. *Physics of Plasmas (1994-present)*, 20(1):012303, 2013.

[63] Roger A Kopp. Theory of coronal streamer formation. Technical report, Los Alamos National Lab., NM (United States), 1992.

[64] Harri Laakso and Arne Pedersen. Ambient electron density derived from differential potential measurements. *Measurement Techniques in Space Plasmas: Particles*, pages 49–54, 1998.

[65] Harri Laakso, Matthew Taylor, and C Philippe Escoubet. *The Cluster Active Archive: Studying the Earth's Space Plasma Environment*. Springer Science & Business Media, 2009.

[66] G Le, CT Russell, JT Gosling, and MF Thomsen. Isee observations of low-latitude boundary layer for northward interplanetary magnetic field: Implications for cusp reconnection. *Journal of Geophysical Research: Space Physics (1978–2012)*, 101(A12): 27239–27249, 1996.

[67] Sanjiva K Lele. Compact finite difference schemes with spectral-like resolution. *Journal of computational physics*, 103(1):16–42, 1992.

[68] Ersilia Leonardis, Sandra C Chapman, W Daughton, V Roytershteyn, and H Karimabadi. Identification of intermittent multifractal turbulence in fully kinetic simulations of magnetic reconnection. *Physical review letters*, 110(20):205002, 2013.

[69] Marcel Lesieur. *Turbulence in fluids*, volume 84. Springer Science & Business Media, 2008.

[70] RVE Lovelace, MM Romanova, and WI Newman. Kelvin-helmholtz instability of the magnetopause of disc-accreting stars. *Monthly Notices of the Royal Astronomical Society*, 402(4): 2575–2582, 2010.

[71] A Masters, N Achilleos, MG Kivelson, N Sergis, MK Dougherty, MF Thomsen, CS Arridge, SM Krimigis, HJ McAndrews, SJ Kanani, et al. Cassini observations of a kelvin-helmholtz vortex in saturn's outer magnetosphere. *Journal of Geophysical Research: Space Physics (1978–2012)*, 115(A7), 2010.

[72] Yosuke Matsumoto and Masahiro Hoshino. Onset of turbulence induced by a kelvin-helmholtz vortex. *Geophysical research letters*, 31(2), 2004.

[73] Yosuke Matsumoto and Masahiro Hoshino. Turbulent mixing and transport of collisionless plasmas across a stratified velocity shear layer. *Journal of Geophysical Research: Space Physics (1978–2012)*, 111(A5), 2006.

[74] Yosuke Matsumoto and Kanako Seki. Formation of a broad plasma turbulent layer by forward and inverse energy cascades of the kelvin–helmholtz instability. *Journal of Geophysical Research: Space Physics (1978–2012)*, 115(A10), 2010.

[75] A. Miura. Anomalous transport by magnetohydrodynamic kelvin-helmholtz instabilities in the solar wind-magnetosphere interaction. *Journal of Geophysical Research: Space Physics (1978–2012)*, 89(A2):801–818, 1984.

[76] A. Miura. Simulation of Kelvin-Helmholtz instability at the magnetospheric boundary. *Journal of Geophysical Research*, 92: 3195–3206, 1987.

[77] Akira Miura. Kelvin-helmholtz instability at the magnetopause: Computer simulations. *Physics of the Magnetopause*, pages 285–291, 1995.

[78] Akira Miura and PL Pritchett. Nonlocal stability analysis of the mhd kelvin-helmholtz instability in a compressible plasma. *Journal of Geophysical Research: Space Physics*, 87(A9):7431–7444, 1982.

[79] TKM Nakamura and M Fujimoto. Magnetic reconnection within rolled-up mhd-scale kelvin-helmholtz vortices: Two-fluid simulations including finite electron inertial effects. *Geophysical research letters*, 32(21), 2005.

[80] TKM Nakamura, D Hayashi, M Fujimoto, and I Shinohara. Decay of mhd-scale kelvin-helmholtz vortices mediated by parasitic electron dynamics. *Physical review letters*, 92(14):145001, 2004.

[81] TKM Nakamura, M Fujimoto, and A Otto. Structure of an mhd-scale kelvin-helmholtz vortex: Two-dimensional two-fluid simulations including finite electron inertial effects. *Journal of Geophysical Research: Space Physics (1978–2012)*, 113(A9), 2008.

[82] TKM Nakamura, Hiroshi Hasegawa, Iku Shinohara, and Masaki Fujimoto. Evolution of an mhd-scale kelvin-helmholtz vortex accompanied by magnetic reconnection: Two-dimensional particle simulations. *Journal of Geophysical Research: Space Physics*, 116(A3), 2011.

[83] K Nykyri and A Otto. Plasma transport at the magnetospheric boundary due to reconnection in kelvin-helmholtz vortices. *Geophysical research letters*, 28(18):3565–3568, 2001.

[84] K Nykyri, A Otto, B Lavraud, C Mouikis, LM Kistler, A Balogh, and H Reme. Cluster observations of reconnection due to the kelvin-helmholtz instability at the dawnside magnetospheric flank. In *Annales Geophysicae*, volume 24, pages 2619–2643, 2006.

[85] Leon Ofman and Barbara J Thompson. Sdo/aia observation of kelvin–helmholtz instability in the solar corona. *The Astrophysical Journal Letters*, 734(1):L11, 2011.

[86] A Otto and DH Fairfield. Kelvin-helmholtz instability at the magnetotail boundary: Mhd simulation and comparison with geotail observations. *Journal of Geophysical Research: Space Physics (1978–2012)*, 105(A9):21175–21190, 2000.

[87] F Palermo, M Faganello, F Califano, F Pegoraro, and O Le Contel. Compressible kelvin–helmholtz instability in supermagnetosonic regimes. *Journal of Geophysical Research: Space Physics*, 116(A4), 2011.

[88] E. N. Parker. Dynamics of the interplanetary gas and magnetic field. *Astrophysical Journal*, 128:664–676, January 1958.

[89] Götz Paschmann and Patrick W Daly. Analysis methods for multi-spacecraft data. 1998.

[90] A Pedersen, P Décréau, C-P Escoubet, G Gustafsson, H Laakso, P-A Lindqvist, B Lybekk, A Masson, F Mozer, and A Vaivads. Four-point high time resolution information on electron densities by the electric field experiments (efw) on cluster. In *Annales Geophysicae*, volume 19, pages 1483–1489, 2001.

[91] A Pedersen, B Lybekk, Mats André, Anders Eriksson, A Masson, FS Mozer, P-A Lindqvist, PME Décréau, I Dandouras, J-A Sauvaud, et al. Electron density estimations derived from spacecraft potential measurements on cluster in tenuous plasma regions. *Journal of Geophysical Research: Space Physics (1978–2012)*, 113(A7), 2008.

[92] TD Phan, D Larson, J McFadden, RP Lin, C Carlson, M Moyer, KI Paularena, M McCarthy, GK Parks, H Reme, et al. Low-latitude dusk flank magnetosheath, magnetopause, and boundary layer for low magnetic shear: Wind observations. *Journal of Geophysical Research: Space Physics*, 102(A9):19883–19895, 1997.

[93] PL Pritchett and FV Coroniti. Three-dimensional collisionless magnetic reconnection in the presence of a guide field. *Journal of Geophysical Research: Space Physics (1978–2012)*, 109(A1), 2004.

[94] H Reme, C Aoustin, JM Bosqued, I Dandouras, B Lavraud, JA Sauvaud, A Barthe, J Bouyssou, Th Camus, O Coeur-Joly, et al. First multispacecraft ion measurements in and near the earth's magnetosphere with the identical cluster ion spectrometry (cis) experiment. In *Annales Geophysicae*, volume 19, pages 1303–1354, 2001.

[95] Alessandro Retinò, David Sundkvist, Andris Vaivads, F Mozer, Mats André, and CJ Owen. In situ evidence of magnetic reconnection in turbulent plasma. *Nature Physics*, 3(4):236–238, 2007.

[96] L Rezeau and G Belmont. Magnetic turbulence at the magnetopause, a key problem for understanding the solar wind/magnetosphere exchanges. *Space Science Reviews*, 95(1-2):427–441, 2001.

[97] Edmond C Roelof and David G Sibeck. Magnetopause shape as a bivariate function of interplanetary magnetic field bz and solar wind dynamic pressure. *Journal of Geophysical Research: Space Physics (1978–2012)*, 98(A12):21421–21450, 1993.

[98] Claudia Rossi, Alessandro Retinò, and Francesco Califano. Two-fluid simulations of kelvin-helmholtz instability with realistic initial conditions from magnetopause observations. Journal of Geophysical Research (to be submitted), 2015.

[99] Christopher T Russell and RC Elphic. Isee observations of flux transfer events at the dayside magnetopause. *Geophysical Research Letters*, 6(1):33–36, 1979.

[100] F Sahraoui, G Belmont, L Rezeau, N Cornilleau-Wehrlin, JL Pinçon, and A Balogh. Anisotropic turbulent spectra in the terrestrial magnetosheath as seen by the cluster spacecraft. *Physical review letters*, 96(7):075002, 2006.

[101] Greg Salvesen, Kris Beckwith, Sean M O'Neill, Mitchell C Begelman, and Jacob B Simon. Energetics and dissipation in the magnetised kelvin-helmholtz instability: the non-linear regime. Technical report, 2013.

[102] J Saur, H Politano, A Pouquet, and WH Matthaeus. Evidence for weak mhd turbulence in the middle magnetosphere of jupiter. *Astronomy & Astrophysics*, 386(2):699–708, 2002.

[103] M Scholer and RA Treumann. The low-latitude boundary layer at the flanks of the magnetopause. *Space Science Reviews*, 80(1-2): 341–367, 1997.

[104] N Sckopke, G Paschmann, G Haerendel, BU Sonnerup, SJ Bame, TG Forbes, EW Hones, and CT Russell. Structure of the low-latitude boundary layer. *Journal of Geophysical Research: Space Physics (1978–2012)*, 86(A4):2099–2110, 1981.

[105] S Servidio, A Greco, WH Matthaeus, KT Osman, and P Dmitruk. Statistical association of discontinuities and reconnection in magnetohydrodynamic turbulence. *Journal of Geophysical Research: Space Physics*, 116(A9), 2011.

[106] J V Shebalin, W H Matthaeus, and Montgomery D. Anisotropy in mhd turbulence due to a mean magnetic field, 1983.

[107] J-H Shue, JK Chao, HC Fu, CT Russell, P Song, KK Khurana, and HJ Singer. A new functional form to study the solar wind control of the magnetopause size and shape. *Journal of Geophysical Research: Space Physics (1978–2012)*, 102(A5):9497–9511, 1997.

[108] J-H Shue, P Song, CT Russell, JT Steinberg, JK Chao, G Zastenker, OL Vaisberg, S Kokubun, HJ Singer, TR Detman, et al. Magnetopause location under extreme solar wind conditions. *Journal of Geophysical Research: Space Physics (1978–2012)*, 103 (A8):17691–17700, 1998.

[109] R Smets, D Delcourt, G Chanteur, and TE Moore. On the incidence of kelvin-helmholtz instability for mass exchange process at the earth's magnetopause. In *Annales Geophysicae*, volume 20, pages 757–769, 2002.

[110] P Song and CT Russell. Model of the formation of the low-latitude boundary layer for strongly northward interplanetary magnetic field. *Journal of Geophysical Research: Space Physics (1978–2012)*, 97(A2):1411–1420, 1992.

[111] Bengt UÖ Sonnerup, Hiroshi Hasegawa, Wai-Leong Teh, and Lin-Ni Hau. Grad-shafranov reconstruction: An overview. *Journal of Geophysical Research: Space Physics (1978–2012)*, 111(A9), 2006.

[112] Torbjörn Sundberg, SA Boardsen, JA Slavin, Lars G Blomberg, and H Korth. The kelvin–helmholtz instability at mercury: an assessment. *Planetary and Space Science*, 58(11):1434–1441, 2010.

[113] David Sundkvist, Alessandro Retinò, Andris Vaivads, and Stuart D Bale. Dissipation in turbulent plasma due to reconnection in thin current sheets. *Physical review letters*, 99(2):025004, 2007.

[114] Peter A Sweet. The neutral point theory of solar flares. In *Electromagnetic phenomena in cosmical physics*, volume 6, page 123, 1958.

[115] K Takagi, C Hashimoto, H Hasegawa, M Fujimoto, and R Tan-Dokoro. Kelvin-helmholtz instability in a magnetotail flank-like geometry: Three-dimensional mhd simulations. *Journal of Geophysical Research: Space Physics (1978–2012)*, 111(A8), 2006.

[116] A Tenerani, M Faganello, F Califano, and F Pegoraro. Nonlinear vortex dynamics in an inhomogeneous magnetized plasma with a sheared velocity field. *Plasma Physics and Controlled Fusion*, 53(1):015003, 2011.

[117] T Terasawa, M Fujimoto, T Mukai, I Shinohara, Y Saito, T Yamamoto, S Machida, S Kokubun, AJ Lazarus, JT Steinberg, et al. Solar wind control of density and temperature in the near-earth plasma sheet: Wind/geotail collaboration. *Geophysical research letters*, 24(8):935–938, 1997.

[118] VA Thomas and D Winske. Kinetic simulations of the kelvin-helmholtz instability at the magnetopause. *Journal of Geophysical Research: Space Physics (1978–2012)*, 98(A7):11425–11438, 1993.

[119] SA Thorpe. Turbulence in stably stratified fluids: A review of laboratory experiments. *Boundary-Layer Meteorology*, 5(1-2):95–119, 1973.

[120] Rudolf A Treumann and Wolfgang Baumjohann. Collisionless magnetic reconnection in space plasmas. *arXiv preprint arXiv:1401.5995*, 2014.

[121] JG Trotignon, PME Décréau, JL Rauch, O Randriamboarison, V Krasnoselskikh, P Canu, H Alleyne, K Yearby, E Le Guirriec, HC Séran, et al. How to determine the thermal electron density and the magnetic field strength from the cluster/whisper observations around the earth. In *Annales Geophysicae*, volume 19, pages 1711–1720, 2001.

[122] JG Trotignon, JL Rauch, PME Décréu, P Canu, and J Lemaire. Active and passive plasma wave investigations in the earth's environment: The cluster/whisper experiment. *Advances in Space Research*, 31(5):1449–1454, 2003.

[123] GR Tynan, A Fujisawa, and G McKee. A review of experimental drift turbulence studies. *Plasma Physics and Controlled Fusion*, 51 (11):113001, 2009.

[124] F Valentini, F Califano, and P Veltri. Two-dimensional kinetic turbulence in the solar wind. *Physical review letters*, 104(20): 205002, 2010.

[125] Mario Vietri and Luigi Stella. A new instability of accretion disks around magnetic compact stars. *The Astrophysical Journal*, 503(1):350, 1998.

[126] J Vogt, S Haaland, and G Paschmann. Accuracy of multipoint boundary crossing time analysis. *Annales Geophysicae-Atmospheres Hydrospheresand Space Sciences*, 29(12):2239, 2011.

[127] Hans Volland. *Handbook of atmospheric electrodynamics*, volume 2. CRC Press, 1995.

[128] M Volwerk, K-H Glassmeier, R Nakamura, T Takada, W Baumjohann, B Klecker, H Reme, TL Zhang, E Lucek, and CM Carr. Flow burst-induced kelvin-helmholtz waves in the terrestrial magnetotail. *Geophysical research letters*, 34(10), 2007.

[129] SN Walker, MA Balikhin, TL Zhang, ME Gedalin, SA Pope, AP Dimmock, and AO Fedorov. Unusual nonlinear waves in the venusian magnetosheath. *Journal of Geophysical Research: Space Physics (1978–2012)*, 116(A1), 2011.

[130] M Wan, WH Matthaeus, H Karimabadi, V Roytershteyn, M Shay, P Wu, W Daughton, B Loring, and Sandra C Chapman. Intermittent dissipation at kinetic scales in collisionless plasma turbulence. *Physical review letters*, 109(19):195001, 2012.

[131] Simon Wing and Patrick T Newell. 2d plasma sheet ion density and temperature profiles for northward and southward imf. *Geophysical research letters*, 29(9):21–1, 2002.

[132] Emiliya Yordanova, Andris Vaivads, Mats André, SC Buchert, and Z Vörös. Magnetosheath plasma turbulence and its spatiotemporal evolution as observed by the cluster spacecraft. *Physical review letters*, 100(20):205003, 2008.

[133] G Zimbardo, A Greco, L Sorriso-Valvo, S Perri, Z Vörös, G Aburjania, K Chargazia, and O Alexandrova. Magnetic turbulence in the geospace environment. *Space science reviews*, 156 (1-4):89–134, 2010.